Current Reports on Science and Technology

(A Peer Reviewed Research Journal)

Faculty of Sciences
Khalsa College Amritsar

Current Reports on Science and Technology

(A Peer Reviewed Research Journal)
Bi –Annual
(January-June 2016)

ISSN : 2455-023X

Subscription
Life Member : Rs. 1500/-
Five Years : Rs. 750/-
Per Copy : Rs. 125/-

For Subscription write to :
Librarian, Khalsa College Amritsar
Email : chiefeditorjpas@gmail.com, Ph: +91 183 2258097, Fax : +91 183 2255619

Current Reports on Science and Technology Published by Faculty of Sciences, Khalsa College Amritsar and printed at Printwell 146, Focal Point, Amritsar

Current Reports on Science and Technology

(A Peer Reviewed Research Journal)

Bi –Annual

Volume – 02 Issue – 01 January-June 2016

Contents

Curr. Rep. Sci. & Tech. 2 (1) (2016) 1-9

Effect Of WO_3on Covalent Behaviour of $PbO-B_2O_3$ Glasses

Gurinder Pal Singh[1], Joga Singh[1], Simranpreet Kaur[2], Parvinder Kaur[2], D.P. Singh[2],P.S. Bedi[3] and Arshdeep Kaur[3]
[1]Department of Physics, Khalsa College, Amritsar-143002, India
[2]Department of Physics, Guru Nanak Dev University, Amritsar-143005, India
[3]Chandigarh Engineering College, Landran-140307, India
gp_physics96@yahoo.co.in

Abstract

WO_3-PbO-B_2O_3 glasses containing different concentrations of WO_3 (ranging from 0-10 mol %) have prepared in our previous work.To support the structural and optical properties of these glasses some basic parameters have been calculated like molar volume, boron-boron separation, oxygen packing density, polarizibility and refractive index. It has been shown from boron-boron separation calculation that glasses have compact structure which results decrease in density. The molar volume of the glasses decreases (37.20-28.92cm^3/mol) and density increases (3.11-4.03g/cm^3) with the presence of tungsten. The presence of WO_3 causes more compaction of the borate network by breaking the bonds between trigonal elements which results in the decrease of molar volume and increase of density. Refractive index of glasses increases from (2.43-2.65). The ionic behaviour of the glasses increase due to the incorporation of WO_3.The changes caused by the addition of WO_3 on the physical properties of these glasses have been observed.

Keywords

Tungsten Borate glass; Refractive index; Ionicity.

I. Introduction

Glasses have received a considerable attention due to their unique properties like hardness, good strength, transparency and excellent corrosion resistance. Glasses are supercooled liquids, transparent, and amorphous in nature. They are inorganic product of fusion which has cooled to a rigid condition without any crystallization. The main distinction between glass and crystals is the presence of long-range order in the crystal

structure. The optimization of such properties as a function of composition and other processing parameters requires a good knowledge of the microscopic glassy structure. In glass formers, boron trioxide is generally found in the vitreous form. It is a glassy, solid and white oxide of boron. Borate glasses contain planar BO_3 groups as structural unit. Borate glasses are the technologically important class of glasses and play a significant role in various applications. Beside this PbO is also a play the role of glass former. $PbO\text{-}B_2O_3$ glasses are of technological interests owing to their unique properties such as their low melting temperatures, wide glass formation regions, and good radiation shielding properties. The glasses formed by the combination of $PbO\text{-}B_2O_3$ are transparent. These glasses have low rate of crystallization, moisture resistant and are stable in nature.

Transition metal ions doped borate glasses have many applications in microelectronics, optical glasses and solid state laser. In transition metals, tungsten metal has great importance because it has wide application in optical devices like electrochromic optical smart window & display devices [1-2]. One more interesting thing about the tungsten oxide is that it forms glasses only by combining with other glass formers such as boron oxide. Due to different valence state of tungsten in glasses likeW^{6+},W^{5+},W^{4+}etc [1-4], its presence can influence on the spectroscopy properties like structure and optical.

The main motive of the present work is the study of refractive index, molar volume, covalent and ionic behaviour of lead borate glasses in the presence of tungsten oxide.

II. Experimental details

A. Sample Preparation

Series of lead borate glasses with composition $xWO_3\text{-}(30\text{-}x)\ PbO\text{-}70B_2O_3$ (in mol%) with x=0-10 % are prepared by mixing and melting of appropriate amounts of lead (IV) oxide, tungsten (VI) oxide, and boric oxide. The glass material is melted in silica crucible at 1000° C for 60 minutes. The melt is then poured in to preheated steel mould. To avoid breaking of the samples by residual internal strains, it is immediately transferred to annealing furnace at a temperature of 380 °C for 1 hour. The

chemical composition of the undoped and tungsten doped glasses is given in the Table 1.

B. Density, Molar Volume and Boron-Boron Separation

The density of glass samples is measured by using the standard Archimede's principle with the help of a sensitive microbalance and taking pure benzene as the immersion fluid.

The density is calculated by using the formula

$$D = \frac{W_A}{W_A - W_B} \times 0.876$$

where W_A is the weight of sample in air, W_B weight of the sample in benzene and .876 is density of the benzene.

The molar volume (V^m) is calculated with the help of following formula:

$V^m = \Sigma x_i M_i / D$

where xi is the molar fraction of the component and M^i is its molecular weight.

The average boron-boron separation $<d_{B\text{-}B}>$ is calculated

$$< d_{B-B} >= \left(\frac{V_m^B}{N_A}\right)^{\frac{1}{3}}$$

where V_m is molar volume, N_A is Avogadro number.

$$V_m^B = \frac{V_m}{2(1 - X_B)}$$

X_B molar fraction of B_2O_3

III. Results

A. Density and Molar Volume

Density of samples has been found in our previous work. The variation of density and molar volume with concentration of tungsten oxide is listed in Table 1. Observation table shows that as the tungsten oxide content increases, the density increases from 3.11 to 4.03 gcm^{-3}, but the molar volume decreases from 37.20 to 28.92 $cm^{3} \cdot g^{-1} \cdot mol^{-1}$. The increase in the density depends on two reasons: (1) the ionic radius of Pb (1.27 Å) is more than tungsten (0.92 Å) so the tungsten is present in interstitial sites of

the glass network thus providing a compact structure to the glass matrix. The four coordinated boron units are formed with the help of these oxide ions. The four coordinate BO_4 are denser than BO_3 triangle [5-6]. Molar volume plays an important role in it. Due to presence of tungsten it decreases which results in decrease in bond length or inter atomic distance between atoms of glass network which resulting in compaction of structure [7-8]. Fig. 1 shows that density is inversely related with molar volume which indicates the change in glass structure when tungsten oxide content increases.

For verification of compaction of glasses due to the presence of tungsten, the average distance between boron atoms $<d_{B-B}>$ is calculated [7].The volume which contains one mole of boron within given structure is denoted by and has been found as: V_m^B

$$V_m^B = \frac{V_m}{2(1-X_B)} \text{-------(1)}$$

Where Vm and X_B are molar volumes and molar fraction of B_2O_3

$$< d_{B-B} >= \left(\frac{V_m^B}{N_A}\right)^{\frac{1}{3}} \text{--------(2)}$$

where N_A is Avogadro number. Table 1 shows that$<d_{B-B}>$value decreases with increasing of tungsten oxide content. The results show that the tungsten ions help to decrease the average boron-boron separation. Hence, compaction of glass network occurs on addition of Tungsten at the expense of B_2O_3 which confirms the density and molar volume results.

To have a profound view, the results of molar volume and density have been used to calculate the molar volume of oxygen (V_O) and oxygen packing density (OPD) by using the formula [6-7].

$$V_0 = \sum_i \frac{V_m}{x_i n_i} \quad \text{-------- (3)}$$

$$OPD = 1000C\left(\frac{\rho}{M}\right) \quad \text{-------- (4)}$$

The results obtained for molar volume of oxygen (V_0) and oxygen packing density (OPD) shows inverse relation (OPD increases and V_0 decreases) which is shown in Table 2.This happen only when more oxygen helps in the formation of bridged structure. These bridging oxygens result

in the compaction of glass structure.All the above factors such as density and molar volume shows that tungsten oxide plays an important role in the modification of glasses.

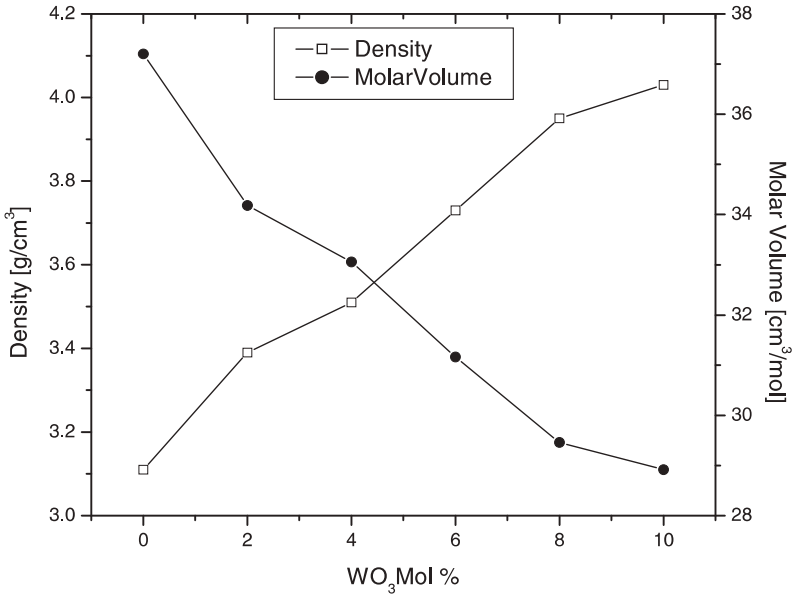

Fig.1. *Density and molar of Glasser*

Table1 *Nominal composition (mole fraction), density, Molar Volume, boron boron separation and refractive index of the glass samples.*

Glass	WO_3 (%)	PbO (%)	B_2O_3 (%)	Density (D) (g/cm^3)	Molar Volume (V_m) (cm^3/mol)	$<d_{bb}>$ (nm)	Refractive Index
PB	0	30	70	3.11	37.20	0.469	2.43
W1	2	28	70	3.39	34.18	0.456	2.46
W2	4	26	70	3.51	33.06	0.451	2.52
W3	6	24	70	3.73	31.16	0.442	2.53
W4	8	22	70	3.95	29.46	0.434	2.60
W5	10	20	70	4.03	28.92	0.431	2.65

B. Average Coordination Number

The most important parameter to confirm the bridging or non-

bridging oxygen bond is an average coordination number. It is calculated by equation [7-9]

$$m = [\sum_i n_{ci}\, x_i]\text{----(5)}$$

where m is average coordination number nciis coordination of cation. The coordination numbers of cation of tungsten, boron and lead is 6, 4 and 4 respectively. On addition of tungsten oxide the average coordination number of glass samples increases (shown in Table 2). These all results indicate that addition of tungsten oxide in a glass matrix continuously increases the number of bridging oxygens which further results in an increase of $[BO_4]$ groups in the whole glass network.

C. Bond Density

The number of bonds per unit volume gets affected by addition of tungsten and is calculated by the relation [7-9]

$$n_b = \frac{N_A}{V_m} \sum_i n_c\ x_i\text{--------(6)}$$

where n_c is the coordination number of cation, N_A is the Avogadro number, xi is mole fraction of different oxides and n_c is the coordination number of cation. Number of bonds per unit volume also increases with increase in tungsten content (Table 2).These results show that tungsten ions play an important role in the modification of glasses.

D. Covalency and Ionicity

Structure as well as optical properties of glasses also depend on ionicity and covalency of glasses. These can be calculated on the basis of Pauling's bond iconicity and by using electro negativity difference [8-11]. Electro negativity difference of glasses can be calculated by using the following equation:

$$\Delta\chi=\sum x_i \Delta\chi_i\ \text{-------(7)}$$

In this, $\Delta\chi_i$ is the electronegativity difference of glass which contain oxides and can be calculated by using the relation $\Delta\chi i=\chi_A-\chi_C$ where $\chi_A$and χ_C are taken as the Pauling electronegativity of cation and anion respectively.

The Pauling's bond ionicity relation (I_b) is shown below:

$$I_b = [1 - e^{\left(-0.25(\chi^2)\right)}]\text{--------(8)}$$

The bond ionicity I_b and electro negativity difference with values $\Delta\chi$ continuously increases and covalent character of the glasses is inversely related to tungsten concentration in glass network as shown in Table 2. It shows the change of covalent character to ionic character of glasses which causes a decrease in optical band gap semiconductor region.

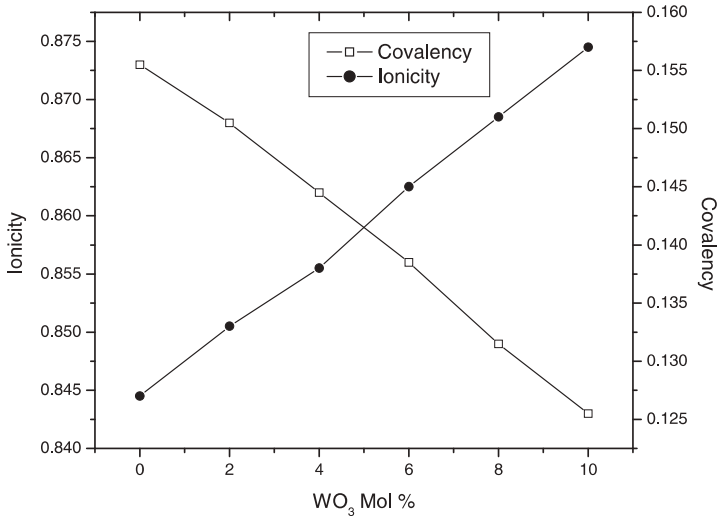

Fig. 2. *Lonicity and Covalency of Glasses.*

Table 2 *The covalency, ionicity, oxygen packing density, molar volume of oxygen, number of bonds per unit volume, average coordination number, Molar refraction and Molar Polarizibility of the glass samples respectively.*

Glass	Covalency	Ionicity	OPD	V_0	Bond Density	Average Coordination Number	Molar refraction,	Molar polarizibility
PB	0.873	0.127	64.52	15.50	0.648	4	23.06	0.915
W1	0.868	0.133	71.39	14.01	0.712	4.04	21.44	0.850
W2	0.862	0.138	75.02	13.33	0.743	4.08	21.19	0.840
W3	0.856	0.145	80.88	12.36	0.797	4.12	20.01	0.794
W4	0.849	0.151	86.89	11.51	0.850	4.16	19.36	0.768
W5	0.843	0.157	89.90	11.12	0.875	4.2	19.29	0.765

E. Refractive Index, Molar Refraction, Molar Polarizibility

Refractive index is the most important optical property and it varies by changing the base glass composition. It is also important from electric point of view. The relation which is used to calculate the refractive index

has been given by Dimitrova et.al [12-14]. By using this relation refractive index has been calculated as:

$$\left(\frac{n^2-1}{n^2-2}\right) = 1 - \sqrt{\frac{E_g}{20}}$$

$$R_m = \left(\frac{n^2-1}{n^2-2}\right) V_m$$

$$\alpha_M = \left(\frac{3}{4\pi N_A}\right) R_m$$

In this: n, R_m, E_g, N_A and α_m are the refractive index, molar refraction, optical band gap, Avogadro number and polarizibility respectively.

The observations reveal that refractive index of glasses increases gradually with decrease in the optical band gap corresponding to an increase in WO_3. The refractive index increases because coordination of borate changes from trigonal [BO_3] to tetrahedral [BO_4].

IV. Conclusion

The above discussion shows that addition of WO_3 increases the density corresponding decrease in molar volume of PbO-B_2O_3 glasses. The presence of tungsten in the glass samples causes more compaction of the borate network due to the formation of more BO_4 groups.The boron-boron separation and number of bonds per unit volume calculation also support the compact structure of glasses.Refractive index of glasses also increases with the incorporation of tungsten oxide due to conversion of BO_3 to BO_4 groups. Covalency of glasses decreases and ionicity increases. Hence by controlling the material composition physical properties can be tuned for particular purpose.

V. References

[1] R.Sivakumar, C.Sanjeeviraja, M.Jayachandran, R.Gopalakrishnan, S.N.Sarangi, D. Paramanik, T. Som, J.Phy: condens.Matter 19 (2007) 186204.

[2] C. Lasbrugnas, P. Thomas, O. Masson, J.C. Champarnaud-Mesjard, E. Fargin, V.Rodriguez, M. Lahaye, Opt. Mater. 31 (2009) 775.

[3] G. Pal Singh, D.P. Singh Physica B 406 (2011) 640644.
[4] G. Pal Singh and D.P. Singh Can. J. Phy 89(2011)1281.
[5] G. Pal Singh, Simranpreet Kaur, Parvinder Kaur, D.P. Singh, Physica B 407 (2012)1250.
[6] G. Upender, S. Ramesh, M. Prasad, V. G. Sathe, V. C. Mouli, J. Alloy Comp. 504 (2010) 468.
[7] G. Pal Singh, D.P. Singh, J. Mole.Struc.1012 (2012)137.
[8] M. Abdel-Baki, F. A. Abdel-Wahab, Fouad El-Diasty, J. Appl. Phys. 111(2012) 073506.
[9] G. Lucovsky, J. Optoelectron. Adv. Mater. 3 (2001)155.
[10] M A Baki and F El-Diasty, J. Solid State Chemistry 184 (2011) 2762.
[11] V. Dimitrov, T.Komatshu, J.Solid State Chem. 163 (2002) 100.
[12] V. Dimitrov, T. Komatshu, J. Solid State Chem. 163 (2002) 100.
[13] J.A. Duffy, J. Solid State Chem. 62 (1986) 145.
[14] G. Pal Singh, Parvinder Kaur, Simranpreet Kaur, D.P. Singh, Physica B 407 (2012)4168.

Curr. Rep. Sci. & Tech. 2 (1) (2016) 10-16

Dynamics of the reaction involving loosely bound projectile

Mandeep Kaur[1], BirBikram Singh[1] and Manoj K. Sharma[2]
[1]Department of Physics, Sri Guru Granth Sahib World University, Fatehgarh Sahib-140406, India.
[2]School of Physics & Material Sciences, Thapar University, Patiala-147004, India.
**birbikram.singh@gmail.com*

Abstract

In reference to the experimental data given for fusion cross-section of a proton rich projectile ^{7}Li with the target ^{27}Al, a comprehensive decay analysis of composite system $^{34}S^{*}$ is made within Dynamical cluster Decay Model (DCM) of Gupta and collaborators. The motivation behind this work is the quest for dominant decay mode present in $^{34}S^{*}$. The results show that the fusion yield has almost equal contribution from both light particles (LPs) and fission fragments equally. The fragmentation behavior, preformation profile are also presented using deformations and hot compact orientations within DCM for the decay of $^{34}S^{*}$ formed in a reaction with loosely bound projectile ^{7}Li.

Keywords

Heavy Ion Induced reactions, Complete Fusion, Incomplete Fusion.

I. Introduction

Experiments using stable weakly bound nuclei provide valuable information to understand number of nuclear properties in heavy ion reactions at low energies. In this context, ^{6}Li, ^{7}Li and ^{8}Be beams have been found extremely useful to explore the reaction dynamics around the Coulomb barrier. Fusion of weakly bound and exotic radioactive nuclei are reactions of great interest which may also play a significant role in the formation of new nuclei near the drip lines. Unlike the reactions with tightly bound nuclei, a substantial contribution of breakup and transfer is observed in case of weakly bound nuclei. The breakup and transfer may be

followed by subsequent fusion of only a part of the projectile which is known as incomplete fusion (ICF). In this framework, the fusion is classified in terms of complete fusion (CF), which refers to fusion of the whole projectile or all its fragments, and total fusion (TF), where the ICF processes are also included. For unstable nuclei, the fusion process is affected by their low binding energy, which can cause them to break up before reaching the fusion barrier. Thus the breakup process may reduce the CF cross sections, making it difficult in superheavy element formation. Alternatively, the extended structure (i.e cluster comprising excess number of protons/ neutrons or both) of loosely bound nuclei could in principle may induce a large enhancement/suppression of fusion.

The study of proton-rich systems (towards proton drip-line) has become an interesting area of research. Many reactions induced by weakly bound radioactive nuclei have been studied in the energy region near and around Coulomb barrier. Low breakup threshold and cluster structure of these nuclei enhance the importance of reaction dynamics i.e. transfer and breakup channel starts competing with usual compound nucleus process. This may influence the quantum tunneling which may effect the fusion cross- sections via modification in the barrier height and barrier position. So, the interesting feature of these studies is to address the effect of breakup of such loosely bound projectiles on the fusion cross-sections in the context of enhancement and suppression processes [1,2]. In view of this context regarding the importance of loosely bound projectile we intend to analyse the reaction dynamics of composite system $^{34}S^{*}$ formed in $^{7}Li^{+27}Al$ within the framework of Dynamical Cluster Decay (DCM) model of Gupta and collaborators [3]. Recently, we have made calculations for a compound system $^{65}Ge^{*}$ formed when the loosely bound projectile ^{7}Be fuses with the target at near and sub barrier energies to study the proton evaporation yield. The calculations has been done by spherical as well as hot compact oriented nuclei considerations at six different centre of mass energies and are in good comparison with the experimental data [4].

In the present study we intend to analyse the fusion cross section of lighter compound system $^{34}S^{*}$ formed in $^{7}Li_{+}{}^{27}Al$ reaction at E_{lab}=10 MeV using hot compact orientationwithin the DCM. Here, the preliminary calculations of fusion yield σ_{fus} includes fusion fission (ff) cross-section σ_{ff} and evaporation residues/ light particles LPs cross section σ_{ERs}in the decay $^{34}S^{*}$ and is further compared with the experimental data [5] along with relevant discussion associated with fragmentation profile, preformation

behavior along with penetration probability of LPs as well as ff fragments. We have investigated the reaction dynamics of a lighter compound system $^{34}S^{*}$, formed in a reaction involving weakly bound projectile ^{7}Li bombarded on a target ^{27}Al at E_{lab}=10 MeV, using the methodology of DCM, for which details are given in section II. The calculations and results are discussed in section III alongwith their comparison with the experimental data [5]. In section IV study is concluded.

II. Methodology: Dynamical Cluster Decay Model

Dynamical cluster decay model (DCM) is different from another statistical model as it treats the evaporation residues (ERs), intermediate mass fragments (IMFs) and fusion fission (ff) on equal footings [4].The missing nuclear structure information of compound nucleus in statistical model enters in DCM via preformation probability P_0 of the fragments and is calculated by solving Schrodinger equation in η co-ordinate. For ℓ-partial waves, the compound nucleus decay cross-section is given by

$$k=\sqrt{\frac{2\mu E_{c.m}}{\hbar^2}} \qquad \sigma=\frac{\pi}{k^2}\sum_{l=0}^{l_c or l_{\max}}(2l+1)P_0P \tag{1}$$

where, $\mu = [A_1A_2/(A_1 + A_2)]m$, is the reduced mass, with m as the nucleon mass and ℓ_{max} is the maximum angular momentum. The angular momentum ℓ_{max} is fixed for vanishing the fusion barrier of incoming channel $_i$ or light particles cross-section $_{LP}$. The total fusion cross-sectionwithin this model is given by

$$\sigma_{fus}= \sigma_{ER}+ \sigma_{ff}+ \sigma_{nCN} \tag{2}$$

where σ_{ER}, σ_{ff} and σ_{nCN} are respectively evaporation residue/ LPs, ff and non-compound nucleus cross sections which sum up to give fusion cross section fus. Apparently, in the DCM, both LPs and complex IMFs up to symmetric division are treated as the dynamical collective mass motions of preformed clusters or fragments through the barrier. In equation. (1), the preformation probability P_0 is obtained by solving the stationary Schrodinger equation in, at a fixed $R = R_a$, and is given by

$$P_0 = \sqrt{B_{\eta\eta}}\left|\psi[\eta(A_i)]\right|^2(2/A) \tag{3}$$

The structure information of the compound nucleus enters the preformation probability P_0 through the fragmentation potential V (R, η, $\beta\lambda_i$,θ_i, T), defined as

$$V(\eta, R, \ell, T) = \sum_{i=1}^{2}\left[V_{LDM}(A_i,Z_i,T) + \sum_{i=1}^{2}[\delta U_i]e^{\left(\frac{-T^2}{T^2}\right)} + V_c(R,Z_i,\beta_{\lambda i},\theta_i,T) + (R,A_i,\beta_{\lambda i},\theta_i,T) + V_\ell(R,A_i,\beta_{\lambda i},\theta_i,T)\right] \quad (4)$$

Here $V_{LDM}$and U are, respectively, the T-dependent liquid drop and shell correctionenergies [6], V_c is the coloumb potential,V_p indicates the proximity potential and $V_\ell$denotes the angular momentum dependent potential. The penetrability calculated as the WKB tunneling probability

$$P = \exp[-\frac{2}{\hbar}\int_{R_a}^{R_b}\{2\mu[V(R) - Q_{eff}]\}^{1/2}dR] \quad (5)$$

where is defincal R_a, defined above, is the first turning point of the penetration path used for calculating the WKB penetrability P.

III. Calculations and Discussions

The fusion excitation function for light mass system $^{34}S^*$ formed by the fusion of loosely bound projectile ^{7}Li onto ^{27}Al target at $E_{c.m.}$ = 7.9411 MeV. Interestingly no one particular decay mode is major contributor in the fusion yield, instead, the cross sections for LPs, energetically favored intermediate mass fragments (IMFs), and fission fragments seem to contribute collectively.

Fig.1 (a) illustrates that fragmentation profile V(MeV) for the decay of of parent nuclei $^{34}S^*$ at $E_{c.m.}$ = 7.9411 MeV (T=3.203) at extreme ℓ values, ℓ = 0ħ and at ℓ_{max}= 30ħ We can see that potential energy surface does not change from ℓ = 0ħ and 30ħ, except the behavior of Li isotopes (^{6}Li,^{7}Li,^{8}Li), at ℓ = 0ħ, ^{8}Li has higher potential as compared to ^{6}Li, ^{7}Li,but at ℓ = 30ħ ^{7}Li has higher potential as compared to ^{6}Li, ^{8}Li. It means that ^{7}Li looses its stability as we go from ℓ = 0ħ to at higher ℓ values. The behavior of remaining fragments is almost consistent at both the ℓ values.

Fig.1 (a). The fragmentation potentials V (MeV) as a function of fragment mass A, for the compound system $^{34}S^*$ formed in the reaction ^{7}Be+^{27}Al at two extreme ℓ-values. (b) The variation of summed up preformation factor P_0 with angular momentum, for the decay of $^{34}S^*$ to both LPs and complex fragments.

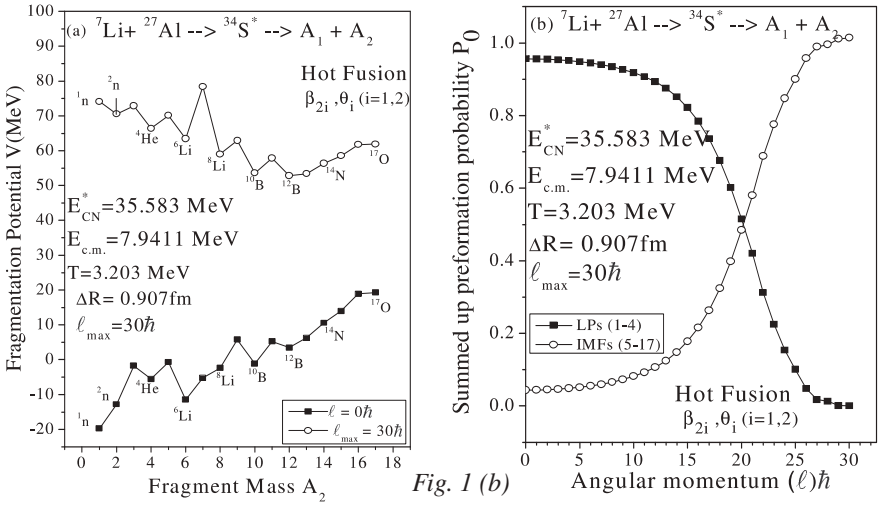

Fig. 1 (b)

Fig.1 (b) shows the summed up preformation profile for LPs and IMFs/ complex fragments as a function of angular momentum. It shows that the LPs are highly preformed at lower ℓ − values, but IMFs starts contributing at higher ℓ − values. It means that LPs are more favored at lowerℓ−values,but IMFs become favorable at higher ℓ−values. Fig. 2 depicts the behavior of summed up penetration probability for LPs as well as IMFs, it shows that both starts penetration through the fusion barrier at higher ℓ − values i.e. at lower ℓ − values the penetration probability for all the fragments is almost zero, but around ℓ = 20ħ the penetration probability starts increasing at very fast rate. Similar type of results has also been obtained earlier but for light mass compound nucleus $^{48}Cr^{*}$ [7].

Table.1 *The DCM calculated fusion cross-sections $\sigma_{fus.}$ for the decay of $^{34}S^{*}$ formed in $^{7}Li+^{27}Al$ reaction at the excitation energy E^{*}_{CN} = 35.5 MeV, compared with the experimental data [6].*

$E_{c.m.}$(MeV)	T (MeV)	ℓ_{max}(ħ)	ΔR(fm)	$\sigma_{fus.}$(mb)			
				DCM(ERs)	DCM(ff)	DCM(total)	Expt.
7.9411	3.203	300	0.907	211.13	226	437.13	415±67

The calculated fusion cross section with other details is presented in Table1. The fusion cross-section is fitted within DCM having only one parameter ΔR i.e. neck length parameter. At ΔR = 0.907fm we are able to fit the given experimental fusion cross-section. The contribution of different decay modes LPs and fission fragments towards this fusion yield is also shown in this table. It is mention here that present study of σ_{fus} has been

made at the energy which is below the Coulomb barrier. Moreover, it is noted here that within theframework of DCM we do not get any nCN contribution and the σ_{fus} comprises the contribution from LPs and fission fragments resulting from collective clusterization process. It will be highly exciting to study the case at different energies i.e. below and above the Coulomb barrier.

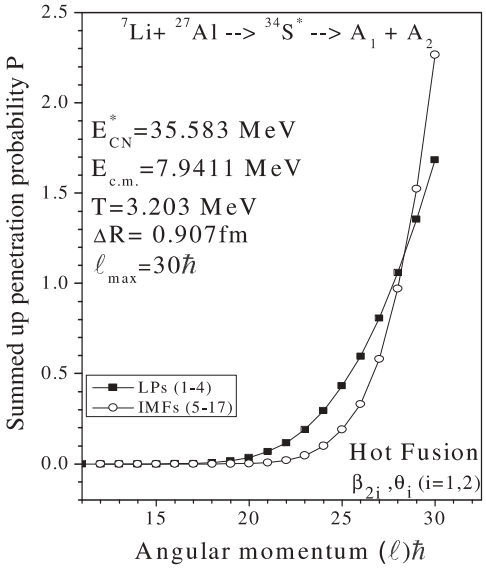

Fig. 2. *The variation of summed up penetration probability P with angular momentum for for the decay of $^{34}S^{*}$ to both LPs and complex fragments.*

IV. Conclusion

The fusion cross section σ_{fus} for light mass compound system $^{34}S^{*}$ formed by the fusion of loosely bound projectile ^{7}Li onto target ^{27}Al at $E_{c.m.}$ = 7.9411 MeV is analyzed. Interestingly no one particular decay mode is major contributor in the fusion yield, instead, the cross sections for LPs, energetically favored IMFs and fission fragments seem to contribute collectively. Behavior of the particles changes with ℓ−values, LPs are energetically more favored at lower ℓ−values, IMFs starts contributing at higher ℓ − values.

V. Acknowledgment

B. B. S. acknowledges the support by the Department of Science and

Technology, New Delhi, in the form of a YoungScientist Award under the SERC Fast Track Scheme, videletter No. SR/FTP/PS-013/2011

VI. References

[1] R. Raabe, C. Angulo, J. L. Charvet, C. Jouanne *et al*., "Fusion and direct around the barrier for the systems ^{7,9}Be, ^{7}Li + ^{238}U"*Phy. Rev. C* **74** (2006) 044606.

[2] E. Martinz-Quiroz, E. F. Aguirela, D. Lizacano, P. Amador-Valenzuela *et al* ., "Near and sub-barrier fusion of ^{7}Be +^{58}Ni system" *Phys. Rev. C* **90** (2014)014616.

[3] Raj. K. Gupta, Sham K. Arun, Raj Kumar and Niyti., "Collective Clusterization in Hot and Rotating Nuclei: Preformed-cluster based Dynamical Cluster-decay Model"*IREPHY* **2** (2008) 369; "Clusters in Nuclei" *Lecture Notes in Physics* **818** (2010) 223.

[4] Mandeep Kaur, Bir Bikram Singh and Manoj K Sharma., "Proton evaporation yields of ^{65}Ge* formed in ^{7}Be + ^{58}Ni reaction at near and sub barrier energies" Proc. *DAE Symp. On Nuc. Phys.* **59** (2014) 474.

[5] K. Kalita, S. Verma, R. Singh, J. J. Dass et al., "Elastic scattering and fusion cross section for ^{7}Be, ^{7}Li + ^{27}Al systems"*Phy. Rev. C* **73** (2006) 024609.

[6] W. Myers and W. J. Swiatecki., "Nuclear masses and deformations"Nucl.Phys. **81** (1966) 1.

[7] Birbikram Singh, Manoj K Sharma, Raj K. Gupta and Walter Griener., "Entrance channel effects in the dynamical cluster decay model for the decay of hot and rotating compound nucleus ^{48}Cr* at E_{CN}^{*}=60 MeV" *Int. J. of Mod. Phy.* E **15** (2006) 699.

Curr. Rep. Sci. & Tech. 2 (1) (2016) 17-23

Synthesis, Structural and Optical Properties of $Zn_{1-x}Ni_xO$ Nanoparticles Prepared by Coprecipitation Method

Deepawali Arora, Pardeep Singh, Parvinder Kaur, Sunil Kumar, Gurinder Pal Singh, Divya Kamra, Rupali Suhuntea, Jaspreet Kaur, Aman Mahajan and D.P. Singh
Department of Physics, Guru Nanak Dev University, Amritsar 143005, India
dpsinghdr@yahoo.com

Abstract

The samples of $Zn_{1-x}Ni_xO$ (x= 0.00 and 0.05) were prepared with coprecipitation method annealed at 400 and 600°C temperatures. The effect of Ni ion substitution on the structural and optical properties has been studied using X-ray Diffraction (XRD), Ultraviolet-Visible, Photoluminescence Spectroscopy (PL) and Scanning Electron Microscopy (SEM). XRD measurements demonstrate that all the prepared samples are polycrystalline single phase in nature and belong to the wurtzite structure. Ultraviolet visible measurements showed a decrease in band gap with the increase in annealing temperature and doping concentration. PL data showed red shift in all the samples with the increase in the annealing temperature. Ni doped ZnO illustrated the morphology is well ordered, has low aggregation, and has a homogeneous distribution of particle size

Keywords

II-VI semiconductors, Transition metal and alloys, Impurity and defect levels, Photoluminescence, Band structure

I. Introduction

Currently, ZnO is attracting attention for its application to transparent high power electronics, surface acoustic wave devices, UV light-emitters, gas-sensing and as a window material for display and solar cells [1]. Zinc oxide (ZnO) with a direct wide bandgap (3.37eV at room temperature) is an n-type semiconductor. In ambient condition, ZnO has a stable hexagonal wurtzite structure with lattice spacing a = 0.325 nm and c = 0.521 nm

[2]and is composed of a number of alternating planes with tetrahedrally-coordinated $O^{2-}$and Zn^{2+} ions, stacked alternately along the *c*-axis. All these predominant properties make ZnO a great potential in the field of nanotechnology. Usually ZnO is doped with different types of metallic ions, like Ga, In, Sn, Al, Sc,Ti, V , Ni , Co and Mn in order to improve its transparent conducting oxide properties [3-4]. ZnO nanoparticles can be prepared by low cost and simple solution based method, such as, sol-gel synthesis, chemical precipitation and hydrothermal reaction [5-6]. Coprecipitation method is a promising alternative synthetic method as it works low working temperature as well as particle size could be easily controlled.

In the present work undoped and Ni doped ZnO nanoparticles were synthesized by using chemical coprecipitation method and thus an attempt was made to study structural and optical properties of undoped and Ni doped ZnO nanopwders.

II. Experimental Details

$Zn_{1-x}Ni_xO$ (x= 0.00 and 0.05) powders were prepared by coprecipitation method. Sol was synthesized using sol-gel solution route technique in order to obtain the Ni doped ZnO powders. For the preparation of sol, stoichiometric amounts of metal nitrate, Zn $(NO_3)_3.6H_2O$, Ni $(NO_3)_3.6H_2O$ was dissolved in deionized water to get 0.6 M solution. No stabilizer was added. This solution was kept for 1 hour for stirring at room temperature. In this solution, 5 M NH_4OH was added drop wise, till the pH value reached to 9,the solution was stirred for 3 hours and then filtered and washed with de-ionized water and ethanol 3 times. The mixture was then dried at 800^{o}C for 15 hours. The dried mixture was then grounded. The obtained powders were annealed at 400°C and 600^{0}C temperatures. Structural characterization of undoped and Ni doped ZnO nanopwders was done using Shimadzu XRD-7000 X-Ray diffractometer (Cu K_α, λ=1.5418 Å) and optical studies were done using ultra-violet visible spectrometer (Perkin Elmar, Lambda 35). Photoluminescence studies were done with fluoremeter LS 45 to excite the luminescence with fixed wavelength light and to measure the intensity of the PL emission at a singlewavelength or over a range of wavelengths. Morphological studies were done using JEOL-JSM 6610 LV instrument, operated at 15kV.

III. Results and Discussion

Fig. 1 and Fig.2 show X-Ray diffraction spectra of undoped and Ni doped ZnO annealed at 400° and 600°C temperatures. The patterns reveal polycrystalline hexagonal wurtzite structure of ZnO. No significant change is observed in the peak position as the annealing temperature of undoped ZnO is increased from 400 to 600°C, but the intensity of all the peaks is found to decrease which indicate a little degradation in the crystallinity of ZnO. A reflection of NiO crystalline structure has been observed at 2θ (43.20). This peak shifts to left at 2θ (43.06) and an increase in intensity of this peak is observed with the increase in annealing temperature. This shift is an evident that Ni gets oxidized and incorporated to larger extent in ZnO indicting the distortion of NiO to a larger spacing [7]. This indicates phase segregation which confirms the limit of solubility of Ni in ZnO to 2.5mole % for low temperature growth conditions.

The lattice parameters values (Table 1) were calculated using XRD. As compared with standard values of lattice parameters of ZnO (a = 0.325 nm and c = 0.521nm), c parameter decreased with annealing temperature and doping of Ni ions. This decrease can be justified since the ionic radius of Ni^{2+} (0.069 nm) is less than that of Zn^{2+} (0.074nm) [8]. The particle size D, of ZnO: Ni nano particles were estimated using Debye- Scherer's equation

$$D = \frac{k\lambda}{\beta \cos \theta} \quad (1)$$

where, λ = 1.54 Å(Cu K_α radiations wavelength), β = full width at half maxima, θ is the Bragg's angle (2θ). The particle size of the nanoparticles is found to increase with the annealing temperature and Ni doping into ZnO host matrix.

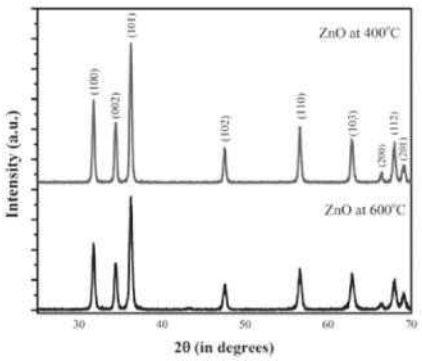

Fig1. XRD pattern of undopedZnO annealed at 400 and 600°C temperatures.

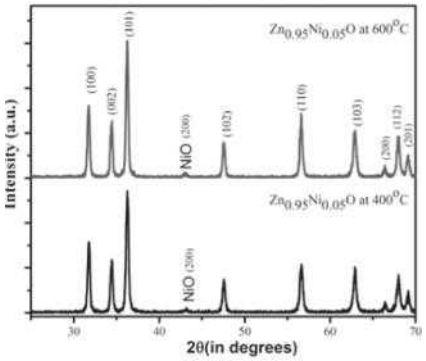

Fig 2. XRD pattern of $Zn_{0.95}Ni_{0.05}O$ annealed 400 and 600°C temperatures.

Fig. 3 shows the SEM images of as prepared nanocrystalline ZnO and $Zn_{0.95}Ni_{0.05}O$ powders annealed at 400° and 600°C temperatures. The prepared samples show agglomeration of nanoparticles andmorphology seems to be almost spherical in structure.

Uv-Vis spectra of undoped ZnO and $Zn_{0.95}Ni_{0.5}O$ nanoparticles are shown in Fig. 4(a) and 4(b). The calculated band gaps are tabulated in Table 1 with an average error of ±0.01. The band gap is found to decrease with doping, since doping of ZnO with Ni adds defects sites in the vicinity of valence band and reduces the effective band gap [9]. The decrease in the band gap with annealing temperature may be attributed to the better substitution of Ni ions hence annealing out some defects.

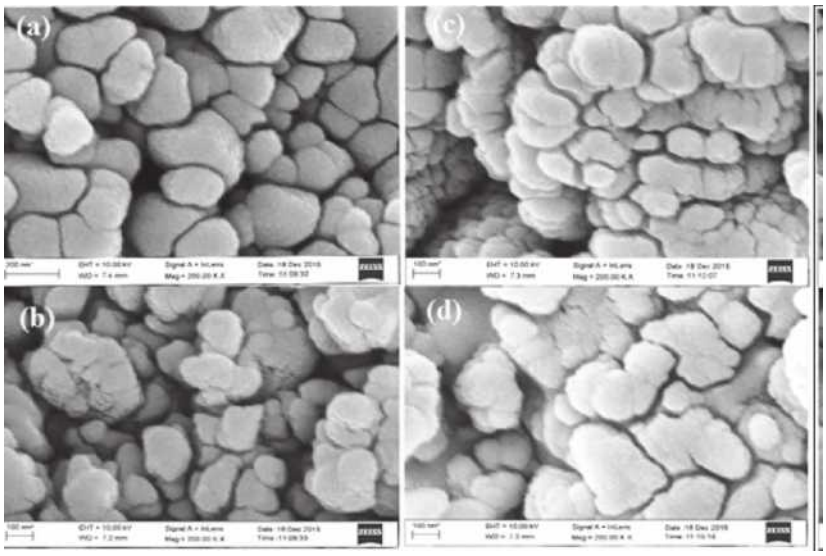

Fig 3. *SEM micrographs of undoped ZnO (a) and (b), (c) and (d) of* $Zn_{0.95}Ni_{0.05}O$ *annealed at* 400^0 *and* 600^0*C temperatures respectively.*

Fig. 5 (a) and 5(b) illustrate the photoluminescence spectra of undoped and Ni doped ZnO respectively with 290 nm excitation under roomtemperature. The PL emission consists of broad visible region, which can be attributed to the electronic transitions from the level of interstitial zinc asassociated with ionized oxygen vacancies to the valence band [10]. A peak at 423 nm refers to the violet luminescence which is probably due to radiative defects related to the interface traps existing at the grain boundaries and emitted from the radiative transition between this level and

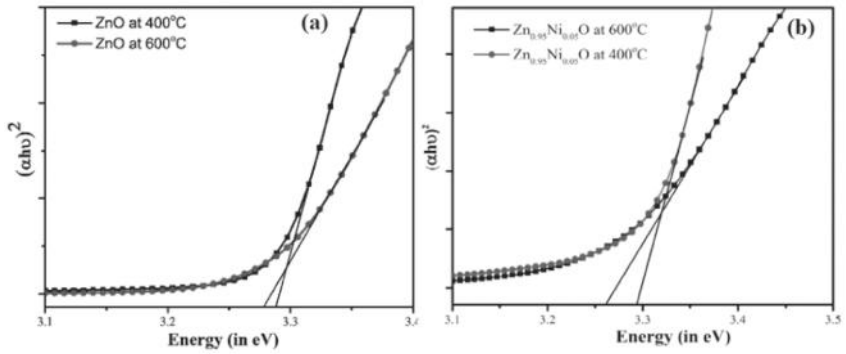

Fig 4. *Optical Band gap of (a) ZnO(b) Ni doped ZnO annealed at 400 and 600°C temperatures respectively.*

the valence band [11].Another peak at 485 nm refers to the blue emission and can be attributed to the transitions between the oxygen vacancy and lattice defects related to oxygen and zinc vacancies [12].The PL intensity becomes stronger as the annealing temperature increases from 400 to 600o C which might be attributed to the recovery of microstructural defects [13]. However, with Ni doping the peak at 485 nm quenched with the significant value.This quenching might be due incorporation of Ni ions into the ZnO host matrix and hence leads to decrease in the crystalline quality of the samples, and is consistent with XRD results.

Table 1. *Variation in lattice parameters, band gap and crystallite size with annealing temperature and doping concentration.*

Parameters	**Pure ZnO**	**ZnO**		**$Zn_{0.95}Ni_{0.05}O$**	
Temperature(°C)		**400**	**600**	**400**	**600**
a parameter	3.250	3.270	3.279	3.279	3.279
c parameter	5.204	5.212	5.208	5.205	5.202
Band Gap (eV)	3.37	3.29	3.28	3.30	3.26
CrystalliteSize (nm)	-	20.80	20.96	22.10	24.60

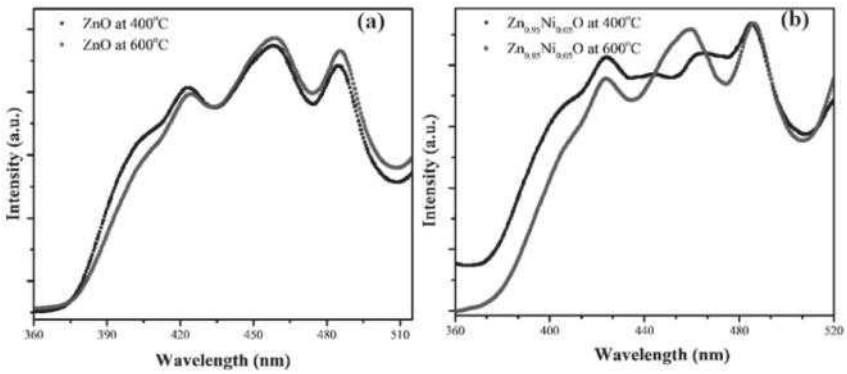

Fig 5.*Room temperature photoluminescence spectra of (a) undopedZnO (b) Ni doped ZnO annealed at 400 and 600°C annealing temperatures respectively.*

IV. Conclusion

In summary, a facile method of nanoparticles synthesis was used to synthesize Ni-doped znO nanoparticles. XRD analysis shows wurtzite structure for ZnO and $Zn_{1-x}Ni_xO$ lattice. Unit cell expansion is clearly observed for Ni doped ZnO nanoparticles. particle size was calculated by Debye-Scherrer equation and is between 20-24 nm. The band gap analysis from Uv-vis spectra shows enhancement in the band gap upon Ni doping in ZnO.Ni doped ZnO illustrated the morphology is well ordered with low aggregation, and has a homogeneous distribution of particle size. Optical absorption measurements indicate red shift in the absorption band edge upon Ni doping.

V. References

[1] P. Zu, Z.K. Tang, G.K.L.Wong, M. Kawasaki, A. Ohtomo, K. Koinuma and Y. Sagawa, "Ultraviolet spontaneous and stimulated emissions from ZnO microcrystallite thin films at room temperature," Solid State Commun.103 (1997) 459

[2] K. Nakahara, and Takasu, "Interactions between gallium and nitrogen dopants in ZnO films grown by radical-source molecular-beam epitaxy, Appl. Phys. Lett. 79 (2001) 139-4141

[3] V.N. Zhitomirsky, E. Cetinorgu, R.L. Boxman and S. Goldsmith, "Properties of SnO_2 films fabricated using a rectangular filtered vaccum arc plasma source," Thin Solid Films516 (2008) 5079.

[4] B.D. Ahn, S.H. Oh, C.H. Lee, G.H. Kim, H.J. Kim and S.Y. Lee, "Influence of thermal annealing ambient on Ga-doped ZnO thin films," J. Cryst. Growth 309 (2007)128

[5] Z. Hui, Y. Deren, M. Xiangyang, J.Yujie and X. Jin, "Luminescence properties of ZnO films annealed in growth ambient and oxygen," Nanotechnology15 (2004) 622

[6] J. Zhang, L. D. Sun and J. L. Yin, H. L. Su, C. S. Liao, and C.H.Yan,"Control of ZnO morphology via a simple solution route", Chem. Mater.14 (2002) 172

[7] M. Xingyu, Z. Wei, and D. Youwei, "Ferromagnetism of Ni cluster in Ni-doped ZnO by solid state reaction" J. Mag. Mag. Mater. 320 (2008) 1102-1105.

[8] M. El-Hilo, A.A. Dakhe and A.Y. Ali-Mohamed,"Room temperature ferromagnetism in nanocrystalline Ni-doped ZnO synthesized by co-precipitation," J. Magn. Magn. Mater. 321 (2009) 22792283.

[9] S. Kant and A. Kumar,"Synthesis and Characterization of Transition Metals Doped ZnO Nanorods," Adv. Mat. Lett.3(4) (2012) 350-354.

[10] R. Elilarassi, and G. Chandrasekaran,"Synthesis and optical properties of Ni-doped zinc oxidenanoparticles for optoelectronic applications," Optoelec. Lett.6 (2010) 1

[11] B.J. Jina,S.Imb and S.Y. Leec, "Violet and UV luminescence emitted from ZnO thin films grown onsapphire by pulsed laser deposition," Thin Solid Films 366 (2000) 107-110.

[12] S. Kumar, N. Kumari, S. Kumar, S. Jain and N. K. Verma, "Synthesis and characterization of Ni-doped Cd Senanoparticles: magnetic studies in 300100 K temperature range,"Appl.Nanosci. 2 (2012) 437-443.

[13] D.J. Qiua, H.Z. Wua,b , A.M. Fengc , Y.F. Laob , N.B. Chena and T.N. Xua, "Annealing effects on the microstructure and photoluminescenceproperties of Ni-doped ZnO films," Appl. Surf. Sci.222 (2004)263-268.

Curr. Rep. Sci. & Tech. 2 (1) (2016) 24-30

Ethanol And Acetone Sensing Response Of Pure And Doped Cr_2O_3 Nanoparticles

Nipin Kohli[1] and Ravi Chand Singh[2]
[1]Department of Physics, BBK DAV College for Women, Amritsar, India
[2]Department of Physics, Guru Nanak Dev University, Amritsar, India
nipinkohli82@yahoo.com

Abstract

In this work the effect of tin and tungsten (as a dopant) on the structure, morphology and sensing response of Cr_2O_3 nanoparticles has been reported. Wet chemical route was adopted for the synthesis of Cr_2O_3 nanoparticles and 4% of tin and tungsten by weight were added separately at the time of reaction. To understand the structure, synthesized materials were subjected to X-ray diffraction (XRD) and field emission scanning electron microscopy (FESEM). XRD study exhibited that the diffraction peaks shift slightly towards left for tin doped Cr_2O_3 whereas no such observation was made for tungsten doped Cr_2O_3. However, crystallite size of all the samples was nearly same. In FESEM images no change in morphology was observed due to the introduction of dopant. Chromium oxide samples thus prepared were deposited as thick films on alumina substrates to act as gas sensors and their sensing response to acetone and ethanol vapour was investigated at different operable temperatures. It has been observed that pure and doped sensors exhibited optimum response at 250°C. The investigations revealed that the addition of tin and tungsten as a dopant enhanced the sensing response of Cr_2O_3 nanoparticles appreciably.

Keywords

Nanoparticels, sensor, XRD, precipitation.

I. Introduction

Gas sensors based on semiconducting metal oxides are the most investigated group of gas sensors. These sensors undergo resistance change upon exposure to reducing gases by the oxidative interactions with the negatively charged chemisorbed oxygen. The gassolid interaction

influences the density of electronic species and thereby resistance of material. The gas sensing characteristics such as gas response, response time, recovery time and selectivity are greatly influenced by the surface area, morphology, particle size, particle size distribution and porosity [1]. However, introduction of dopants in the parent system is one of the important techniques which influence the sensing performance of gas sensors based on nanoparticles [24]. Recently, various techniques such as thermal evaporation [5], sputter deposition [6], wet chemical route [7] etc. have been used for doping of metal oxide nanostructures.

In the present work, synthesis of chromium oxide (Cr_2O_3) nanoparticles has been carried out by wet chemical technique and an attempt has been made to improve the sensing performance of Cr_2O_3 nanoparticles by the addition of tin (Sn) and tungsten (W).

II. Experimental Details

Tin doped chromium oxide (Sn/Cr_2O_3) powder was prepared by following a chemical route. 0.2 M solution of $CrCl_3 6H_2O$ and $SnCl_4 5H_2O$ was prepared in distilled water, with concentration of tin as 4% by weight. Then resulting solution was precipitated by adding ammonium hydroxide drop wise at room temperature. The precipitate thus obtained was separated from rest of the liquid by filtering and was dried into powder at 120°C. Then the powder was calcined at 500°C for 3 hours. In similar manner tungsten doped chromium oxide (W/Cr_2O_3) was prepared using tungstic acid and chromium chloride hexahydrate as precursors. Following above mentioned procedure another powder was synthesized only from $CrCl_3 6H_2O$ without adding any dopant.

Crystal structure of prepared samples was characterized by XRD using Cu K_α radiation and morphologies of the samples were analyzed by FESEM.

To fabricate thick film sensors, an appropriate amount of synthesized powder was taken and mixed with distilled water to make paste. The paste was coated onto an alumina substrate between two gold electrical contacts to obtain a thick film. Using above procedure a batch of sensors was fabricated from synthesized samples. Sensing response of these samples

was investigated in an indigenously developed chamber and the sensing response for gas species was recorded by Keithley Data Acquisition Card KUSB3100. The sensor response magnitude was determined as R_g/R_a ratio, where R_g and R_a are the resistances of sensor in airgas ambience and air respectively.

III. Results And Discussion

A. Structural Analysis

Fig. 1 represents X-ray diffraction patterns of synthesized samples. XRD patterns of undoped and doped Cr_2O_3 crystals revealed the presence of only corundum structure. No other phases were found. The diffraction peaks of Sn/Cr_2O_3 shifted to lower angles, suggesting that the unit cell expands to accommodate the tin. This change is expected on tin replacing chromium ions in the lattice, as the ionic radii are 0.71 Å (Sn^{4+}) and 0.62 Å (Cr^{3+}). No shifting of peaks has been observed in case of W/Cr_2O_3 as ionic radii of Cr^{3+} and W^{6+} are similar.

Table 1 shows the lattice parameters 'a' and 'α' and cell volume 'V' of rhombohedral unit cell of pure and doped Cr_2O_3.

Fig. 2 represents FESEM micrographs of synthesized samples of chromium oxide where clusters and agglomerates are seen on the surface.

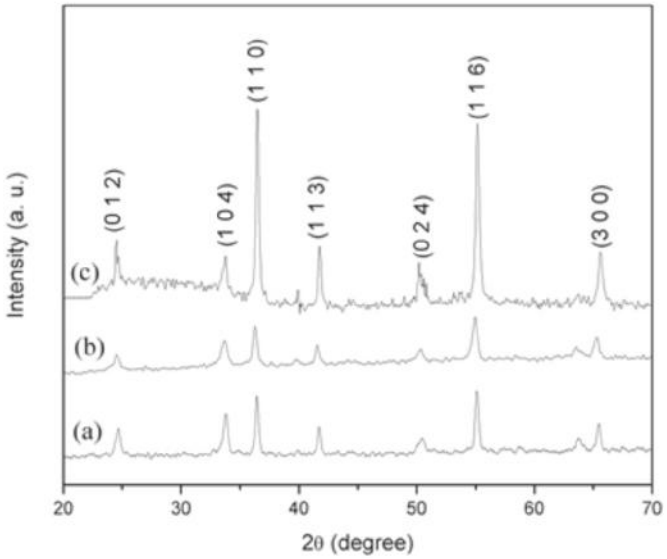

Fig1. *XRD patterns of (a) pure, (b) Sn/Cr_2O_3 and (c) W/Cr_2O_3 nanoparticles*

Table 1. *Lattice parameters of pure and doped chromium oxide*

Sample	a (in Å)	A (in degree)	V (in Å^3)
Pure Cr_2O_3	5.34	54.92	94.98
Sn/ Cr_2O_3	5.36	55.06	96.22
W/ Cr_2O_3	5.34	55	95.1

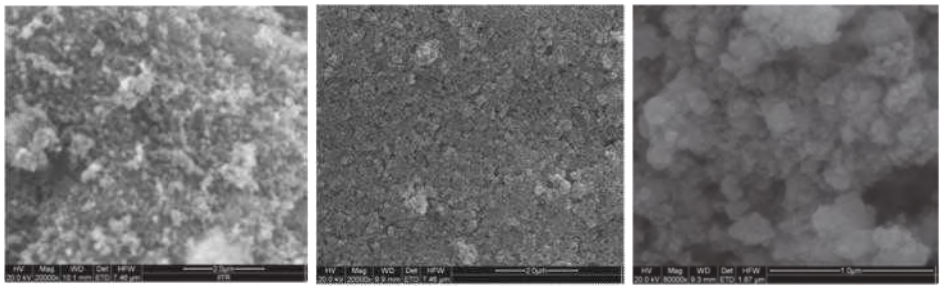

Fig 2. *FESEM micrographs of (a) pure, (b) Sn/Cr_2O_3 and (c) W/Cr_2O_3 nanoparticles.*

B. Gas Sensing Characteristics

Fabricated sensors were exposed to 250 ppm of ethanol and acetone vapour at different operating temperatures and results are shown in Fig. 3. It can be observed that optimum operable temperature of pure and doped sensors for both the gas species is same i.e. 250°C.

Moreover with the addition of Sn and W in $Cr_2O_3$the sensing response for ethanol and acetone has increased significantly. In p-type oxides, substitution of a low valent cation with higher valent cation in an oxide results in increased number of cation vacancies, consequently increased number of oxygen species adsorbed on the surface, and hence increased reactivity with test gas species [8].

It is also interesting to note from Fig. 4 that the fabricated sensor exhibited the higher response to acetone as compared to ethanol. Though gas sensing is a complex phenomenon still there are some of the obvious factors which might be playing crucial role in exhibiting this type of response variation. One of the plausible explanations could be on the basis of complete oxidation of these compounds and in the process consuming 8 and 6 O_{ads} by acetone and ethanol respectively. The reactions have been shown below in equations (1) and (2):

$$C_3H_6O + 8O \rightarrow 3CO_2 + 3H_2O + 8e \quad (1)$$

$$C_2H_5OH + 6O \rightarrow 2CO_2 + 3H_2O + 6e \quad (2)$$

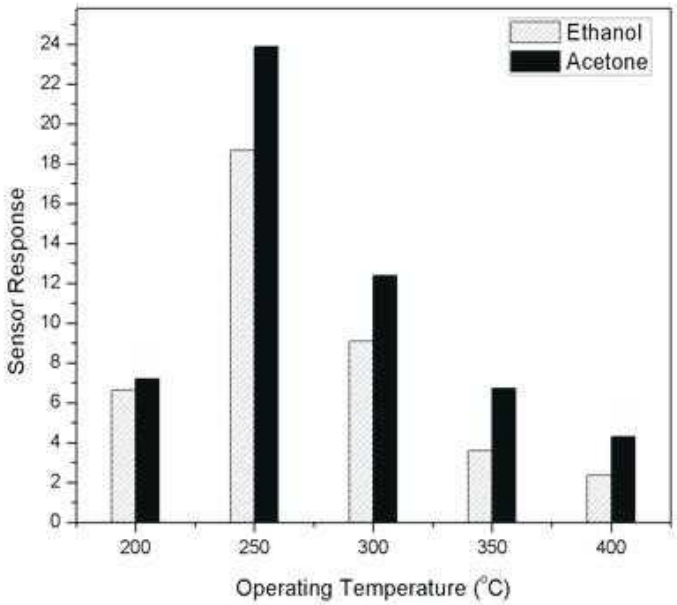

Fig 3. *Sensor response of pure Cr_2O_3 sensor at different operable temperatures towards 250 ppm ethanol and acetone.*

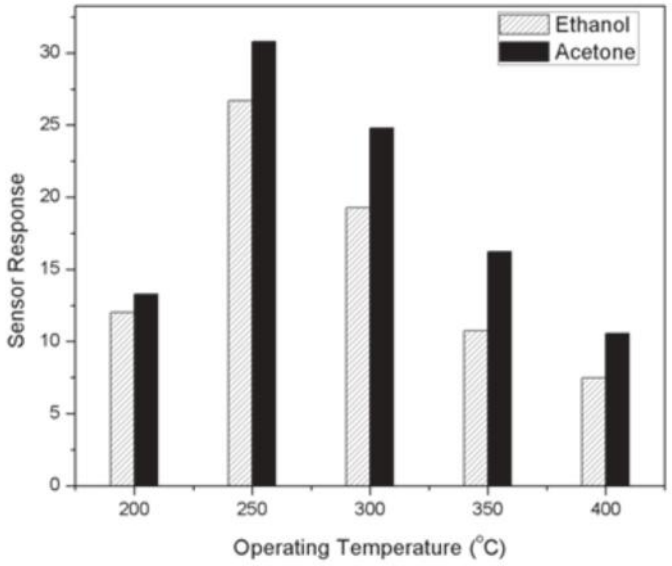

Fig 4. *Sensor response of Sn doped Cr_2O_3 sensor at different operable temperatures towards 250 ppm ethanol and acetone.*

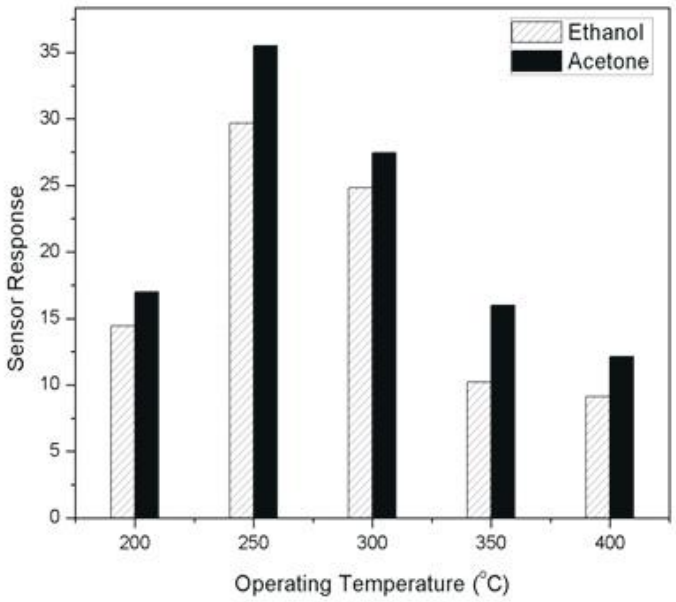

Fig 5. *Sensor response of W doped Cr_2O_3 sensor at different operable temperatures towards 250 ppm ethanol and acetone.*

IV. Results And Discussion

A chemical technique for the synthesis of pure and tin-doped Cr_2O_3 has been adopted. XRD results show the formation of corundum structure of Cr_2O_3. Expansion of unit cell has been observed due to the substitution of Cr^{3+} with Sn^{4+} but no such change has been observed due to substitution of Cr^{3+} with W^{6+}. Addition of tin and tungsten has increased the sensing response for alcohol significantly due to increased number of cation vacancies.

V. Acknowledgments

Authors would like to thank following: University Grants Commission, New Delhi, India for financial support; IIT Roorkee for FESEM investigations.

VI. References

[1] S.R. Morrison, "Semiconductor gas sensors" Sens. Actuators B 2 (1982) 329341.

[2] B. K. Miremadi, R. C. Singh, Z. Chen, S. R. Morrison, and K. Colbow,

"Chromium oxide gas sensors for the detection of oxygen and nitrogen oxide" Sens. Actuators B 21 (1994) 1-4.

[3] S. Pokhrel, Y. Ming, L. Huo, H. Zhao, S. Gao, "$Cr_{2-x}Ti_xO_3$ ($x \leq 0.5$) as CH_3COCH_3 sensitive resistors" Sens. Actuators B 125(2007) 550555.

[4] D. N. Suryawanshi, D. R. Patil, L. A. Patil, "Fe_2O_3-activated Cr_2O_3thick films as temperature dependent gas sensors" Sens. Actuators B 134 (2008) 579584.

[5] C. Cantalini, "Cr_2O_3, WO_3 single and Cr/W binary oxide prepared by physical methods for gas sensing applications" J. Eur. Ceram.Soc. 24 (2004)14211424.

[6] S. Morandi, E. Comini, G. Faglia, G. Ghiotti, "CrSn oxide thin films: Electrical and spectroscopic characterisation with CO, NO_2, $NH_3$and ethanol" Sens. Actuators B118 (2006) 142148.

[7] L. F. He, Y. Jia, F. L. Meng, M. Q. Li, J. H. Liu, "Development of sensors based on CuO-doped SnO_2 hollow spheres for ppb level H_2S gas sensing" J. Mater. Sci. 44 (2009) 4326-4333.

[8] J.R. Davis, Heat Resistant Materials, Materials Park: ASM International (1997). 4547.

Curr. Rep. Sci. & Tech. 2 (1) (2016) 31-41

Phase Separation Behavior of a Nonionic Surfactant in Presence of Electrolytes and Non Electrolytes

Reshu Sanan, Ayushi, Ashima Nayyar and Jatinder Singh Gandhi
P.G. Department of Chemistry, Khalsa College, Amritsar-143005 (INDIA)
reshusanan@gmail.com

Abstract

The present work is aimed at studying the phase separation behavior of nonionic surfactant, Igepal CO 720 in the presence of various electrolytes [sodium chloride (NaCl), magnesium chloride ($MgCl_2$), aluminium chloride ($AlCl_3$), sodium sulfate (Na_2SO_4), magnesium sulfate ($MgSO_4$), sodium oxalate ($Na_2C_2O_4$) and sodium acetate (CH_3COONa)] and non electrolytes [glucose, fructose, sucrose, glycine, urea, thiourea and L-ascorbic acid]. Owing to the salting-out nature of electrolytes, the CP of Igepal CO 720 got lowered in their presence. However, among non electrolytes, sugars and glycine act as CP depressors while urea, thiourea and L-ascorbic acid were found to be CP enhancers. Further the energetics of the clouding phenomenon in terms of standard free energy (ΔG_c^0), standard enthalpy (ΔH_c^0) and standard entropy (ΔS_c^0) of clouding have also been evaluated for Igepal CO 720 in the presence of various additives.

Keywords

Cloud point, Igepal CO 720, electrolytes, non electrolytes.

I. Introduction

A unique feature of nonionic surfactants is the presence of Cloud point (CP) curves, which represents the temperature above which precipitation or turbidity of an aqueous solution of a water-soluble surfactant starts, resulting from the dehydration of hydrophilic portion of micelles at higher temperature. This eventually causes its micelles to coalesce and grow to sizes which are large enough to make the solution turbid. This clouding behaviour of nonionic surfactants has considerable practical relevance. For

example, in preparing emulsions, the CP decides the most suitable surfactant for a given oil [1,2]. Several factors have been considered to be responsible for the CP phenomenon like structure of surfactant molecule, its concentration and the presence of additives [3-5].

Keeping this in view, we have investigated the effect of various electrolytes [such as sodium chloride (NaCl), magnesium chloride ($MgCl_2$), aluminium chloride ($AlCl_3$), sodium sulfate (Na_2SO_4), magnesium sulfate ($MgSO_4$), sodium oxalate ($Na_2C_2O_4$) and sodium acetate (CH_3COONa)] and non electrolytes [glucose, fructose, sucrose, glycine, urea, thiourea and L-ascorbic acid] on the clouding behaviour of Igepal CO 720. Igepal CO 720 belongs to nonionic polyoxyethylene surfactants having a nonyl chain attached to phenyl moiety as their hydrophobic tail and a chain of twelve ethylene oxide units as hydrophilic head group as shown in Fig. 1. It enjoys wide applicability in all phases of detergents compounding and aqueous processing in the textile and paper industries as well as industrial metal cleaners, acid cleaners etc [6,7]. In spite of being nontoxic and having a wide applicability, Igepal CO 720 has been least investigated and this formed the basis of our interest in this compound.

II. Experimental

Igepal CO 720 was obtained from Sigma Aldrich, while all electrolytes and non electrolytes were procured from S.D. Fine Chemicals, India. All chemicals were used as received and were of analytical grade. An analytical balance with a precision of ±0.0001g was used for weighing the amount of different substances. The solutions were prepared by dissolving accurately weighed quantities in requisite volumes of deionised double distilled water. The cloud point (CP) was measured visually when the solution of Igepal CO 720 suddenly appears to be turbid. The measuring solution was taken in test tubes suspended in an oil bath, whose temperature was increased gradually with constant stirring at a rate of about 0.1 $^0C\ min^{-1}$. The temperature at which turbidity first appeared was noted and heating was discontinued. The system then underwent self-cooling and temperature of disappearance of turbidity was noted. The average of two readings was taken as CP.

III. Results And Discussion

A. Phase Separation Behavior

Keeping in view the dependency of CP on the structure as well as the concentration of both surfactant and the additive, we firstly investigated the CP variation of Igepal CO 720 with concentration (Fig. 2). It was observed that the CP first decreases and then increases with increase in concentration, exhibiting a U-type curve typical of nonionic surfactants [8,9]. From this graph, a CP value of 359.95 K for 1% wv^{-1} Igepal CO 720 was taken for further studies.

Further the effect of various electrolytes viz. NaCl, $MgCl_2$, $AlCl_3$, Na_2SO_4, $MgSO_4$, CH_3COONa and $Na_2C_2O_4$, on the phase separation behavior of Igepal CO 720 (1% wv^{-1}) has been depicted in Fig. 3. It has been observed that the CP of Igepal CO 720 gets depressed in the presence of all electrolytes and this lowering of CP is found to depend on the concentration of electrolytes, where more is the concentration, greater is the depression in CP. This effect of electrolytes on the CP of nonionic surfactant can be explained on the basis of their salting-out nature. Ions, which are strong water-structure formers [5], increase the hydrogen bonding among water molecules, decrease the hydration of the ether groups of the surfactant, reducing its solubility, salting it out, and thus lowering its CP. Further, the added salts provide additional counterions to the existing systems and enhance counterion binding; as a result, the water of hydration is removed from the headgroup region, resulting in a decrease of their CP. A further observation from the studies on comparison of the various salts having common counterions is that more is the valency of the ion, greater is its effect on the depression of CP. At 1M concentrations of added salts, it can thus be inferred that the effect of cations varies as $Al^{3+} > Mg^{2+} > Na^{+}$ and that of anions as $SO_4^{2-} > Cl^{-}$ and $C_2O_4^{2-} > CH_3COO^{-}$.

Secondly, the effect of various non electrolytes viz. glucose, fructose, sucrose, glycine, L-ascorbic acid, urea and thiourea on the phase separation behavior of Igepal CO 720 was investigated. It was observed that the additives; glucose, fructose, sucrose and glycine lower the CP while urea, thiourea and L-ascorbic acid lead to an increase in the CP of Igepal CO 720 (Fig. 4). This effect of additives on the CP of nonionic surfactant can be

explained on the basis of their salting-out and salting-in nature. Sugars are well known water-structure makers, increase the hydrophobic interactions and decrease the cmc of surfactants [10]. The sugars decrease the water of hydration of the micelles by competing for water molecules associated with the micelles and hence, CP decreases in presence of sugars. Similarly, glycine having zwitterionic structure is highly solvated in aqueous medium. Because of this there is decrease in the availability of water molecules to hydrate the micelles. Hence at lower temperature micelles get dehydrated, van der Waals interaction occurs and lowering of CP occurs. On the other hand, urea acts in two different ways either by affecting the solvent (indirect mechanism) and facilitating the solvation of the hydrophobic species or by replacing the solvent (direct mechanism). The indirect mechanism is widely accepted, and many experimental results seem to support the hypothesis that urea acts as a water structure breaker [11]. In particular, the urea addition to micellar solutions leads to an increase in cmc [12] or decrease in aggregation number [13]. Urea acts as a water structure breaker and increases the CP. The same CP increasing effect is observed with thiourea but the effect is more than that of urea. The structure of thiourea closely resembles that of urea with less aqueous solubility and better thermal stability. Studies on thiourea surfactant systems show that thiourea is a better water-structure breaker compared with urea at similar concentrations. Water structure breakers increase the CP by making more water molecules available to the micelle. Here also, the lowering as well as the enhancing of CP is found to depend on the concentration of additives, more is the concentration, greater is the effect on CP.

B. Thermodynamics of Clouding

The separation of a homogeneous surfactant solution into two coexisting phases by releasing its solvated water at CP is an equilibrium process, for which concentration and activity are both equal (when considered ideal for calculation purposes). Hence the thermodynamic parameters for this clouding phenomenon, the standard Gibbs free energy of clouding (ΔG_c^0) can be calculated as per equation (1)

$$\Delta G_c^o = RT \ln x_c \quad (1)$$

where x_c represents the mole fraction of clouding species, R is the gas constant and T is the clouding temperature in Kelvin. Further the slope of $\Delta G_c^0/T$ vs. T plot can be used to determine the standard enthalpy of clouding (ΔH_c^0) following equation (2). These curves have two stages, the first stage being controlled by both enthalpy and entropy; $\Delta H_c^0 - T\Delta S_c^0$ and the other being enthalpy controlled; $\Delta H_c^0 > T\Delta S_c^0$ [14]. The standard entropy for clouding (ΔS_c^0) was in turn evaluated by use of equation. (3)

$$\Delta H_c^0 = -T^2\left[\frac{d\left(\Delta G_c^0/T\right)}{dT}\right] \quad (2)$$

$$T\Delta S_c^0 = \Delta H_c^0 - \Delta G_c^0 \quad (3)$$

These thermodynamic parameters have been evaluated for Igepal CO 720 in the presence of various additives and listed in Tables 1 and 2 for electrolytes and non electrolytes respectively. As expected, ΔG_c^0 has been found out to be negative for all the systems studied indicating that the clouding process proceeds spontaneously where as ΔH_c^0 and ΔS_c^0 values are positive or negative depending on the nature of the system. Clouding process is believed to occur by initial dehydration of PEO chains followed by association of the dehydrated molecules [15,16]. The first process is endothermic and increases the entropy, whereas the second one is exothermic and decreases the entropy. The negative ΔH_c^0 and ΔS_c^0 values thus indicates

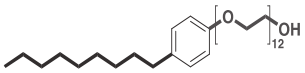

Fig 1. *Structure of Igepal CO 720.*

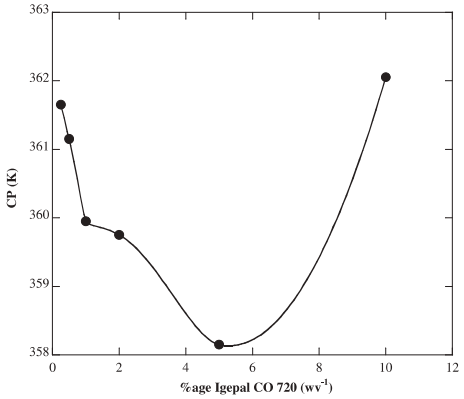

Fig 2. *Plot showing concentration vs. cloud point for Igepal CO 720.*

that the association process overrides the dehydration step as the formation of larger aggregates involves release of heat with overall ordering of the system [17]. However, positive values of ΔH_c^0 and ΔS_c^0 suggest that interplay of both the dehydration and the association processes changes the balance between hydrophilic and hydrophobic interactions and thus the temperature dependent interaction parameters come into play [18].

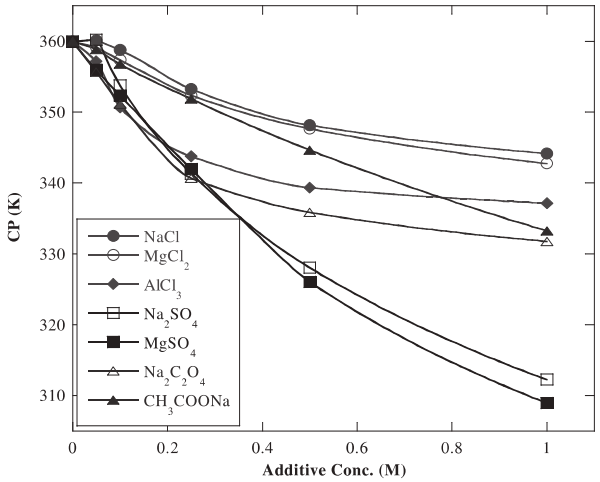

Fig 3. *Plots showing the effect of different concentrations of various electrolytes on cloud point of Igepal CO 720 (1%wv-1%wv^{-1}).*

Reshu Sanan

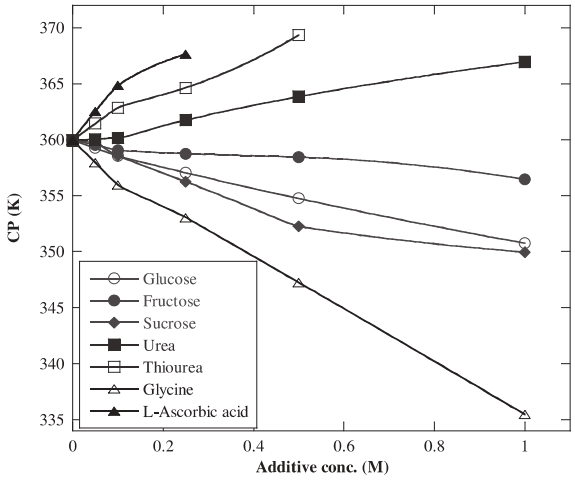

Fig 4. *Plots showing the effect of different concentrations of various non electrolytes on cloud point of Igepal CO 720 (1%wv^{-1}).*

IV. Conclusions

The phase separation behavior of Igepal CO 720 has been studied in the presence of different concentrations (0.05M, 0.1M, 0.25M, 0.5M and 1.0M) of various electrolytes and non electrolytes using Cloud point measurements. It was observed that the CP of Igepal CO 720 gets depressed in the presence of all electrolytes (NaCl, $MgCl_2$, $AlCl_3$, Na_2SO_4, $MgSO_4$, $Na_2C_2O_4$ and CH_3COONa) owing to their salting-out nature. Further more is the concentration of the added electrolyte, greater is the depression in CP. Also, among various electrolytes the depression in CP is observed to be directly dependent on the charge of the ion where the effect on CP of Igepal CO 720 varies as $Al^{3+} > Mg^{2+} > Na^{+}$ for cations and $SO_4^{2-} > Cl^{-}$ and $C_2O_4^{2-} > CH_3COO^{-}$ for anions. Regarding non electrolytes, sugars (glucose, fructose, sucrose) and glycine decreased the CP of Igepal CO 720, while urea, thiourea and L-ascorbic acid, were found to increase the CP of Igepal CO 720. This has been attributed to their different type of behavior towards water molecules with the former ones acting as strong water structure makers while the latter ones are water structure breakers. Although the structure of thiourea closely resembles with that of urea, yet it exhibited a greater effect than urea at similar concentrations. The thermodynamics of clouding phenomenon for Igepal CO 720 gave negative ΔG_c^0 values in presence of all the additives, signifying the feasibility of clouding process where as ΔH_c^0 and ΔS_c^0 values were positive or negative depending on the nature of the system.

Table 1. *Thermodynamics of the clouding behavior for Igepal CO 720 in the presence of various electrolytes.*

Additive	**[Additive] (M)**	ΔG^0_c **(kJmol^{-1})**	ΔH^0_c **(kJmol^{-1})**	ΔS^0_c **(kJmol^{-1})**
NaCl	0.05	-22.6	-533.7	-1.42
	0.10	-24.5	-529.6	-1.41
	0.25	-26.9	-161.1	-0.38
	0.50	-28.4	-156.5	-0.37
	1.00	-30.1	-152.9	-0.35
$MgCl_2$	0.05	-22.5	-412.7	-1.09
	0.10	-24.4	-408.6	-1.07
	0.25	-26.8	-161.8	-0.38

	0.50	-28.4	-157.5	-0.37
	1.00	-30.0	-153.1	-0.36
$AlCl_3$	0.05	-22.4	-136.9	-0.32
	0.10	-23.9	-131.9	-0.31
	0.25	-26.1	-126.8	-0.29
	0.50	-27.8	-301.6	-0.81
	1.00	-29.5	-297.7	-0.79
Na_2SO_4	0.05	-22.6	-51.3	-0.08
	0.10	-24.2	-49.4	-0.07
	0.25	-25.9	-46.0	-0.06
	0.50	-26.8	-74.8	-0.15
	1.00	-27.3	-67.8	-0.13
$MgSO_4$	0.05	-22.3	-114.8	-0.26
	0.10	-24.1	-112.5	-0.25
	0.25	-26.0	-105.9	-0.23
	0.50	-26.7	-37.1	-0.03
	1.00	-27.0	-33.3	-0.02
$Na_2C_2O_4$	0.05	-22.3	-109.0	-0.24
	0.10	-24.0	-106.3	-0.23
	0.25	-25.9	-100.0	-0.22
	0.50	-27.5	-145.7	-0.35
	1.00	29.0	-142.2	-0.34
CH_3COONa	0.05	-22.5	-238.0	-0.60
	0.10	-24.4	-235.2	-0.59
	0.25	-26.8	-228.8	-0.58
	0.50	-28.2	-72.3	-0.13
	1.00	-29.2	-67.6	-0.12

Table 2. *Thermodynamics of the clouding behavior for Igepal CO 720 in the presence of various non electrolytes.*

Additive	**[Additive] (M)**	**ΔG^0_c (kJmol^{-1})**	**ΔH^0_c (kJmol^{-1})**	**ΔS^0_c (kJmol^{-1})**
Glucose	0.05	-22.5	-764.3	-2.06
	0.10	-24.5	-761.3	-2.05
	0.25	-27.1	-227.7	-0.56
	0.50	-29.0	-224.8	-0.55
	1.00	-30.7	-219.7	-0.54
Fructose	0.05	-22.5	-2285.7	-6.29
	0.10	-24.6	-2279.4	-6.28
	0.25	-27.3	-2275.6	-6.27

	0.50	-29.3	-370.2	-0.95
	1.00	-31.2	-366.1	-0.94
Sucrose	0.05	-22.5	-485.8	-1.29
	0.10	-24.5	-482.6	-1.28
	0.25	-27.1	-317.9	-0.82
	0.50	-28.8	-178.8	-0.43
	1.00	-30.6	-176.5	-0.42
Glycine	0.05	-22.4	-348.9	-0.91
	0.10	-24.3	-345.0	-0.90
	0.25	-26.8	-339.4	-0.89
	0.50	-28.4	-76.0	-0.14
	1.00	-29.4	-70.9	-0.12
Urea	0.05	-22.6	375.3	1.04
	0.10	-24.6	377.6	1.05
	0.25	-27.5	7565.6	20.9
	0.50	-29.8	7655.6	21.0
	1.00	-32.1	7788.5	21.2
Thiourea	0.05	-22.6	569.1	1.57
	0.10	-24.8	575.6	1.58
	0.25	-27.7	190.7	0.52
	0.50	-30.2	197.5	0.53
L-Ascorbic acid	0.05	-22.7	367.9	1.01
	0.10	-25.0	374.5	1.03
	0.25	-28.0	382.9	1.04

V. References

[1] L.A.M. Rupert, "A thermodynamic model of clouding in water/alcohol ethoxylate mixtures," J. Colloid Interface Sci. 153 (1992) 92-105.

[2] A.T. Florence, F. Madsen, F. Puisieux, "Emulsion stabilization by non-ionic surfactants: the relevance of surfactant cloud point," J. Pharm. Pharmacol. 27 (1975) 385-394.

[3] R. Sanan, R.K. Mahajan, "Polyethylene Glycol Assisted Micellar, Interfacial and Phase Separation Studies of Triblock Copolymer - Nonionic Surfactant Mixtures," Colloids Surf. A 433 (2013) 145-153.

[4] K.S. Sharma, S.R. Patil, A.K. Rakshit, "Study of the cloud point of C12En nonionic surfactants: effect of additives," Colloids Surf. A 219 (2003) 67-74.

[5] S. Mahajan, A. Shaheen, T.S. Banipal, R.K. Mahajan, "Cloud Point

and Surface Tension Studies of Triblock Copolymer-Ionic Surfactant Mixed Systems in the Presence of Amino Acids or Dipeptides and Electrolytes," J. Chem. Eng. Data 5 (2010) 3995-4001.

[6] M.A. Sedgwick, D.C. Crans, N.E. Levinger, "What Is Inside a Nonionic Reverse Micelle? Probing the Interior of Igepal Reverse Micelles Using Decavanadate," Langmuir 25 (2009) 5496-5503.

[7] S.S. Mati, T.K. Mondal, S. Dhar, S. Chall, S.C. Bhattacharya, "Differential contribution of Igepal and CnTAB micelles on the photophysics of nonsteroidal drug Naproxen," Spectrochimica Acta Part A 92 (2012) 122-130.

[8] L. Koshy, A.H. Saiyad, A.K. Rakshit, "The effects of various foreign substances on the cloud point of Triton X 100 and Triton X 114," Colloid Polym. Sci. 274 (1996) 582-587.

[9] R. Heusch, BTF-Biotech. Forum 3 (1986) 1.

[10] R. Kjellander, E. Florin, "Water structure and changes in thermal stability of the system poly(ethylene oxide)water," J. Chem. Soc. Faraday Trans. 77 (1981) 2053-2077.

[11] M. Manabe, M. Koda, K. Shirahama, "The effect of 1-alkanols on ionization of sodium dodecyl sulfate micelles," J. Colloid Interface Sci. 77 (1980) 189-194.

[12] M. Abu-Hamdiyyah, K. Kumari, "Solubilization tendency of 1-alkanols and hydrophobic interaction in sodium lauryl sulfate in ordinary water, heavy water, and urea solutions," J. Phys. Chem. 94 (1990) 6445-6452.

[13] F.G. Briganti, S. Puvvada, D. Blankschtein, "Effect of urea on micellar properties of aqueous solutions of nonionic surfactants," J. Phys. Chem. 95 (1991) 8989-8995.

[14] M.S. Alam, Kabir-ud-Din, A.B. Mandal, "Evaluation of Thermodynamic Parameters of Amphiphilic Tricyclic Antidepressant Drug Imipramine Hydrochloride-Additive Systems at the Cloud Point," Colloids Surf. B 76 (2010) 577-584.

[15] M. Prasad, S.P. Moulik, D. Chisholm, R. Palepu, "Influence of Hydrotropes and Glycols on the Clouding Behavior of Surfactants (TritonX 100 and Brij 56) and Polymers (Polyvinylmethyl Ether and

Triblock Co-Polymer, Pluronic 85),” J. Oleo. Sci. 52 (2003) 523-534.

[16] A. van Bommel, R.M. Palepu, “n-Alkanol induced clouding of Brij® 56 and the energetics of the process,” Colloids Surf. A 233 (2004) 109-115.

[17] M.S. Alam, Kabir-ud-Din, A.B. Mandal, “Thermodynamics at the Cloud Point of Phenothiazine Drug Chlorpromazine Hydrochloride-Additive Systems,” J. Chem. Eng. Data 55 (2010) 1693-1699.

[18] T. Inoue, H. Ohmura, D. Murata, “Cloud point temperature of polyoxyethylene-type nonionic surfactants and their mixtures,” J. Colloid Interface Sci. 258 (2003) 374-382.

Curr. Rep. Sci. & Tech. 2 (1) (2016) 42-57

Thermodynamic Properties of Hydrogen plasma with Electronic Excitation

Gurpreet Singh
Department of Physics, DAV College, Bathinda-151001, India.
gurpreet.dav@gmail.com

Abstract

The thermodynamic properties of local thermodynamic equilibrium (LTE) atomic hydrogen thermal plasmas with electronically excited states (EES) have been studied in the temperature range 10000K to 50000K and over a wide range of pressures. Two cases have been considered (i) ground state (GS) plasma, in which all the species are assumed to be in the ground state and (ii) excited state (ES) plasma, in which all the atomic species are distributed over various possible excited states. The number of excited states to be included in the partition function depends upon temperature and pressure. It has been observed that the properties have shown a strong dependence on the presence of EES. The electronic excitation affects both frozen and reactive specific heats but compensation takes place for the total specific heat at low pressures. At high pressures, this compensation fails for the total specific heat, while the effect of EES on isentropic coefficient is modest.

Keywords

Thermal plasma, Saha's ionization equation, Electronic excitation, Thermodynamic properties

I. Introduction

Thermal plasmas have wide industrial applications [1,2,4-6] which include arc welding, plasma spraying, plasma torches used for plasma cutting and waste destruction. It has also an immense application in astrophysical phenomenon [3, 4]. Overall plasma must be electrically neutral, which is known as quasi-neutrality. Low electric field and high pressures are the basic requirements for the existence of LTE in plasmas [4]. The theoretical

modeling of plasmas for a wide range of temperatures and pressures include the accurate calculation of composition, thermodynamic and transport properties. The evaluation of these properties has widely gained importance in the recent years and a particular emphasis has been given to high pressure and high temperature plasmas. When the ionization degree decreases, the electronically excited states (EES) increase their role in affecting the thermodynamic properties of the plasmas [7, 8]. Less attention has been devoted to the role of EES in affecting the thermodynamic properties of the thermal plasmas as there is large underestimation of influence of EES. The reasons of this underestimation are essentially due to the small differences reported by different authors [9-15], when thermodynamic properties are compared by using partition functions of the atomic species allowing only the ground-state term and the corresponding values including all electronic states. The above statement is a consequence of a sort of compensation between various contributions of a given thermodynamic property, for example, there is compensation between the different contributions (i.e. frozen and reactive) of the total specific heat. In particular, the insertion of electronically excited states in the whole thermodynamic properties increases the frozen specific heat compared with the corresponding quantity calculated by neglecting the electronically excited states, the reverse being true for the reactive contribution. This largely explains the insensitivity of the total thermodynamic quantities to the internal excitation of atomic species. So, a refinement of the partition functions of these species is required.

The paper is divided as follows: In section II, through the partition function, the role of electronic excitation on the composition of ground state (GS), excited state (ES) and variation of degree of ionization with temperatures and at different pressures for hydrogen thermal plasmas has been evaluated. In section III, expression for various thermodynamic properties viz. enthalpy (H), specific heat at constant pressure (C_p), isentropic coefficient (γ) and internal specific heat ($\frac{C_{V_H}}{R}$) are presented. The expressions for the various thermodynamic properties have been written in terms of the degree of ionization and the partition function. The results and discussion is presented in section IV. Finally, detailed discussion of the role of electronically excited states in affecting

the various thermodynamic properties of hydrogen plasma has been presented in section V.

II. Partition Function

Thermodynamic properties of thermal plasmas can be easily calculated once the composition of the system is known, which in many cases can be described by the Saha equation. The ionization state of a gas in equilibrium at temperature T can be found using Saha's equation. There is a

$$\frac{n_e n_{H^+}}{n_H} = \left(\frac{2\pi mkT}{h^2}\right)^{3/2} \frac{2}{f_H} \exp\left(\frac{-I_H}{kT}\right) \tag{1}$$

separate Saha equation for each pair (j; j + 1) of ionization states associated with each element present in the gas. These equations have to be solved simultaneously, together with an equation governing charge conservation which ultimately sets the electron number density n_e. For hydrogen, to determine the electron number density n_e, we can take advantage of charge conservation. The total number density n is given by $n = n_H + n_{H+} + n_e$ and the total pressure $p = nkT$. Equation (1) can be rewritten in terms of ionization.

$$\alpha = \left(\frac{n_e}{n_H + n_{H^+}}\right) \text{ as}$$

$$\frac{\alpha^2}{(1-\alpha^2)} p = \left(\frac{2\pi mkT}{h^2}\right)^{3/2} kT \frac{2}{f_H} \exp\left(\frac{-I_H}{kT}\right) \tag{2}$$

degree of where f_H is the electronic partition function and I_H is the ionization energy of atomic hydrogen n_e, n_H and n_H +are the number densities of electrons, H- atoms and protons respectively.

A. Equilibrium composition of ground state (GS) and excited state (ES) plasmas

The concentration of electron X_e, hydrogen ion X_H and hydrogen atom X_H in the ground state plasma at p=1, 10 and 100 atm respectively have been evaluated at different temperatures. It has been observed that $X_e = X_{H+}$ at high pressure (i.e. p=100 atm) is less as compared to that at low pressure [11] because ionization of hydrogen atoms take place at a high temperature

with increase in pressure. Atomic hydrogen in the excited state plasma is divided into the different possible excited states depending upon pressure and temperature. We thus obtain the excited state plasma (e, H^+, H (n)) with n=1, 2, 3 …, n_{max} where n_{max} =12, 12 and 7 have been used in the calculation at p=1, 10 and 100atm respectively.

The relative concentration of the i^{th} atomic excited state is obtained by

$$\frac{n_i}{n_T} = \frac{g_i}{Z(T)} \exp(-E_i/kT)$$
$$\text{with} \quad Z(T) = \sum g_i e^{-E_i/kT} \tag{3}$$

where n_i, g_i and E_i are the number density, degeneracy and energy of the 2^{th} atomic excited state respectively and are the total number density and electronic partition function of atomic hydrogen. The partition function, called the sum over the states is the sum of the products of the statistical weights of the energy states of an atom multiplied by the Boltzmann factors. As the Boltzmann factors remain practically constant and the statistical weights grow with the increase in energy of the levels, this sum diverges for an isolated atom due to the existence of an infinite number of energy levels. To evaluate the partition function of the atoms in a partially ionized perfect gas in thermodynamic equilibrium, it is necessary to find the last internal level an atom can have under the temperature and pressure conditions in the gas. Furthermore, once the maximum level is known, one should attempt to find the sum, to calculate the partition function of a chemical element for plasmas.

The problem of the divergence of the partition function is overcome in the literature [7, 15] by cutting the sum to an n_{max} which in the case of atomic hydrogen can be written in different ways according to different physical conditions. A simple cutoff criterion based upon confined- atom (CA) model is adopted [7], i.e. by considering excited states with classical Bohr radius not exceeding the interparticle distance. The criterion thus

$$a_o n_{max}^2 = (1/n')^{1/3} \tag{4}$$

obtained is where a_o is the Bohr radius and $n' = p/kT$ is the total number

density of hydrogen atoms. All the excited states with the principal quantum number $n \leqslant n_{max}$ should be considered in the partition function. Thus, the partition function f_H depends upon pressure and temperature. Fig. 1 displays the variation of partition f_H function vs. temperature at different pressures.

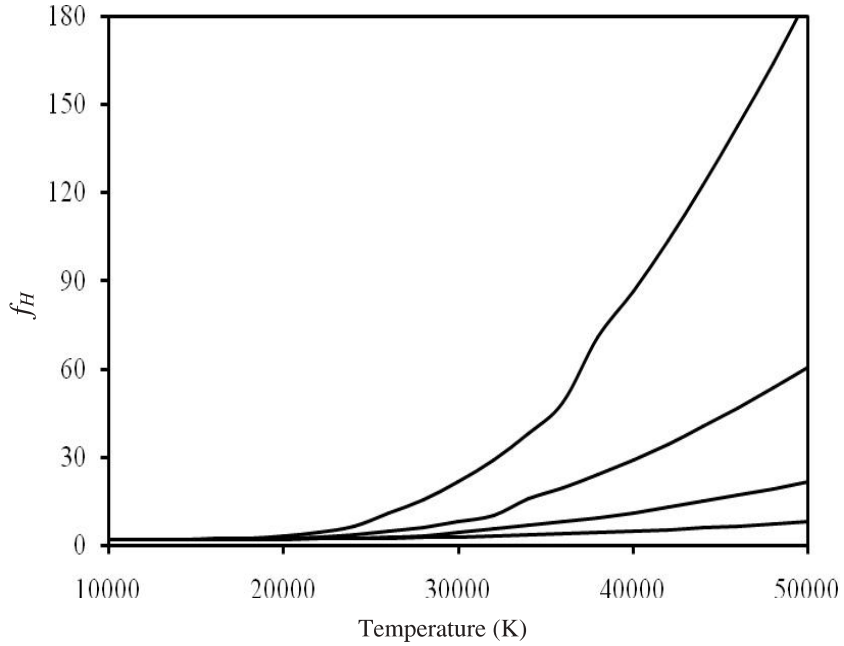

Fig 1. Partition function f_H vs. temperature. Curves (upper to lower) represent p=1, 10, 100 & 1000 atm respectively.

It has been observed that with increase in pressure, the concentration of the excited states increases as well as the maxima $X_{H(n)}$ of shifts towards higher temperature.

B. Variation of degree of ionization with temperature and pressure

Using computer program based upon above equations , degree of ionization has been evaluated at different pressures over a wide range of temperature (i.e. from 10000-50000 K). Its variation with temperature has displayed in Fig. 2 for both GS and ES plasmas at p=1 and 100 atm. It is clear that with increase of pressure, the degree of ionization for ES plasma become less than that for GS plasma.

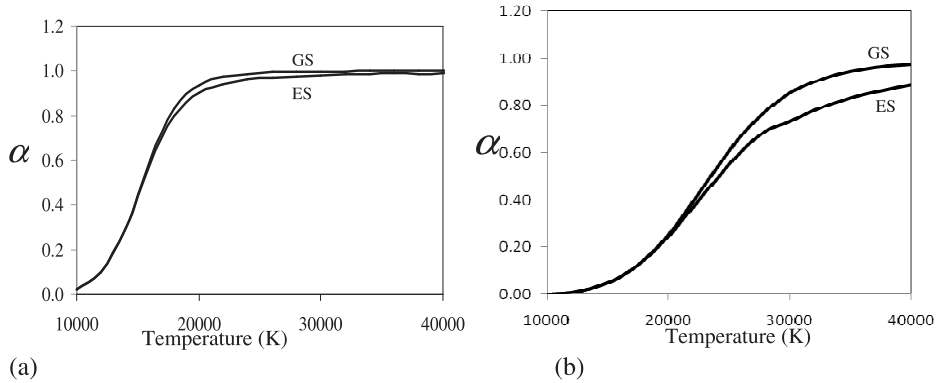

***Fig 2**. Degree of ionization vs. Temperature for GS and ES at (a) p=1 atm and at (b) 100 atm.*

III. Thermodynamic properties: Expressions

The expressions for thermodynamic properties such as enthalpy, specific heat at constant pressure and isentropic coefficient for GS and ES hydrogen plasma has been presented.

A. Enthalpy

Among the thermodynamic properties, the most important for plasma modelling are the enthalpy H, its derivative with respect to temperature T, and the specific heat at constant pressure C_p. The peaks on these curves correspond to dissociation mechanisms at low or intermediate temperatures (around 4000 K for H_2, and 7000 K for N_2 at atmospheric pressure) and to ionization at high temperatures (mainly around 15000K for many species having an ionization energy around 1015 eV).

Starting with one mole of atomic hydrogen, then at a given temperature H, H^+ and e have 1-α,α and α moles respectively, where α is the degree of ionization defined by

$$\alpha = n_e / n_N = \frac{n_e}{n_H + n_{H^+}} , \tag{5}$$

where n_N, n_H and n_H are the number densities of nuclei, H atoms and protons respectively. Total enthalpy of this three component plasma (H, H^+, e) is

$$H = (1-\alpha)H_H + \alpha H^+ + \alpha H_e \tag{6}$$

where H_H, H_{H+} and He are the molar enthalpies of H atoms, protons and electrons given by

$$H_H = \frac{5}{2}RT + E_H + \frac{D}{2}$$

$$H_e = \frac{5}{2}RT$$

$$H_{H^+} = \frac{5}{2}RT + \frac{D}{2} + I_H$$

where $^5/_2$RT , D, I_H and E_H are the translational molar enthalpy of each species, dissociation energy of H_2 , the ionization energy of H atoms and the electronic energy of atomic hydrogen respectively. Thus, $^D/_2$ and $^D/_2$+I_H are the chemical enthalpy of atomic hydrogen and protons. Thus, total enthalpy of hydrogen plasma is given by

$$H = \frac{5}{2}(1+\alpha)RT + (1-\alpha)E_H + \frac{D}{2} + \alpha I_H$$

The second term in the above equation is the internal enthalpy with E_H given by

$$E_H = RT^2\left(\frac{\partial \ln f_H}{\partial T}\right) \tag{7}$$

where f_H is the internal partition function defined by

$$f_H = \sum g_n \exp(-\frac{\varepsilon_n}{kT}) \tag{8}$$

with

$$\varepsilon_n = I_H\left(1-\frac{1}{n^2}\right)$$

and $g_n = 2n^2$

where n denotes the principal quantum number of atomic hydrogen and g_n is the statistical weight.

B. Specific heat at constant pressure

When the derivative of total enthalpy H is taken with respect to temperature T at constant pressure , the dependence of the degree of ionization with temperature must be considered. Thus, we define two specific heats, the first one, called frozen specific heat is obtained by taking derivative of the total enthalpy with respect to temperature at constant whereas in the second one, called reactive specific heat of the plasma, this constraint is eliminated.

Thus, the total specific heat of the hydrogen plasma is given by

$$c_p = c_{pf} + c_{pr} \tag{9}$$

where the frozen specific heat C_{pf} is

$$c_{pf} = \left(\frac{\partial H}{\partial T}\right)_p = \frac{5}{2}(1+\alpha)RT + (1-\alpha)c_{VH} \tag{10}$$

where C_{VH} is the internal specific heat of atomic hydrogen and is given by

$$c_{VH} = \left(\frac{\partial E_H}{\partial T}\right)_V = R\left[\frac{\partial \ln f_H}{\partial \ln T} + \frac{\partial^2 \ln f_H}{\partial^2 \ln T}\right] \tag{11}$$

with f_H as the electronic partition function of atomic hydrogen. The reactive specific heat is given by

$$c_{pr} = \left(\frac{\partial H}{\partial \alpha}\right)_{p,\alpha}\left(\frac{\partial \alpha}{\partial T}\right)_p = \left(\frac{5}{2}RT + I_H - E_H\right)\left(\frac{\partial \alpha}{\partial T}\right)_p$$

$$c_{pr} = \frac{1}{RT^2}\frac{\alpha(1-\alpha^2)}{2}\left(\frac{5}{2} + I_H - E_H\right)^2 \tag{12}$$

where the degree of ionization α and its derivative $(\partial\alpha/\partial T)p$ have been obtained from the Saha's equation.

C. Isentropic coefficient (γ)

For the isentropic coefficient γ (c_p/c_v), we have

$$\gamma = \left[\frac{\frac{1}{RT^2}\alpha(1-\alpha)(I_H + \frac{5}{2}RT - E_H)^2 + (1+\alpha)\frac{5}{2}R + (1-\alpha)c_{VH}}{\frac{1}{RT^2}\frac{\alpha(1-\alpha)}{(2-\alpha)}(I_H + \frac{3}{2}RT - E_H)^2 + (1+\alpha)\frac{3}{2}R + (1-\alpha)c_{VH}}\right] \tag{13}$$

D. Internal specific heat

The internal specific heat of atomic hydrogen C_{VH} depends upon first and second derivative of the partition function and can be written as

$$\frac{c_{VH}}{R} = \left(\overline{E}^2 - \overline{E^2}\right) \times \left(\frac{11{,}600}{T}\right)^2$$

which is the product of two factors. The first factor is sharp peaked curve at low pressure due to large number of excited states whereas it is a flattened curve at high pressure due to smaller number of excited states. The second factor is parabolically decreasing with

temperature. The variation of frozen and reactive specific heats for both GS and ES plasmas at low and high pressures is presented in Figure 3 & 4 respectively.

The internal contribution c_{int} to the frozen part c_{pf} of the specific heat is again the product of two factors (i) (1-α), the molar fraction of H atoms and (ii) $\frac{C_{VH}}{R}$ The role of electronically excited states (EES) in affecting thermodynamic properties of hydrogen thermal plasma has been examined over a wide range of temperature and pressure by taking GS and ES plasmas. The enthalpy for GS and ES plasma, total specific heat at constant pressure C_p along with its frozen and reactive contributions have been worked out in detail for both the cases. Their pressure and temperature dependence has been depicted graphically.

IV. Results and Discussion

The method of computation starts with the determination of electronic partition function which through Saha equation gives the degree of ionization. At a given temperature, the number of excited states to be inserted in the partition function depends upon pressure, thus the partition function varies with pressure. In order to estimate the effect of including the EES in the atomic partition function and its derivatives, specific heat at constant pressure, C_p $(C_{pf} + C_{pr})$ where C_{pf} and C_{pr} are the frozen and reactive contributions to the specific heat, has been evaluated in the temperature range 10000K to 50000K and at different pressures. The frozen part C_{pf} is further the sum of the translational and internal contributions i.e. $C_{pf} = {}^5/_2$ RT + $C_{int.}$ The ratios C_{int}/C_{pf} and C_{int}/C_p have been worked out for hydrogen thermal plasma in the temperature range 10000-50000 K and in the pressure range 1-100atm. Following the same approach, the ratios of specific heats at constant pressure to the specific heat at constant volume C_V i.e. γ (called the isentropic coefficient) have been studied and the role of electronic excitation has been discussed.

The enthalpy for the hydrogen plasma has been evaluated. The effect of electronically excited states on the enthalpy has been graphically depicted in figure 3 by the plot of $\frac{H_{ES}}{H_{GS}}$ for GS and ES hydrogen plasma at different pressures.

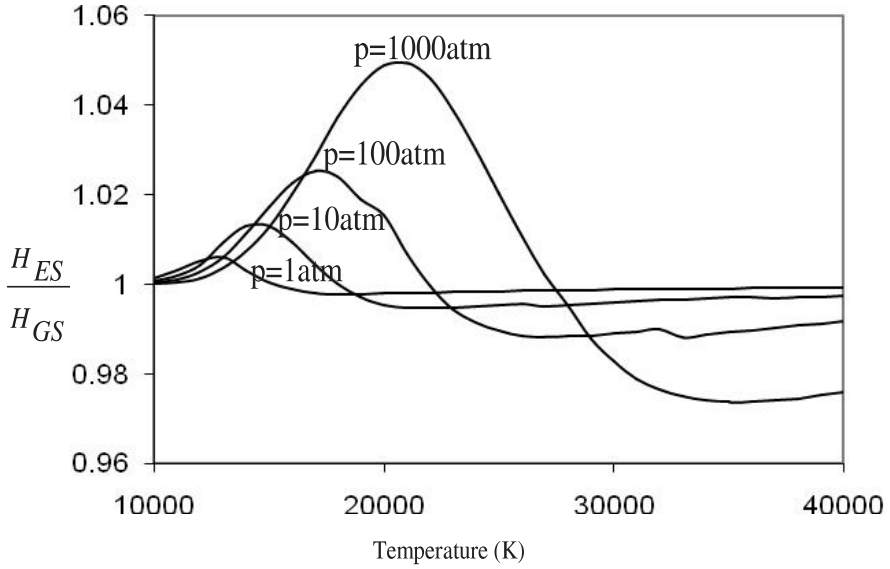

Fig 3. *Ratio of enthalpy for GS and ES hydrogen plasma at different pressures pressures.*

The number of excited states to be included in the partition function is first determined using a simple cutoff criterion (based on confined atom (CA) model). Then a computer program has been developed to compute the degree of ionization and the various contributions to the specific heat at different pressures in the temperature range 10000-50000 K. The results thus obtained for C_{pf} and C_{pr} are presented in Fig. 4 *and* 5 for p=1 and 100 atm respectively The comparison of results of for the excited state (ES) plasma with those of the ground state (GS) plasma have been made in Figure 6 which displays the variation of the ratio $\frac{c_p(ES)}{c_p(GS)}$ with temperature for p=1,10,100 and 1000 atm respectively.

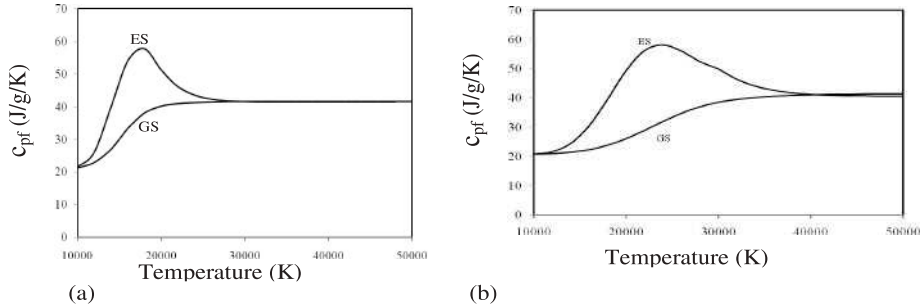

Fig 4. *Frozen specific heat C_{pf} vs. Temperature for ES and GS hydrogen plasmas at (a) p=1 atm (b) p=100 atm.*

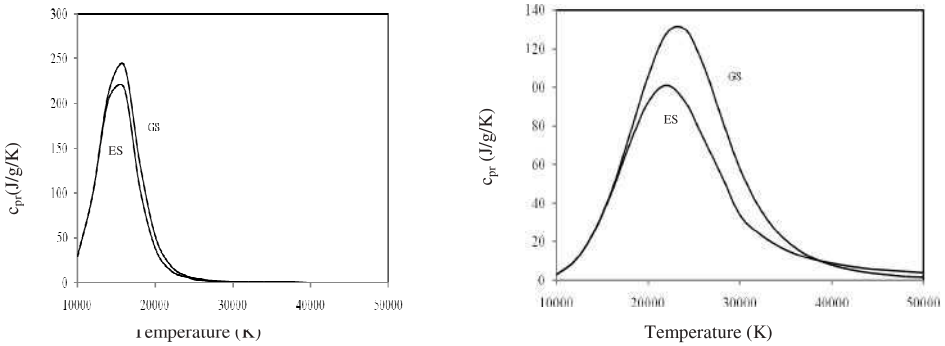

Fig 5. *Reactive specific heat c_{pr} vs. Temperature for ES and GS hydrogen plasmas at (a) p=1 atm (b) p=100 atm.*

The role of electronic excitation on the frozen contribution of specific heat c_{int} has been discussed and is given by

$$c_{\text{int}} = (1-\alpha)c_{VH}$$

where the degree of ionization and the internal specific heat of atomic hydrogen C_{VH} depend upon electronic partition function. Comparison of with and has been attempted by plotting the ratios and c_{int}/c_{pf} *and* c_{int}/c_p with temperature at different pressures in figures 7 respectively. It may be mentioned here that c_{pf} is the sum of internal and translational contributions i.e.

$$c_{pf} = \frac{5}{2}(1+\alpha)RT + c_{\text{int}}.$$

Hence, it has been observed that

(i) as pressure increases, the partition function decreases, due to the ionization of atoms occurs at high temperature and hence concentration of EES increases (Fig. 1)

(ii) the value of c_{pr} for ES plasma is lower than that of the GS plasma in the region where electronic excitation is dominant (Fig. 5). Ground state results overestimate the reactive contribution by about 15% at p=100 atm. This is due to the fact that the electronic energy EH of the atomic hydrogen appears in the expression for c_{pr} with negative sign in equation12.

(iii) at low pressure p=1 atm, the internal contributions in c_{pf} and cancel each other leading to a sort of compensation which is not observed at high pressures p=10-10_3atm. The deviation of results for GS and

ES plasmas are more emphatically displayed in Fig. 6 where the ratio $\frac{c_p(ES)}{c_p(GS)}$ does not behave monotonically, rather maxima and minima are observed at a given pressure. The differences strongly increase with increase of pressure. But for $p \leq 1$ atm these differences are negligible i.e. the ratio is practically independent of temperature. This fact mislead researchers in past for not considering electronically excited states in calculating thermodynamic properties of LTE plasmas.

(iv) Regarding the estimation of internal contribution to specific heat, Fig. 7 displays maxima of $\frac{c_{\text{int}}}{c_{pf}}$ at all pressures. At p=103 atm, this ratio is greater than 0.5 i.e. contribution due to electronic excitation is higher than the translational one. On the other hand, the ratio c_{int}/c_p behaves in a similar way to that c_{int}/c_{pf} of but the corresponding maxima decrease due to the negative role played by the electronic excitation in the reactive contribution C_{pr} of the specific heat. At $p=10_3$ atm, c_{int}/c_p =0.25 indicating thereby that the internal contribution is not negligible at high pressures.

(v) Internal specific heat (Fig. 8) is a function of temperature as well as pressure and enthalpy for excited states (ES) plasmas is greater than ground state (GS).

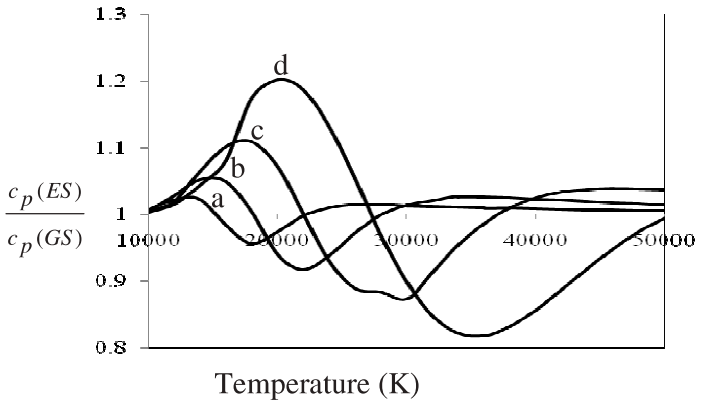

Fig 6. $\frac{c_p(ES)}{c_p(GS)}$ ***vs.*** *temperature. Curves a, b, c & d represent p= 1, 10, 100& 100 atm respectively.*

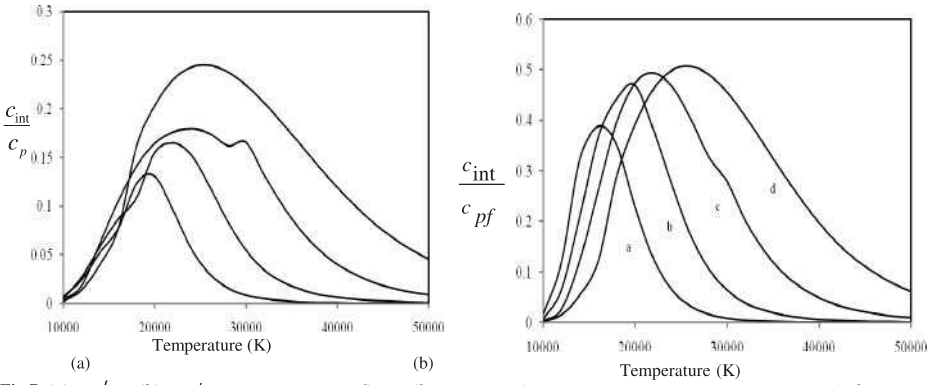

Fig 7. *(a)* c_{int} / c_p *,(b)* c_{int} / c_{pf} *vs. temperature. Curves (lower to upper) represent , ctively.*

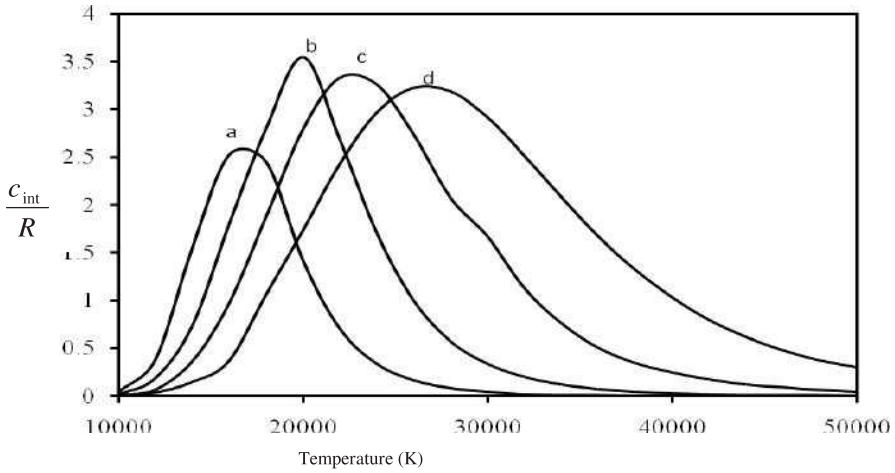

Fig 8. $\frac{c_{int}}{R}$ *vs. temperature. Curves a, b, c & d represent p=1, 10 &100atm respectively.*

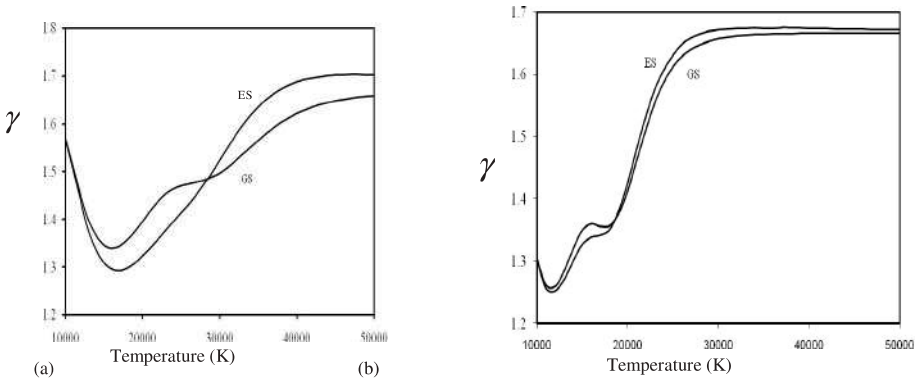

Fig 9. *Isentropic coefficient vs. Temperature for ES and GS hydrogen plasmas at (a) p=1 atm (b) p=100 atm.*

The peak observed for the excited state (ES) plasma is due to the addition of cint , thereby indicating the role of EES. With increase of pressure, ionization shifts towards high temperature thereby, shifting the peak of cint for ES plasma towards high temperature.

(vi) the contribution of electronic excitation tends to disappear in the total isentropic coefficient which include translation, electronic and reactive components (Fig. 9). In fact, the computed values for GS and ES plasmas differ by not more than 7.5% due to some compensation in different terms of [Equation 13]. Thus, the contribution of electronic excitation makes its presence felt to total specific heat at high pressures but not as emphatically as in the case of frozen specific heat.

V. Conclusion

The thermodynamic properties of a LTE hydrogen plasma depend upon the number of electronically excited states (EES) to be inserted in the partition function. This inclusion of EES increases the partition function thereby affecting the degree of ionization and the internal specific heat of high temperature atomic hydrogen plasmas especially at high pressures. Its strong dependence on the frozen specific heat of the plasma mixture has been observed but the effect is negligible on the total specific heat due to compensation between the frozen and reactive contributions to the total specific heat at low pressure. This compensation fails at pressures higher than one atm. Hence, the equilibrium properties such as enthalpy and specific heat depend upon EES. The isentropic exponent also depends upon the EES at low pressures whereas the difference between its GS and ES value at high pressures is modest. The importance of internal energy in affecting the frozen and total specific heat of plasma at high pressure is confirmed by both criteria. A non ideal approach can be used in future work on the subject [12-14], especially for the high-pressure case. The approach could also introduce a better cutoff criterion based on the density, based on quantum statistical mechanics. The extension of these ideas on the other hand, to other atomic plasmas (N and O) should take into account the so-called low lying excited

states, as well as the electronic levels above the first ionization limit of atoms.

VI. Acknowledgments

The author is thankful to colleagues of the Department of Physics, DAV College Bathinda for their encouragement and giving helpful suggestion.

VII. References

[1]. J.J. Lowke, R. Morrow, J. Haidar, and A.B. Murphy, "Prediction of gas tungsten arc welding properties in mixtures of argon and hydrogen" IEEE Trans. Plasma Sci. 25 (1997) 925-930.

[2]. P. Fauchais, and A.Vardelle, Thermal plasmas. IEEE Trans. Plasma Sci. 25(1997) 1258-1280.

[3]. M., Capitelli, G., Colonna, D., Giordano, L., Marraffa, A., Casavola, P., Minelli, D., Pagano, D., Pietanza, and F., Taccogna, "High-Temperature Thermodynamic Properties of Mars-Atmosphere Components," Journal of Spacecraft and Rockets, 42 (2005) 980989.

[4]. M.I. Boulos, P. Fauchais, and E., Pfender, Thermal plasmas: Fundamental and Applications, Vol. 1 (1994) Plenum Press, New York.

[5]. P.M.Campbell, Transport phenomena in a completely ionized gas with large temperature gradients Physical Review A 30 (1984) 365-373.

[6]. M.Capitelli, R Celiberto, C Gorse, A Laricchiuta, D Pagano, P Traversa "Transport properties of local thermodynamic equilibrium hydrogen plasmas including electronically excited states" Phys Rev E 69 (2004) 026412.

[7]. M Capitelli, A Laricchiuta, D Pagano, P Traversa "Electronically excited states and transport properties of thermal plasmas : the viscosity" Chem Phys Lett. 379 (2003) 490.

[8]. B. Sourd P. Andre´ J. Aubreton M.F. Elchinger" Influence of the excited states of atomic nitrogen N(2D), N(2 P) on the Transport properties of nitrogen part I: Atomic nitrogen properties". Plasma Chem Plasma Process 27(2007) 225240.

[9]. D. Bruno, M. Capitelli, C. Catalfamo, and A. Laricchiuta, "Cutoff criteria of electronic partition functions and transport properties of atomic hydrogen thermal plasmas" Phys Plasmas 15, (2008)112306.

[10]. G.,Singh and K Singh, Estimation of higher-order contribution to viscosity of hydrogen plasmas including electronically excited states". *Phys. Plasmas* 13 (2006) 122309-4.

[11]. G., Singh, R., Sharma, and K Singh, "Effect of excited states on higher-order contributions to electron transport in hydrogen thermal plasmas". J. Phys. D: Appl. Phys. 41(2008) 225203-7.

[12]. G., Singh, R. Sharma, and K. Singh, "Electron transport in hydrogen thermal plasmas". J. Plasma Fusion Res. SERIES 8(2009)1344-1347.

[13]. F. De Palma, A.R. Casavola and M. Capitelli, "Influence of electronic excitation on the thermodynamic properties of hydrogen plasmas". J. Thermophys. Heat Trans. 20 (2006). 921-925.

[14]. D. Bruno, M. Capitelli, C. Catalfamo and Laricchiuta," A Cutoff criteria of electronic partition functions and transport properties of atomic hydrogen thermal plasmas". Phys. Plasmas 15 (2008) 112306-7.

[15]. P. Kovitya, "Thermodynamic Properties of High-Temperature Plasmas," *IEEE Transactions on Plasma Science,* Vol. PS-13 (1985) p. 587.

Curr. Rep. Sci. & Tech. 2 (1) (2016) 58-72

A Zinc-acetic Acid Interceded Reductive Cleavage of 3-dienyl-2-azetidinone NDA Cycloadducts: A facile en route to Novel β-lactam Tetehered 4-amino alcohols

Amit Anand
Department of Chemistry, Khalsa College Amritsar, Punjab
aa_wiz@yahoo.com

Abstract

Amino alcohols are important class of organic compounds for their key roles in many biological and medicinal activities. Extensive efforts have been made for the selective synthesis of amino alcohols and there are a number of reports in the literature, but majority of them involves cumbersome experimental procedures with low yields. The selective reduction of nitroso Diels-Alder cycloadducts of 3-dienyl-2-azetidinone with Zinc/Acetic acid reduction protocol providing a facile and high yielding en route to novel, unnatural and biologically important 1,4-disubstituted-3-(1-hydroxy-4-(phenylamino)but-2-enyl)-1) azetidin-2-ones is reported.

Keywords

β-lactam, amino alcohols, zinc, acetic acid.

I. Introduction

Amino alcohols are attractive compounds, either as ligands for asymmetric stereoselective catalysis [1] or as building blocks for the preparation of biologically active molecules.[2] Some of the chiral amino alcohols are important constituent of natural products, such as cinchonine, cinchonidine, quinine, quinidine, ephedrine and norephedrine.[3] Thus, the construction of this important structural motif attracts extensive efforts by organic chemists. Developing efficient and novel methods to prepare amino alcohols remains one of the major challenges. Many inroads have been made in this regard which include hydrogenation of pthalimido ketone,[4] reductive cross-coupling of chiral *N-tert*-butanesulfinyl imines with aldehydes,[5] Indium trichloride catalyzed Mukaiyama aldol reaction

of keto ester, [6] amino ketones reduction [7] and the reductive cleavage of 3,6-dihydro-1,2-oxazines.[8] 3,6-dihydro-1, 2-oxazines are valuable synthetic intermediates which have found applications in numerous total syntheses of biologically relevant targets due to their regio- and stereoselective synthesis using nitroso Diels-Alder reaction. The cycloadduct may be used as a temporary protection which can be deprotected or transformed selectively in the synthesis *via* most usually the reductive cleavage of the NO bond.[9] The numerous methods that have been developed for the cleavage of the NO bond can be listed under three different types: (a) radical-mediated,[10] (b) anionic mediated (with[11] or without[12] quaternarization reaction of the nitrogen atom) and (c) metal-mediated. The latter class includes the majority of the reduction conditions, based on sodium or aluminium amalgam,[13] zinc in acetic acid,[14] $LiAlH_4$,[15] molybdenum[16] or samarium[17] complexes, indium[18] and catalytic hydrogenation over Pd/C, $Pd(OH)_2$, PtO_2 or Raney Ni.[19] Most of these approaches require harsh reaction conditions (such as strongly acidic medium at elevated temperature)[14] or lead to the undesired side reactions and/or rearrangements.[20] On the other hand, some reductive methods do not allow the selective NO bond cleavage in the presence of other reducible functional groups.

Recently, Madsen *et.al* have devised a new method for the synthesis of vicinal alcohols which employs a Barbier-type reaction between an imine and 3-benzoyloxyallyl bromide in the presence of zinc metal.[21] Whiting *et. al* have demonstrated a one-pot synthesis of chiral amino alcohols from ,-unsaturated aldehydes which circumvents competitive 1,2- versus 1,4-boryl addition, by means of using a sterically hindered amine-derived imine.[22] Tam *et. al.* have demonstrated the first example of rhodium-catalyzed ring-opening reactions of 3-aza-2-oxabicyclo [2.2.1] hept-5-ene with arylboronic acids.[23] They have also reported unprecedented Ru catalyzed nucleophilic ring-opening reactions of 3-aza-2-oxabicyclo[2.2.1]hept-5-ene with alcohols. The reactions were found to be highly regioselective, giving only the substituted 1,2-cyclopentenes.[24] Miller *et. al.* have established that a variety of 3-aza-2-oxabicyclo[2.2.1]hept-5-ene and [2.2.2]oct-5-ene systems can be

solvolytically ring-opened under $In(OTf)_3$ catalyzed conditions. The regio- and stereoselectivity of the products obtained depends on the co-solvents and/or the size of the nucleophiles. Anti-1,2 and anti-1,4-alkoxy hydroxyamino- disubstituted cyclohexene products were obtained from [2.2.2] bicyclic systems whereas anti-1,2, anti-1,4 and syn-1,4 were obtained from [2.2.1] bicyclic systems.[25] Kouklovsky *et. al.* have recently shown that carbonyl compounds having an α-hetero substituent, such as 2,2-dimethyl-1,3-dioxan-5-one or preferably 1,3-dithiolan-2-carboxaldehyde, react with salts of 1,2-oxazine to achieve efficiently the cleavage of the NO bond under mild conditions. The corresponding 1,4-*cis* aminoalcohols are isolated in good to excellent yield, without metal contamination, inherent to classical reducing methods.[26]

Thus a significant number of reports have appeared concerning the nitroso Diels-Alder cycloaddition of various cyclic and acyclic dienes with nitroso dienophiles and their transformation to corresponding amino alcohols. The literature rationale, however, suggests only a few reports on successful ultilisation of a heterocyclic ring substituted 1,3-diene in various versions of NDA cycloadditions. Mahajan *et. al.* have successfully developed an alternate convenient single step route for the synthesis of heterocyclic ring substituted 1,3-butadienes by successful utilization of *in situ* generated butadienyl ketene in their cycloaddition reactions with various imines and 1,3-diaza-1,3-butadienes leading to the formation of the formation of 3-butadienyl-2-azetidinones and 5-dienyl-pyrimidinones respectively.[27,28,29] The DA cycloaddition reactions of 3-butadienyl-2-azetidinones and 5-dienyl pyrimidinones were studied in refluxing toluene with symmetrical and unsymmetrical dienophiles. The reactions were non diastereoselective and resulted in the formation of mixtures of regio- and diastereoisomers.[30] The catalytic, Lewis acid interceded andπ-facially selective DA cycloaddition reactions with various symmetrical and unsymmetrical carbon dienophiles were however, highly stereoselective and resulted in the formation of a exclusive endo adduct.[31] The Imino Diels-Alder cycloadditons (IDA) of 3-dienyl-2- azetidinones with various imines resulted in formation of the quinoline derivatives in which the dienyl component of 3-dienyl-2-azetidinones, interestingly participated as

2π component while the *N*-aryl imines participated as 4π components of fused 2-azadienes.[32]

II. Result and Discussion

The regio - and distereoselective Nitroso Diels - Alder(NDA) cycloadducts 3a-r were previously reported to be prepared by the treatment of 1a-i with 1.1 *eq* of nitrosoarenes 2a-b in dry dichloromethane for 6-7hr at room temperature in excellent yields (80-90%) (Scheme 1).[33]

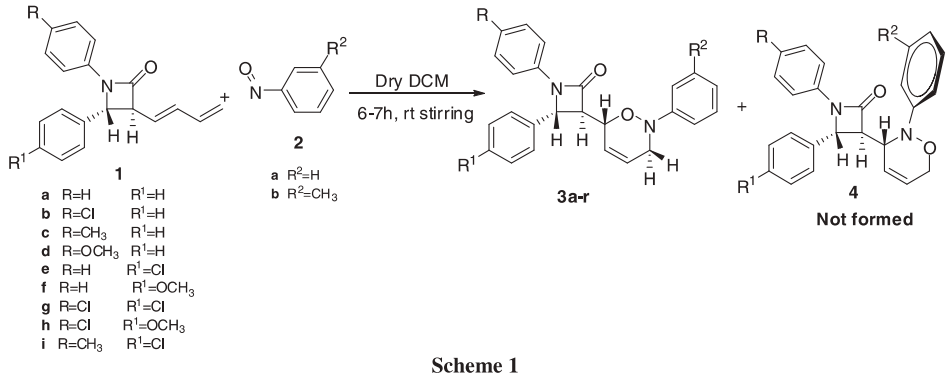

Scheme 1

The observedπ-facial selectivity probably stems from the preferred *Re* face approach of nitrosoarene to the most preferred s-cisoid confirmation of *N*-aryl 3-dienyl-2-azetidinones due to the lesser steric interactions offered by proton of the third carbon of the azetidinone ring during such progression. The π-facial, regio- and distereoselective NDA cycloadducts were characterized on the basis of analytical evidences and spectral data.[33]

The treatment of a solution NDA cycloadducts 3a-r & in minimum amounts of glacial acetic acid with zinc powder for 4-5hr at room temperature resulted in the good yields (65-75%) of previously unknown amino alcohol tethered β-lactams 5a-r (Scheme 2, Table 1).

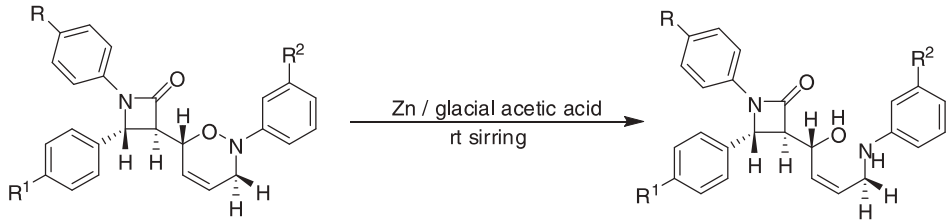

Scheme 2

Table 1: N-O bond cleavage of 3-oxazine tethered 2-azetidinones **3**:

Entry	R	R^1	R^2	Reaction Time(hr)	% Yield of 5
5a	H	H	H	4.0	74
5b	Cl	H	H	4.2	75
5c	CH_3	H	H	4.5	68
5d	OCH_3	H	H	4.9	68
5e	H	Cl	H	4.2	75
5f	H	OCH_3	H	4.7	65
5g	Cl	Cl	H	4.1	74
5h	Cl	OCH_3	H	4.6	68
5i	CH_3	Cl	H	4.3	66
5j	H	H	CH_3	4.2	74
5k	Cl	H	CH_3	4.4	73
5l	CH_3	H	CH_3	4.4	67
5m	OCH_3	H	CH_3	4.9	71
5n	H	Cl	CH_3	4.5	75
5o	H	OCH_3	CH_3	5.0	72
5p	Cl	Cl	CH_3	4.4	75
5q	Cl	OCH_3	CH_3	4.2	66
5r	CH_3	Cl	CH_3	4.4	69

[a]All the reactions were conducted using glacial acetic acid as solvent. [b]The spectra of crude adducts show the formation of single isomer. [c]Yields of adducts were measured prior to crystallization

The diastereomerically pure amino alcohals 5a-r, so obtained, were characterized as 1,4-disubstituted-3-(1-hydroxy-4-(phenylamino)but-2-enyl)-1) azetidin-2-ones on the basis of analytical data and spectral evidences, the details of which are described in the experimental section while the salient features are discussed here. The compound 5a, for example, analyzed for $C_{25}H_{24}N_2O_2$ showed the molecular ion peak at 384. Its IR spectrum exhibited a sharp absorption at 1748 cm^{-1} due to the carbonyl of the lactam ring, a broad absorption at 3357cm^{-1} assigned to intramolecularly hydrogen bonded OH group. The salient features of the ^1H spectrum includes a doublet of a doublet at 3.44(*J*=2.4 Hz, 5.4 Hz) corresponding to H^3, a broad peak at 3.51 due to exchangeable NH proton, a doublet of doublet of an AB quartet at 3.75(*J*=0.9Hz, 5.4Hz, 5.7Hz, 16.2 Hz) due to H^{8a} and H^{8b}, a doublet at 5.01-5.07(*J*=5.4 Hz) corresponding to H^5, a doublet at 5.11-5.12(*J*=2.4 Hz) due to H^4, an resolved multiplet at 5.61-5.80 assigned to H^6 and H^7. Its ^{13}C spectra also attest the presence of the required carbons along with a characteristic methylene carbon at 52.5 and carbonyl peak at 164.8. The disappearance of an NH peak at 3.51, coupling of 0.9 Hz with NH proton in the presence of D_2O and the appearance of molecular ion peak at 384 in its mass spectrum further confirms the formation of *N*-substituted amino alcohols tethered 2-azetidinone 5a (Figure 1).

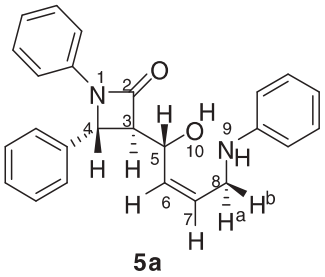

5a

Figure 1

The amino alcohols 5a-r are further being explored in their intramolecular nucleophilic amidiolysis employing the well known β-lactam synthon methodology.

III. Experimental

Melting points were determined by open capillary using Veego Precision Digital Melting Point apparatus (MP-D) and are uncorrected. IR spectra were recorded on a Shimadzu D-8001 spectrophotometer. ^{1}H NMR spectra were recorded in deuterochloroform with Joel (300 MHz) spectrometers using TMS as internal standard. Chemical shift values are expressed as ppm downfield from TMS and *J* values are in Hz. Splitting patterns are indicated as s: singlet, d: doublet, t: triplet, m: multiplet, q: quartet, br: broad peak and brs: broad singlet. ^{13}C NMR spectra were also recorded on Joel 300 (75.0 MHz) spectrometers in deuterochloroform using TMS as internal standard. Mass spectra were recorded on Shimadzu GCMS-QP-2000 mass spectrometer. Elemental analyses were performed on Heraus CHN-O-Rapid Elemental Analyzer. Column chromatography was performed on a silica gel (60120) mesh Harrison Research Chromatotron using 2 mm plates (Silica gel 60 PF254). *Trans*-3-dienyl-azetidin-2ones were prepared by the reported methods using *N*-alkyl imines.

General method for the synthesis of 3-(1-hydroxy-4-(phenylamino) but-2-enyl)-azetidin-2-ones.

To the solution of 5-dihydroxazinyl-2-azetidinones **3**(1.0 mmol) in glacial acetic acid, zinc powder (2.0 m mol) was added in small lots and the reaction mixture was stirred at rt for 0.5-1.0 hr. The progress of the reaction was checked with the help of TLC monitoring. After the completion of the

reaction, the reaction mixture was vigorously washed with ice cold saturated aqueous $NaHCO_3$ and extracted in CH_2Cl_2. The mixture was concentrated under *vacuo* and the crude reaction mixture thus obtained was chromatographed on 60-120-mesh silica gel to yield 5-(4-amino alcohol) substituted 2-azetidinones **5** [eluent: 1: 4 EtOAc: hexane]. The products were recrystallized from 1: 4 EtOAc: hexane.

5a. 3-(1-hydroxy-4-(phenylamino)but-2-enyl)-1,4-diphenylazetidin-2-one:

Pale Yellow solid, M. p.: 123-124 °C, δ_H ($CDCl_3$, 300 MHz), 3.44(dd, 1H, J= 2.4 Hz,5.7 Hz, H_3), 3.75(ddABq, 2H, J=0.9Hz, 5.4 Hz, 5.7Hz, 16.2Hz, -CH_2), 5.05(d, 1H, J=5.4 Hz, H_5), 5.12(d, 1H, J=2.4 Hz, H_4), 5.72(m, 2H, $H_{6,7}$), 6.88-7.34(m, 15H, ArH, aromatic). δ_C ($CDCl_3$, 75 MHz), 49.4, 57.5, 60.2, 69.7, 115.7, 116.6, 122.3, 123.8, 124.5, 125.9, 126.7, 128.1, 129.0, 129.1, 129.3, 137.2, 138.0, 146.2, 164.5. m/z 384 (M^+). ν_{max} (KBr)/cm^{-1} 1505, 1745, 3345, 3395cm^{-1}. Anal. Calc. for $C_{25}H_{24}N_2O_2$: C, 78.10; H, 6.29; N, 7.29; Found C, 78.37; H, 6.44, N, 7.15.

5b. 1-(4-chlorophenyl)-3-(1-hydroxy-4-(phenylamino)but-2-enyl)-4-phenylazetidin-2-one:

Pale Yellow solid, M. p.: 125-126 °C, δ_H ($CDCl_3$, 300 MHz), 3.43(dd, 1H, *J*=2.4 Hz, 5.7 Hz, H_3), 3.76(ddABq, 2H, *J*=0.9Hz, 5.4 Hz, 5.7Hz, 16.2Hz, -CH_2), 5.06(d, 1H, *J*=5.7 Hz, H_5), 5.14(d, 1H, *J*=2.4 Hz, H_4), 5.73(m, 2H, $H_{6,7}$*), 6.86-7.32(m, 14H, ArH, aromatic).* δ_C ($CDCl_3$, 75 MHz), 49.3, 57.4, 60.2, 69.8, 115.5, 116.4, 122.3, 123.9, 124.6, 125.9, 126.8, 128.4, 129.0, 129.2, 136.1, 137.3, 138.2, 146.4, 164.3. m/z 418 (M^+). ν_{max} (KBr)/cm^{-1} 1504, 17425, 3347, 3390cm^{-1}. Anal. Calc. for $C_{25}H_{23}ClN_2O_2$: C, 71.68; H, 5.53; N, 6.69; Found C, 71.79; H, 5.77; N, 6.50.

5c. 3-(1-hydroxy-4-(phenylamino)but-2-enyl)-4-phenyl-1-*p*-tolylazetidin-2-one:

Pale Yellow solid, M. p.: 124-125 °C, δ_H ($CDCl_3$, 300 MHz), 2.26(s, 3H, -CH_3), 3.44(dd, 1H, J= 2.4 Hz, 5.4 Hz, H_3), 3.77(ddABq, 2H, J=0.9Hz, 5.4 Hz, 5.7Hz, 16.2Hz, -CH_2), 5.03(d, 1H, J=5.7Hz, H_5), 5.13(d, 1H, J=2.4Hz, H_4), 5.76(m, 2H, $H_{6,7}$), 6.85-7.35(m, 14H, ArH, aromatic). δ_C ($CDCl_3$, 75 MHz), 30.8, 49.5, 57.3, 60.5, 69.8, 115.3, 116.5, 122.2, 123.8, 124.3, 125.9,

126.7, 128.0, 129.1, 129.5, 135.6, 137.5, 138.1, 146.3, 164.4. m/z 398 (M^+). ν_{max} (KBr)/cm^{-1} 1507, 1740, 3350, 3392cm^{-1}. Anal. Calc. for $C_{26}H_{26}N_2O_2$: C, 78.36; H, 6.58; N, 7.03; Found C, 78.52; H, 6.74; N, 6.90.

5d. 3-(1-hydroxy-4-(phenylamino)but-2-enyl)-1-(4 methoxyphenyl)-4-phenylazetidin-2-one:

Pale Yellow solid, M. p.: 133-134 °C, δ_H ($CDCl_3$, 300 MHz), 3.44(dd, 1H, *J*=2.4 Hz, 5.7 Hz, H_3), 3.76(s, 3H, -OCH_3), 3.77(ddABq, 2H, *J*=0.9Hz, 5.4 Hz, 5.7Hz, 16.2Hz, -CH_2), 5.02(d, 1H, *J*=5.7 Hz, H_5), 5.12(d, 1H, *J*=2.4 Hz, H_4), 5.78(m, 2H, $H_{6,7}$), 6.80-7.32(m, 14H, ArH, aromatic). δ_C ($CDCl_3$, 75 MHz), 49.3, 55.8, 57.4, 60.5, 69.9, 115.6, 116.7, 122.1, 123.7, 124.4, 125.9, 126.5, 128.0, 129.2, 129.3, 137.2, 138.0, 146.2, 154.3, 164.3. m/z 414 (M^+). ν_{max} (KBr)/cm^{-1} 1503, 1742, 3340, 3393cm^{-1}. Anal. Calc. for $C_{26}H_{26}N_2O_3$: C, 75.34; H, 6.32; N, 6.76; Found C, 75.51; H, 6.48; N, 6.19.

5e. 4-(4-chlorophenyl)-3-(1-hydroxy-4-(phenylamino)but-2-enyl)-1-phenylazetidin-2-one:

Pale Yellow solid, M. p.: 135-136 °C, δ_H ($CDCl_3$, 300 MHz), 3.42(dd, 1H, *J*=2.4 Hz, 5.7 Hz, H_3), 3.78(ddABq, 2H, *J*=0.9Hz, 5.4 Hz, 5.7Hz, 16.2Hz, -CH_2), 5.02(d, 1H, *J*=5.7 Hz, H_5), 5.14(d, 1H, *J*=2.4 Hz, H_4), 5.79(m, 2H, $H_{6,7}$), 6.80-7.30(m, 14H, ArH, aromatic). δ_C ($CDCl_3$, 75 MHz), 49.3, 57.6, 60.2, 69.5, 115.2, 116.5, 122.1, 123.2, 124.4, 125.8, 126.7, 128.1, 129.0, 129.3, 132.5, 137.5, 138.2, 146.4, 164.2. m/z 419 (M^+). ν_{max} (KBr)/cm^{-1} 1503, 1740, 3340, 3391cm^{-1}. Anal. Calc. for $C_{25}H_{23}ClN_2O_2$: C, 71.68; H, 5.53; N, 6.69; Found C, C, 71.88; H, 5.72; N, 6.52.

5f. 3-(1-hydroxy-4-(phenylamino)but-2-enyl)-4-(4-methoxyphenyl)-1-phenylazetidin-2-one:

Pale Yellow solid, M. p.: 130-131 °C, δ_H ($CDCl_3$, 300 MHz), 3.44(dd, 1H, *J*= 2.4 Hz, 5.7 Hz, H_3), 3.74(s, 3H, -OCH_3), 3.79(ddABq, 2H, *J*=0.9Hz, 5.4 Hz, 5.7Hz, 16.2Hz, -CH_2), 5.02(d, 1H, *J*=5.7 Hz, H_5), 5.12(d, 1H, *J*=2.4 Hz, H_4), 5.80(m, 2H, $H_{6,7}$), 6.85-7.32(m, 14H, ArH, aromatic). δ_C ($CDCl_3$, 75 MHz), 49.4, 55.4, 57.4, 60.1, 69.8, 115.7, 116.6, 122.1, 123.9, 124.6, 126.8, 128.3, 129.0, 129.2, 129.3, 137.2, 138.3, 146.1, 155.6, 164.2. m/z 414 (M^+). ν_{max} (KBr)/cm^{-1} 1502, 1743, 3346, 3394cm^{-1}. Anal. Calc. for $C_{25}H_{26}N_2O_2$: C, 75.34; H, 6.32; N, 6.76; Found C, 75.50; H, 6.49; N, 6.55.

5g. 1,4-bis(4-chlorophenyl)-3-(1-hydroxy-4-(phenylamino)but-2-enyl)azetidin-2-one:

Pale Yellow solid, M. p.: 135-136 °C, δ_H ($CDCl_3$, 300 MHz), 3.44(dd, 1H, *J*=2.4 Hz, 5.7 Hz, H_3), 3.80(ddABq, 2H, *J*=0.9Hz, 5.4 Hz, 5.7Hz, 16.2Hz, -CH_2), 5.03(d, 1H, *J*=5.7 Hz, H_5), 5.16(d, 1H, *J*=2.4 Hz, H_4), 5.88(m, 2H, $H_{6,7}$), 6.80-7.30(m, 13H, ArH, aromatic). δ_C ($CDCl_3$, 75 MHz), 49.3, 57.4, 60.5, 70.0, 115.6, 116.7, 122.4, 123.9, 124.6, 125.9, 126.7, 129.1, 129.3, 133.5, 135.6, 137.2, 138.0, 146.2, 164.5. m/z 452 (M^+). ν_{max} (KBr)/cm^{-1} 1503, 1744, 3341, 3388cm^{-1}. Anal. Calc. for $C_{25}H_{22}Cl_2N_2O_2$: C, 66.23; H, 4.89; N, 6.18; Found C, 66.40; H, 4.99; N, 6.01.

5h. 31-(4-chlorophenyl)-3-(1-hydroxy-4-(phenylamino)but-2-enyl)-4-(4-methoxyphenyl)azetidin-2-one:

Pale Yellow solid, M. p.: 129-130 °C, δ_H ($CDCl_3$, 300 MHz), 3.43(dd, 1H, *J*=2.4 Hz, 6.0 Hz, H_3), 3.77(s, 3H, -OCH_3), 3.83(ddABq, 2H, *J*=0.9Hz, 5.4 Hz, 5.7Hz, 16.2Hz, -CH_2), 4.82(d, 1H, *J*=5.7 Hz, H_5), 5.07(d, 1H, *J*=2.4 Hz, H_4), 6.06(s, 2H, $H_{6,7}$), 6.85-7.32(m, 13H, ArH, aromatic). δ_C ($CDCl_3$, 75 MHz), 49.3, 55.3, 57.2, 60.1, 69.7, 115.7, 116.6, 122.3, 123.8, 124.5, 125.9, 126.7, 129.1, 129.3, 133.5, 137.2, 138.0, 146.2, 155.4, 164.5. m/z 448 (M^+). ν_{max} (KBr)/cm^{-1} 1502, 1740, 3340, 3390cm^{-1}. Anal. Calc. for $C_{25}H_{25}ClN_2O_3$: C, 69.56; H, 5.61; N, 6.24; Found C, 69.72; H, 5.83; N, 6.05.

5i. 4-(4-chlorophenyl)-3-(1-hydroxy-4-(phenylamino)but-2-enyl)-1-*p*-tolylazetidin-2-one:

Pale Yellow solid, M. p.: 136-137°C, δ_H ($CDCl_3$, 300 MHz), 2.26(s, 3H, -CH_3), 3.44(dd, 1H, *J*= 2.4 Hz, 6.0 Hz, H_3), 3.82(ddABq, 2H, *J*=0.9Hz, 5.4 Hz, 5.7Hz, 16.2Hz, -CH_2), 5.03(d, 1H, *J*=5.7 Hz, H_5), 5.16(d, 1H, *J*=2.4 Hz, H_4), 5.81(m, 2H, $H_{6,7}$), 6.80-7.31(m, 13H, ArH, aromatic). δ_C ($CDCl_3$, 75 MHz), 22.3, 49.3, 57.7, 60.1, 69.8, 115.8, 116.5, 122.4, 123.8, 124.5, 125.8, 126.8, 128.1, 129.1, 129.3, 132.4, 137.2, 138.1, 146.1, 164.4. m/z 433 (M^+). ν_{max} (KBr)/cm^{-1} 1502, 1740, 3342, 3396cm^{-1}. Anal. Calc. for $C_{26}H_{25}ClN_2O_2$: C, 72.13; H, 5.82; N, 6.47; Found C, 72.29; H, 5.99; N, 6.32.

5j. 3-(1-hydroxy-4-(*m*-tolylamino)but-2-enyl)-1,4-diphenylazetidin-2-one:

Pale Yellow solid, M. p.: 123-124 °C, δ_H ($CDCl_3$, 300 MHz), 2.28(s, 3H, -

CH_3), 3.44(dd, 1H, *J*= 2.4 Hz, 5.7 Hz, H_5), 3.81(ddABq, 2H, *J*=0.9Hz, 5.4 Hz, 5.7Hz, 16.2Hz, -CH_2), 5.02(d, 1H, *J*=5.7 Hz, H_5), 5.15(d, 1H, *J*=2.4 Hz, H_4), 5.84(m, 2H, $H_{6,7}$), 6.84-7.31(m, 14H, ArH, aromatic). δ_C ($CDCl_3$, 75 MHz), 21.8, 49.2, 57.4, 60.1, 69.8, 112.9, 116.5, 117.2, 123.4, 123.9, 124.8, 126.0, 126.8, 128.3, 128.6, 129.0, 129.1, 137.6, 138.5, 142.9, 147.2, 164.2, m/z 398 (M^+). ν_{max} (KBr)/cm^{-1} 1505, 1745, 3345, 3395cm^{-1}. Anal. Calc. for $C_{26}H_{26}N_2O_2$: C, 78.36; H, 6.58; N, 7.03; Found C, 78.58, H, 6.77; N, 6.92.

5k. 1-(4-chlorophenyl)-3-(1-hydroxy-4-(*m*-tolylamino)but-2-enyl)-4-phenylazetidin-2-one:

Pale Yellow solid, M. p.: 131-132 °C, δ_H ($CDCl_3$, 300 MHz), 2.27(s, 3H, -CH_3), 3.43(dd, 1H, *J*= 2.4 Hz, 5.7 Hz, H_3), 3.83(ddABq, 2H, *J*=0.9Hz, 5.4 Hz, 5.7Hz, 16.2Hz, -CH_2), 5.05(d, 1H, *J*=5.7 Hz, H_5), 5.14(d, 1H, *J*=2.4 Hz, H_4), 5.88(m, 2H, $H_{6,7}$), 6.80-7.28(m, 13H, ArH, aromatic). δ_C ($CDCl_3$, 75 MHz), 21.8, 49.2, 57.4, 60.1, 69.8, 112.9, 116.4, 117.4, 123.1, 123.9, 124.5, 126.3, 126.8, 128.6, 129.0, 129.1, 133.3, 137.6, 138.3, 142.5, 147.2, 164.5, m/z 432 (M^+). ν_{max} (KBr)/cm^{-1} 1502, 1740, 3343, 3388cm^{-1}. Anal. Calc. for $C_{26}H_{25}ClN_2O_2$: C, 72.13; H, 5.82; N, 6.47; Found C, 72.29; H, 5.98; N, 6.29.

5l. 3-(1-hydroxy-4-(*m*-tolylamino)but-2-enyl)-4-phenyl-1-*p*-tolylazetidin-2-one:

Pale Yellow solid, M. p.: 128-129 °C, δ_H ($CDCl_3$, 300 MHz), 2.26(s, 3H, -CH_3, *p*-tolylPh), 2.28(s, 3H, -CH_3, *m*-tolyl), 3.44(dd, 1H, *J*= 2.4 Hz, 6.0 Hz, H_3), 3.82(ddABq, 2H, *J*=0.9Hz, 5.4 Hz, 5.7Hz, 16.2Hz, -CH_2), 5.04(d, 1H, *J*=5.7 Hz, H_5), 5.17(d, 1H, *J*=2.4 Hz, H_4), 5.88(m, 2H, $H_{6,7}$), 6.85-7.32(m, 13H, ArH, aromatic). δ_C ($CDCl_3$, 75 MHz), 21.8, 30.5, 49.2, 57.4, 60.2, 69.9, 112.6, 116.3, 117.2, 123.5, 123.9, 124.7, 126.1, 126.9, 128.2, 128.6, 129.0, 134.5, 137.6, 138.5, 142.9, 147.5, 164.3, m/z 412 (M^+). ν_{max} (KBr)/cm^{-1} 1504, 1741, 3342, 3398cm^{-1}. Anal. Calc. for $C_{27}H_{28}N_2O_2$: C, 78.61; H, 6.84; N, 6.79; Found C, C, 78.81; H, 6.98; N, 6.57.

5m. 3-(1-hydroxy-4-(*m*-tolylamino)but-2-enyl)-1-(4-methoxyphenyl)-4-phenylazetidin-2-one:

Pale Yellow solid, M. p.: 122-123 °C, δ_H ($CDCl_3$, 300 MHz), 2.27(s, 3H, -

CH_3), 3.44(dd, 1H, *J*= 2.4 Hz, 5.7 Hz, H_3), 3.77(s, 3H, -OCH_3), 3.82(ddABq, 2H, *J*=0.9Hz, 5.4 Hz, 5.7Hz, 16.2Hz, -CH_2), 5.08(d, 1H, *J*=5.7 Hz, H_5), 5.17(d, 1H, *J*=2.4 Hz, H_4), 5.88(m, 2H, $H_{6,7}$), 6.82-7.30(m, 13H, ArH, aromatic). δ_C ($CDCl_3$, 75 MHz), 21.8, 49.2, 55.7, 57.4, 60.1, 69.8, 112.9, 116.6, 117.3, 123.6, 123.9, 124.8, 126.1, 126.8, 128.5, 128.6, 129.2, 137.9, 138.5, 142.8, 147.2, 156.7, 164.4, m/z 428 (M^+). ν_{max} (KBr)/cm^{-1} 1504, 1743, 3342, 3390cm^{-1}. Anal. Calc. for $C_{27}H_{28}N_2O_3$: C, 75.68; H, 6.59; N, 6.54; Found C, 75.89; H, 6.78; N, 6.36.

5n. 4-(4-chlorophenyl)-3-(1-hydroxy-4-(*m*-tolylamino)but-2-enyl)-1-phenylazetidin-2-one:

Pale Yellow solid, M. p.: 133-134 °C, δ_H ($CDCl_3$, 300 MHz), 2.28(s, 3H, -CH_3), 3.43(dd, 1H, *J*= 2.4 Hz, 5.7 Hz, H_3), 3.84(ddABq, 2H, *J*=0.9Hz, 5.4 Hz, 5.7Hz, 16.2Hz, -CH_2), 5.08(d, 1H, *J*=5.7 Hz, H_5), 5.15(d, 1H, *J*=2.4 Hz, H_4), 5.88(m, 2H, $H_{6,7}$), 6.78-7.30(m, 13H, ArH, aromatic). δ_C ($CDCl_3$, 75 MHz), 21.8, 49.2, 57.4, 60.1, 69.8, 112.9, 116.5, 117.2, 123.4, 123.9, 124.9, 126.3, 126.9, 128.3, 128.5, 129.2, 131.3, 137.6, 138.5, 142.8, 147.6, 164.5, m/z 432 (M^+). ν_{max} (KBr)/cm^{-1} 1500, 1744, 3342, 3396cm^{-1}. Anal. Calc. for $C_{26}H_{25}ClN_2O_2$: C, 72.13; H, 5.82; N, 6.47; Found C, 72.30; H, 5.99; N, 6.31.

5o. 3-(1-hydroxy-4-(*m*-tolylamino)but-2-enyl)-4-(4-methoxyphenyl)-1-phenylazetidin-2-one:

Pale Yellow solid, M. p.: 123-124 °C, δ_H ($CDCl_3$, 300 MHz), 2.28(s, 3H, -CH_3), 3.44(dd, 1H, *J*= 2.4 Hz, 5.7 Hz, H_3), 3.77(s, 3H, -OCH_3), 3.82(ddABq, 2H, *J*=0.9Hz, 5.4 Hz, 5.7Hz, 16.2Hz, -CH_2), 5.05(d, 1H, *J*=5.7 Hz, H_5), 5.16(d, 1H, *J*=2.4 Hz, H_4), 5.89(m, 2H, $H_{6,7}$), 6.82-7.31(m, 13H, ArH, aromatic). δ_C ($CDCl_3$, 75 MHz), 21.8, 49.2, 5.4, 57.4, 60.1, 69.8, 112.9, 116.5, 117.2, 123.4, 123.8, 124.9, 126.6, 128.2, 128.5, 129.1, 129.2, 137.4, 138.2, 142.9, 147.5, 155.5, 164.3, m/z 428 (M^+). ν_{max} (KBr)/cm^{-1} 1502, 1743, 3340, 3392cm^{-1}. Anal. Calc. for $C_{27}H_{28}N_2O_3$: C, 75.68; H, 6.59; N, 6.54; Found C, 75.88; H, 6.74; N, 6.38.

5p. 1,4-bis(4-chlorophenyl)-3-(1-hydroxy-4-(*m*-tolylamino)but-2-enyl)azetidin-2-one:

Pale Yellow solid, M. p.: 134-135 °C, δ_H ($CDCl_3$, 300 MHz), 2.26(s, 3H, -CH_3), 3.42(dd, 1H, *J*= 2.4 Hz, 5.7 Hz, H_3), 3.82(ddABq, 2H, *J*=0.9Hz, 5.4

Hz, 5.7Hz, 16.2Hz, -CH_2), 5.06(d, 1H, *J*=5.7Hz, H_5), 5.16(d, 1H, *J*=2.4 Hz, H_4), 5.89(m, 2H, $H_{6,7}$), 6.82-7.30(m, 12H, ArH, aromatic). δ_C ($CDCl_3$, 75 MHz), 21.5, 49.2, 57.4, 60.3, 69.7, 112.9, 116.5, 117.4, 123.1, 123.8, 124.6, 126.6, 128.1, 128.6, 129.0, 131.2, 133.5, 137.3, 138.4, 142.9, 147.3, 164.5, m/z 466 (M^+). ν_{max} (KBr)/cm^{-1} 1504, 1742, 3343, 3390cm^{-1}. Anal. Calc. for $C_{26}H_{24}Cl_2N_2O_2$: C, 66.81; H, 5.18; N, 5.99; Found C, 66.99; H, 5.36; N, 5.79.

5q. 1-(4-chlorophenyl)-3-(1-hydroxy-4-(*m*-tolylamino)but-2-enyl)-4-(4-methoxyphenyl)azetidin-2-one:

Pale Yellow solid, M. p.: 130-131 °C, δ_H ($CDCl_3$, 300 MHz), 2.28(s, 3H, -CH_3), 3.42(dd, 1H, *J*= 2.4 Hz, 6.0 Hz, H_3), 3.78(s, 3H, -OCH_3), 3.82(ddABq, 2H, *J*=0.9Hz, 5.4 Hz, 5.7Hz, 16.2Hz, -CH_2), 5.04(d, 1H, *J*=6.0 Hz, H_5), 5.15(d, 1H, *J*=2.4 Hz, H_4), 5.89(m, 2H, $H_{6,7}$), 6.82-7.30(m, 12H, ArH, aromatic). δ_C ($CDCl_3$, 75 MHz), 21.6, 49.1, 55.3, 57.4, 60.2, 69.6, 112.9, 116.4, 117.1, 123.3, 123.9, 124.7, 126.7, 128.1, 128.5, 129.0, 133.3, 137.4, 138.4, 142.8, 147.1, 155.4, 164.4, m/z 462 (M^+). ν_{max} (KBr)/cm^{-1} 1502, 1740, 3341, 3396 cm^{-1}. Anal. Calc. for $C_{27}H_{27}ClN_2O_3$: C, 70.05; H, 5.88; N, 6.05; Found C, 70.24; H, 5.99; N, 5.88.

5r. 4-(4-chlorophenyl)-3-(1-hydroxy-4-(*m*-tolylamino)but-2-enyl)-1-*p*-tolylazetidin-2-one:

Pale Yellow solid, M. p.: 128-129 °C, δ_H ($CDCl_3$, 300 MHz), 2.26(s,3H, -CH_3, *p*-tolylPh), 2.28(s, 3H, -CH_3, *m*-tolyl), 3.43(dd, 1H, *J*= 2.4 Hz, 5.7 Hz, H_3), 3.84(ddABq, 2H, *J*=0.9Hz, 5.4 Hz, 5.7Hz, 16.2Hz, -CH_2), 5.08(d, 1H, *J*=5.7 Hz, H_5), 5.17(d, 1H, *J*=2.4 Hz, H_4), 5.88(m, 2H, $H_{6,7}$), 6.82-7.30(m, 12H, ArH, aromatic). δ_C ($CDCl_3$, 75 MHz), 21.7, 30.5, 49.1, 57.3, 60.2, 69.9, 112.9, 116.4, 117.0, 123.5, 123.9, 124.9, 126.8, 128.4, 128.7, 129.2, 131.4, 135.7, 137.7, 138.8, 142.8, 147.5, 164.4. m/z 446 (M^+). ν_{max} (KBr)/cm^{-1} 1503, 1742, 3342, 3390cm^{-1}. Anal. Calc. for $C_{27}H_{27}ClN_2O_2$: C, 72.55; H, 6.09; N, 6.27; Found C, 72.74; H, 6.25; N, 6.12.

IV. Acknowledgments

The authors are thankful to Khalsa College Amritsar for providing the necessary research facilities. The help of Guru Nanak Dev University for the spectroscopic analysis is also highly acknowledged.

V. References

[1] R. Noyori, Asymmetric Catalysis in Organic Synthesis, New York : John Wiley & Sons (1994).

[2] (a) G. M. Coppola and H. F. Schuster, Asymmetric Synthesis. Construction of Chiral Molecules Using Amino Acids, New York: Wiley (1987). (b) S. C. Bergmeier, Tetrahedron (2000). 56, 2561.

[3] (a) M. Studer,, H. U. Blaser, C. Exner, Adv. Synth. Catal (2003). 45, 345 (b) A. A.Smaardijk, H. Wynberg, J. Org. Chem. (1987). 52, 135 (c) H. Wynberg, Asymmetric Catalysis by Cinchona Alkaloids. In Topics in Stereochemistry; E. L. Eliel, S. Wilen, Wiley-Interscience: New York (1986). 16 (d) G. Muchow, Y. Vannoorenberghe, G. Buono, Tetrahedron Lett. (1987), 28, 6163 (e) P. A. Chaloner, Tetrahedron Lett. (1987). 28, 3013 (f) E. J. Corey, F. J. Hannon, Tetrahedron Lett. (1987). 28, 5237 (g) K. Soai, S. Yokoyama, K. Ebihara T. Hayasaka, J. Chem. Soc., Chem. Commun.(1987). 1690 (h) K. Soai, S. Yokoyama, T. Hayasaka, J. Org. Chem. (1991). 56, 4264.

[4] A. Lei, S. Wu, M. He, X. Zhang, J. Am. Chem. Soc. (2004). 126, 1626.

[5] W. Y. Zhong, Z. Y. Dong, K. Fang, K. Izumi, M. H. Xu, Q. G. Lin, J. Am. Chem. Soc. (2005). 127, 11956.

[6] T. P Loh, J. M. Huang, S. H. Goh, J. J. Vittal, Organic Letters (2000). 2, 1291.

[7] G. Kedi, A. P. Truong, Organic Letters (2002). 4, 3131.

[8] (a) N. J. Leonard, A. J. Playtis, F. Skoog, R. Y. Schmitz, J. Am. Chem. Soc. (1971). 93, 3056. (b) J. Streith, A. Defoin, Synthesis (1994). 1107.

[9] (a) P. F. Vogt, M. J. Miller, *Tetrahedron* (1998). **54**, 1317; (b) J. Streith, A. Defoin, *Synlett* (1996). 189.

[10] M. Wu, T. P. Begley, Org. Lett. (2000). 2, 1345.

[11] A. Al-Harrasi, H. U. Reissig, Synlett, (2005). 1152.

[12] (a) B. H. Lee, A. Biswas, M. J. Miller, J. Org. Chem. (1986). 51, 106. (b) O. Labeeuw, P. Phansavath, J. P. Genet, Tetrahedron Lett. (2004).45, 7107 (c) M. C. Desai, J. L. Doty, L. M. Stephens, K. E. Brighty, Tetrahedron Lett. (1993). 34, 961.

[13] G. E.Keck, S. Fleming, D. Nickell, D. Weider, Synth. Commun. (1979), 281.

[14] E. G. Baggiolini, H. L. Lee, G. Pizzolato, M. R. Uskokovic, J. Am.Chem. Soc., (1982). 104, 6460.

[15] (a) W. Oppolzer, M. J. Petrzilka, J. Am. Chem. Soc., (1976). 98, 6722 For the use of the NiCl2-LiAlH4 reductive system, see:(b) J. J. Tuffariello, H. Meckler, K. Pushpananda, A. Seranatne, Tetrahedron (1985). 41, 3447.

[16] (a) S. Cicchi, A. Goti, A. Brandi, A. Guarna, F. De Sarlo, Tetrahedron Lett. (1990). 31, 3351; For the NaBH4 modification, see: (b) D. Zhang, C. S. Ulling, M. J. Miller, *J. Org. Chem.* (1998). **63**, 885.

[17] G. E. Keck, S. F. McHardy, T. T. Wager, Tetrahedron Lett. (1995). 36, 7419.

[18] S. Cicchi, M. Bonani, F. Cardona, J. Revuelta, A. Goti, Org. Lett. (2003). 5, 1773.

[19] Pd/C: P. M. Wovkulich, M. R. Uskokovic, J. Am. Chem. Soc. (1981). 103, 3956; Pd(OH)2: P. DeShong, J. M. Leginus,, J. Am. Chem. Soc. (1983). 105, 1686; PtO2: N. A. Lebel, N. D. Ojha, J. R. Menke, R. J. Newland, J. Org. Chem. (1972). 37, 2896; Raney Ni: T. Koizumi, H. Hirai, E. Yoshii, J. Org. Chem. (1982). 47, 4004.

[20] M. P. Van Boggelen, B. F. G. A. Van Dommelen, S. Jiang, G. Singh, Tetrahedron (1997). 53, 16897 (b) T. S. Cooper, P. Laurent, C. J. Moody, A. K. Takle, Org. Biomol. Chem. (2004). 265 (c) B. J. McAuley, M. Nieuwenhuyzen, G. N. Sheldrake, Org. Lett. (2000). 2, 1457 (d) G. N. Sheldrake, N. Soissons, J. Org. Chem. (2006). 71, 789.

[21] Lise Keinicke Peter Fristrup Per-Ola Norrby Robert Madsen, J. Am. Chem. Soc. (2005). 127, 45, 15756.

[22] D. J. A*dam, J. Calow*, *Andrei S. Batsanov*, *Alba Pujol*, *Cristina Solé*, *Elena Fernández*, and *Andrew Whiting, Org.* Lett., (2013). 15, 18, 4810.

[23] B. P. Machin, M. Ballantine, J. Mandel,N. Blanchard, W. J. Tam, Org. Chem. (2009). 7261.

[24] B. P Machin, J. Howell, J. Mandel, N. Blanchard, W. Tam, Org. Lett. (2009). 10, 2077.

[25] B. Yang, M. J. Miller, J. Org. Chem. (2009). 7990.

[26] C. Kouklovsky, N. Blanchard, G. Calvet, G. Galvani, Org. Biomol. Chem. (2008). 6, 1063.

[27] (a) B. Alcaide, P. Almendros, N. R. Salgado, J. Org. Chem. (2000). 65, 3310 (b) B. Alcaide, P. Almendros, Tetrahedron Lett. (1999). 40, 1015 (c) B. Alcaide, P. Almendros, C. Aragoncillo, N. R. Salgado, J. Org. Chem6. (1999). 64, 9596 (d) B. Alcaide, M. F. Aly, C. Rodrı´guez, A. Rodrı´guez-Vicente, J. Org. Chem. (2000). 65, 3453 (e) B. Alcaide, P. Almendros, C. Aragoncillo, Chem. Commun. (2000). 757 (f) B. Alcaide, P. Almendros, C. Aragoncillo, Org. Lett. (2000). 2, 1411; (g) B. Alcaide, E. Sa´ez, Tetrahedron Lett. (2000). 41, 1647 (h) B. Alcaide, P. Almendros, J. M. Alonso, M. F. Aly, Chem. Commun. (2000). 485.

[28] A. K. Sharma, S. N. Mazumdar, M. P. Mahajan, J. Org. Chem. (1996). 61, 5506.

[29] A. K. Sharma, S. Jayakumar, M. S. Hundal, M. P. Mahajan, *J. Chem. Soc. Perkin Trans 1* (2002). 774.

[30] A. K. Sharma, R. S. Kumar, M. P. Mahajan, *Heterocycles* (2000). 52, 803.

[31] G. Bhargava, M. P. Mahajan, T. Saito, T. Otani, M. Kurashima, K. Sakai, *Eur. J. Org. Chem.* (2005). 2397.

[32] G.. Bhargava, M. P. Mahajan, T. Saito, *Synlett* (2008). 983.

[33] Amit Anand, Vipan Kumar, Parvesh Singh, Krishna Bisetty, Mohinder P. Mahajan, *Letters in Org. Chem.* (2012). 9, 411.

Curr. Rep. Sci. & Tech. 2 (1) (2016) 73-94

Catalysed Acetylation of Alcohols, Phenols and Amines: A review

M.S. Batra and Hardeep Kaur
Post Graduate College of Chemistry, Khalsa College Amritsar, Punjab-143005.
hardeepbhatia@ymail.com

Abstract

Acetylation of alcohols, phenols and amines is one of the most common acetylation reactions, carried out with acetic anhydride, acetyl chloride and acetic acid using a wide range of novel catalysts and reaction conditions. The reaction is frequently employed for the protection of OH and NH_2 groups during the course of various transformations in a synthetic sequence, especially in the construction of polyfunctional molecules. During the last decade, a number of selective and easily recyclable catalysts which work under the environmentally benign reaction conditions have been reported for the acetylation of these functional groups. Here we have reviewed the recent developments in the area of acetylation of alcohols, phenols and amines with specific emphasis towards nature of catalyst, reaction conditions and usefulness.

Keywords

Acetylation, Alcohols, Thiols, Phenols, Amines

I. Introduction

The acetylation of alcohols, phenols, and amines is one of the most important and frequently used employed reactions in organic synthesis [1-2]. The reaction involves substitution of one or more active hydrogen atoms of these functional groups by an acetyl group and is normally carried out by employing acetic anhydride or acetyl chloride in the presence of a suitable catalyst [3-8]. Acetylation of alcohol/phenol and amine results in the formation of an ester and an amide respectively, which are of great synthetic and commercial importance.

$ROH + CH_3COCl \rightarrow ROCOCH_3 + HCl$ (R=alkyl or aryl group)
$ROH + (CH_3CO)_2O \rightarrow ROCOCH_3 + HCl$ (R=alkyl or aryl group)
$RNH_2 + CH_3COCl \rightarrow RNHCOCH_3 + HCl$ (R=alkyl or aryl group)

Scheme 1. General acetylation reaction.

Another usefulness of this reaction is that it provides a method for the protection of OH and NH groups. The protection of hydroxyl and amino groups is often required during the course of various transformations in a synthetic sequence, especially in the construction of polyfunctional molecules such as nucleosides, carbohydrates, steroids, and natural products.

Acetylation is usually carried out by treating alcohols/phenols or amines with acetic anhydride or acetyl chloride in the presence of an acid, base or a suitable catalyst, in a solvent or solvent free conditions. A variety of methods have been reported in the literature for the acetylation of alcohols and phenols. Herein this review, we have complied the catalyst mediated acetylation of alcohols/phenols and amines using metal salts, metal carbonates, metal oxides, metal triflates, metal tosylates, metal complexes, metals, supported acids, bases and iodine.

I. Acetylation of Alcohols, Phenols and Amines

A. Using Metal salts

Cobalt (II) chloride is used as a catalyst for the acetylation of a variety of alcohols and phenols such as primary, secondary and tertiary with acetic anhydride or acetyl chloride at ambient reaction conditions. The reagent allows selective acetylation of primary hydroxyl groups, in the presence of secondary and tertiary ones while the secondary hydroxyl groups can be preferentially acetylated in the presence of tertiary ones (Scheme 2).The catalyst can be recycled several times without loss of catalytic activity [9-10].

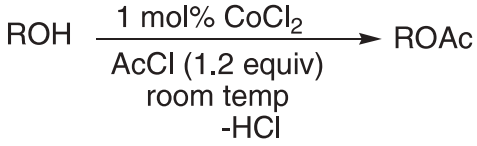

Scheme 2. *Acetylation of alcohols using Co_2Cl_2.*

The acetylation of various alcohols and phenols has also been successfully performed in high yield using an immobilized cobalt (II)

catalyst [11] (Scheme 3). The primary and secondary alcohols were acetylated easily in the presence of the supported cobalt (II) catalyst with acetic anhydride whereas tertiary alcohols required longer reaction times for completion of the reaction. Moreover, the catalyst efficiently acetylated both electron-rich and electron-deficient phenols to corresponding acetates in excellent yields. Further, the catalyst showed high thermal stability and was also recovered and reused at least 10 times without any considerable loss of activity.

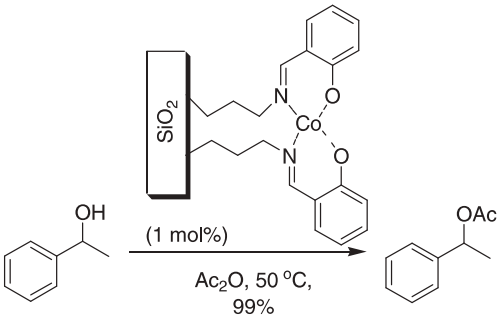

Scheme 3. Acetylation of alcohols/phenols using an immobilized cobalt (II) chloride.

Cerium (III) chloride in used as a catalyst for chemoselective acylation of plenatic alcohols with acyl chloride in THF. In the reported method [12], the alcoholic group undergoes acylation the presance of a phenolic group (Scheme-4).

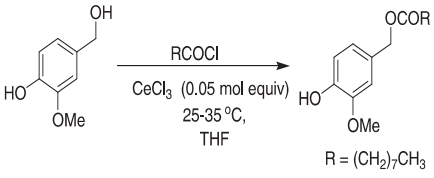

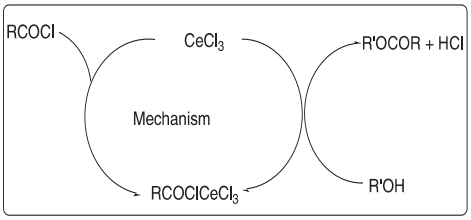

Scheme 4. *Acetylation of phenols using cerium (III) chloride.*

Anhydrous nickel chloride is also used as a catalyst for acetylation of a variety of alcohols/phenols and amines. Meshram *et al* [13] reported the acetylation of alcohols, phenols, amines, and thiols with acetic anhydride (Ac_2O) under solvent free conditions in the presence of 0.1 mol% (13 mg) anhydrous $NiCl_2$ catalyst (Scheme 5).

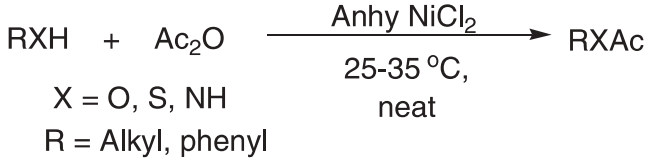

Scheme 5. *Acetylation of phenols using $NiCl_2$ catalyst.*

Chandrashekhar *et al* reported acetylation of a wide range of alcohols such as primary, secondary, allylic and benzylic using $TaCl_5$-SiO_2 as a catalyst [14] (Scheme 6). Further, this method is employed in the kinetic resolution of secondary alcohols using $TaC1_5$ in combination with some chiral ligands [(-)2,3-O-iso propylidene-l,l,4,4-tetra phenyl-L-threitol and α,α-Diphenyl-D- prolinol] as catalyst. But unfortunately low ee's were obtained.

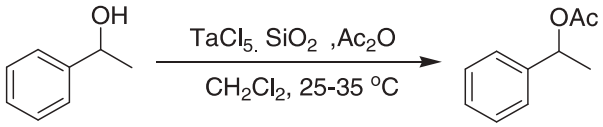

Scheme 6. *Acetylation of alcohols using $TaCl_5$-SiO_2 as a catalyst.*

Zirconium(IV) chloride has been used as a highly efficient, and reusable catalyst for acetylation of structurally diverse phenols, thiols, amines, and alcohols under solvent-free conditions [15]. Acetylation of sterically hindered and electron deficient phenols has been reported in excellent yields with stoichiometric amounts of Ac_2O at room temperature (Scheme 7).

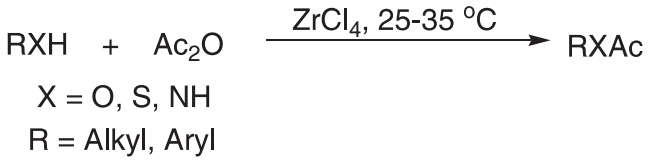

Scheme 7. *Acetylation of alcohols/phenols using $ZrCl_4$ as a catalyst*

Montmorillonite K-10 clay supported $InCl_3$ [16] has been reported as a highly active catalyst for the acetylation of aromatic alcohols and phenols with different acyl chlorides. This catalyst can be reused in reactions number of times without any significant loss of catalytic activity (Scheme 8).

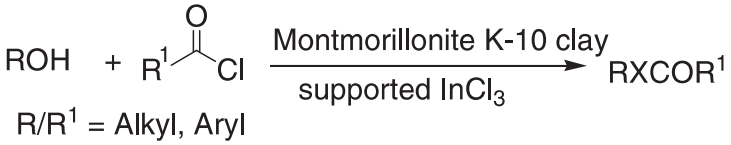

Scheme 8. *Acetylation of phenols and alcohols with acyl chlorides using Montmorillonite K-10 clay supported Indium (III) chloride ($InCl_3$)*

Niobium (V) chloride [17] is used as novel catalyst for selective acetylation of a wide range of alcohol functional groups such as primary, secondary, tertiary, benzylic and phenolic (Scheme 9). Acetylation of various alcohols, has been carried out successfully, while using acetic anhydride and catalytic amount of niobium (V) chloride at room temperature.

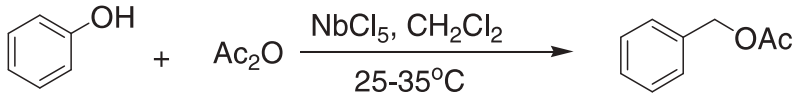

Scheme 9. *Acetylation of alcohols/phenols using Niobium (V) chloride.*

Reddy *et al* [18] used catalytic amounts of $La(NO_3)_3$ and acetic anhydride for acetylation of a wide variety of alcohols, phenols and amines into the corresponding acetates under solvent-free conditions at room temperature. The method is compatible with acid sensitive hydroxyl protecting groups such as TBDMS, THP, OBz, OBn, Boc and some isopropylidenes and offers excellent yields of the mono acetates of 1,3-, 1,4- and 1,5-diols (Scheme 10).

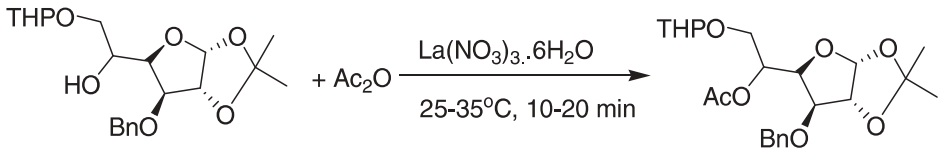

Scheme 10. *Acetylation of alcohols using $La(NO_3)_3$*

A comparative study of acetylation of alcohols and phenols with different acetylating agents and Zinc Cheoride Catalyst [19] under solvent free conditions has been investigated (Scheme 13).

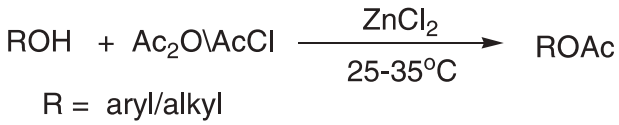

Scheme 11. *Acetylation of alcohols using Zinc Cheoride.*

B. Using Metal carbonates

Metal carbonates and bicarbonates have been used as mild bases for the acetylation of alcohols and phenols. Lugemwa *et al* [20] reported acetylation of a variety of primary alcohols and phenols with acetic anhydride at room temperature in the presence of sodium bicarbonate to produce corresponding esters in good to excellent yields (Scheme 12). The acetylation of 4-nitrobenzyl alcohol has been reported with a number of other carbonates. It has been found that the reaction in the presence of cesium bicarbonate and lithium carbonate gave 4-nitrobenzyl acetate in excellent yield, while in the presence of Na_2CO_3, K_2CO_3, Cs_2CO_3, or

$KHCO_3$ the yield was in the range of 80% to 95%. Amongst the solvent used ethyl acetate, THF, toluene, diethyl ether, dichloromethane, and acetonitrile; toluene was found to be the best solvent for the reaction, while diethyl ether was the poorest.

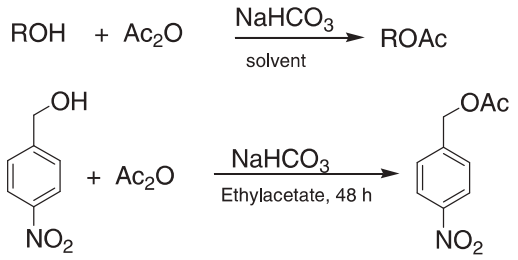

Scheme 12. *Acetylation of phenols/alcohols using carbonates.*

Acetylation of amines in the form of amine hydrochlorides with anhydrides has been reported in an aqueous medium on addition of $NaHCO_3$. The protonated ammonium species is non- nucleophilic due to non-availability of lone pair of electrons on the nitrogen atom and as such does not participate in acetylation reaction. However, upon addition of basic salts, such as $NaHCO_3$, free amines are liberated, which reacts with acetic anhydride to give acylated products. Using this methodology, chemoselective acetylation of amines in the presence of phenols and thiols has been achieved with high selectivity [21].

Potassium carbonate has also been found to be an efficient catalyst for the synthesis of esters and thioesters from alcohols and thiols. Kazemi *et al* [22] reported acetylation of alcohols, phenols and thiols with acetic anhydride using tetra *n*-butylammonium iodide (TBAI) as a phase-transfer catalyst and in the presence of potassium carbonate (K_2CO_3) (Scheme 13). This is a mild, general and practical procedure for the synthesis of esters and thioesters in high yields and suitable reaction times.

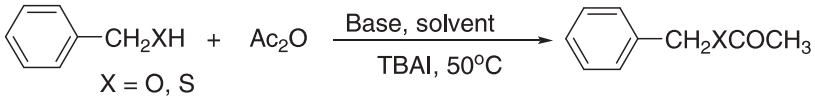

Scheme 13. *Acetylation of alcohols/thiols using potassium carbonate.*

N-Acetylation of anilines with acetyl chloride in the presence of a base like K_2CO_3 and phase transfer catalysts like TBAB, TEBAC and D-Glucose in different solvents like DMF, DMSO, acetonitrile, ethyl acetate,

chloroform etc at room temp have been reported (Scheme 14). Phase Transfer Catalyzed (TBAB) N-acetylation of anilines with acetyl chloride in DMF as solvent and K_2CO_3 as base is considered to be efficient and convenient synthetic methodology [23].

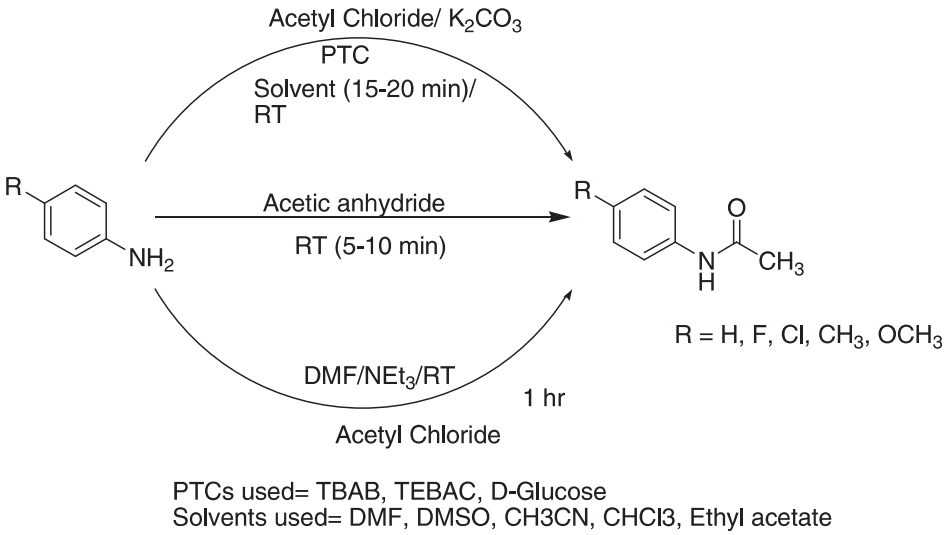

Scheme 14. *Acetylation of amines using PTC.*

C. Metal oxides

A variety of transition metal oxides have been used as catalysts for acetylation of alcohols/phenols and amines. These metal oxides act as heterogenous catalysts, which give ease of separation and the reactions can be carried out under without solvent conditions. Zinc oxide (ZnO) has been used as a catalyst for the acetylation of a variety of alcohols, phenols and amines with acid chlorides or acetic anhydrides under solvent free conditions [24]. Primary, secondary, tertiary, allylic and benzylic alcohols, diols and phenols with electron donating or withdrawing subtituents can be easily acylated in good to excellent yield (Scheme 15).

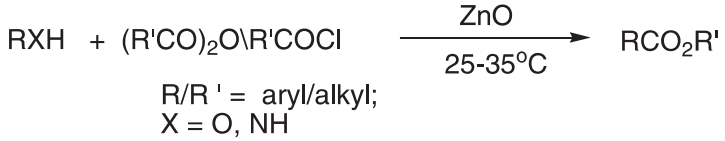

Scheme 15. *Acetylation of alcohols using ZnO.*

Tamaddon *et al* also reported acetylation of alcohols and phenols with acyl chloride using ZnO as a catalyst under solvent free conditions [25] (Scheme 16).

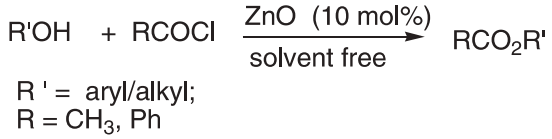

Scheme 16. *Acetylation of alcohols using ZnO.*

Rajabi *et al* [26] reported acetylation of alcohols and phenols with iron oxide nanoparticles supported on silicate material (SBS-15) under mild and solvent free conditions (Scheme 17). The catalyst can be easily recovered from the reaction mixture and can be reused ten times without loss of activity.

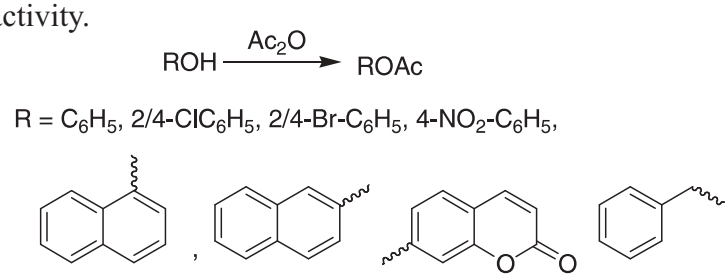

Scheme 17. *Acetylation of alcohols using iron oxide nanoparticles*

Zarei *et al* [27] reported a convenient, rapid, and efficient method for the acetylation of alcohols, phenols, thiols, and amines using acetic anhydride in the presence of a catalytic amount of P_2O_5/Al_2O_3 under solvent-free conditions at room temperature (Scheme 18).

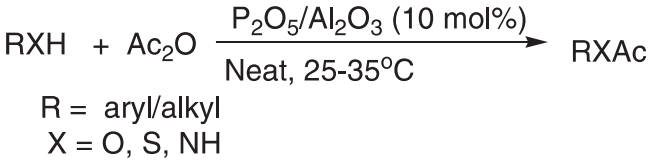

Scheme 18. *Acetylation of alcohols using P_2O_5/Al_2O_3*

D. Using Metal triflates and tosylates

Metal triflates have been used as a Lewis acid catalyst in many synthetic organic transformations. Otera *et al* [28] reported acetylation of alcohols using $Bi(OTf)_3$ as a catalyst (Scheme 19). In this protocol hindered and functionalized alcohols are acylated at 25°C, and solvents can be employed without purification.

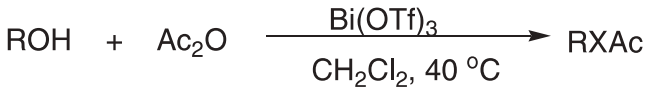

R = primary, secondary, tertiary alkyl, aryl.

Scheme 19*. Acetylation of alcohols using Bi(OTf)$_3$ as a catalyst*

Highly efficient acetylation and benzoylation of alcohols, phenols, amines and thiols have been reported with acetic and benzoic anhydrides catalyzed by new and reusable zirconyl triflate, $ZrO(OTf)_2$ (Scheme 20). The electron deficient $ZrO(OTf)_2$ [29] can be used for the acetylation and benzoylation of not only primary alcohols but also sterically-hindered secondary and tertiary alcohols with acetic and benzoic anhydrides. This catalyst can be reused several times without loss of its activity.

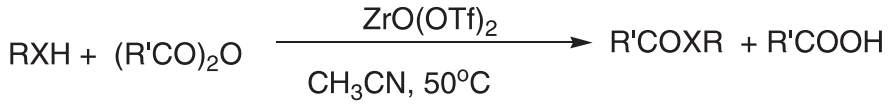

R = Alkyl, Aryl; X = NH, O, S; R' = CH_3, Ph

Scheme 20*. Acetylation of alcohols, phenols, amines and thiols using zirconyl triflate.*

Cerium (III) triflate has been used as a catalyst for the acetylation of a large variety of simple and functionalized alcohols with acetic anhydride [30] (Scheme 21).

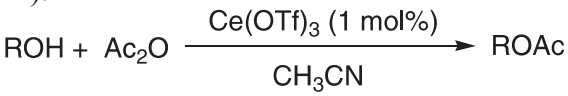

R = Alkyl, Aryl

Scheme 21. *Acetylation of alcohols using Cerium(III) triflate.*

Ahmed *et al* [31] reported the use of aluminium triflate (0.01 to 0.1 mol %) as an efficient catalyst for the acetylation of alcohols, phenols, thiols and sugars with acetic anhydride under solvent-free conditions at room temperature (Scheme 22).

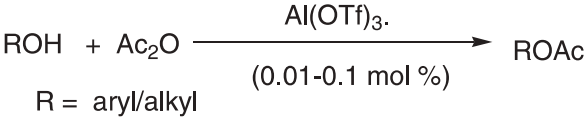

Scheme 22. *Acetylation of alcohols using aluminium triflate.*

Polymer-supported gadolinium triflate (CMPS-IM-Gd) catalyst [32] has been successfully used as an efficient lewis acid catalyst for the acetylation of various alcohols and phenols with acetic anhydride, affording high yields under mild conditions. The reaction was completed in

a short period of time with small amounts of the catalyst. The catalyst was prepared from chloromethyl polystyrene (CMPS) resin using a simple and convenient procedure and was reused over 10 times without any significant loss of its catalytic activity (Scheme 23).

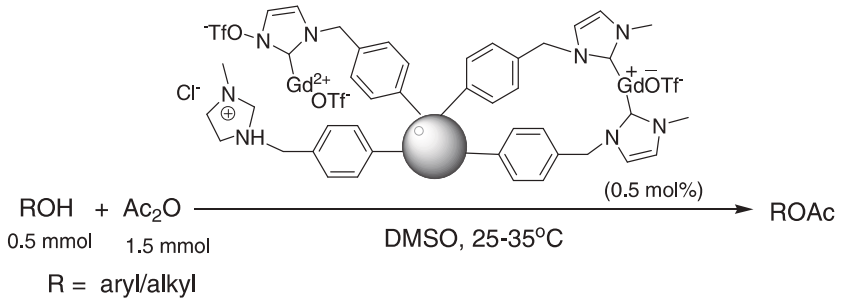

Scheme 23. *Acetylation of alcohols using gadolinium triflate*

Taghavi *et al* [33] explored the catalytic activity of high-valent tetraphenylporphyrinato-vanadium (IV) trifluoromethanesulfonate, $[V^{IV}(TPP)\ (OTf)_2]$, in the acetylation of alcohols and phenols with Ac_2O. The method was employed for both aliphatic and benzylic alcohols as well as sterically-hindered secondary and tertiary alcohols. Acetylation of phenols with acetic anhydride afforded the desired acetates in 88-99% yield (Scheme 24).

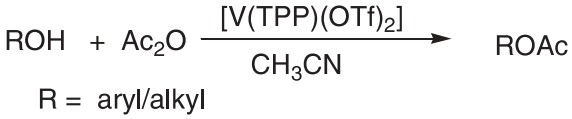

Scheme 24. *Acetylation of alcohols using vanadium salt catalyst.*

Silver triflate [34] has also been used as catalyst in acetylation of a variety of alcohols, thiols, phenols, and amines. The method described has a wide range of applications, proceeds under mild conditions, does not involve cumbersome workup, and the resulting products were obtained in high yields within a reasonable time (Scheme 25).

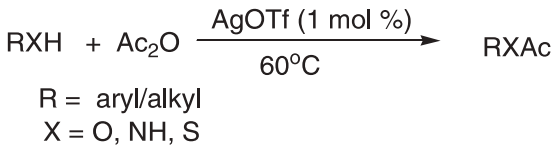

Scheme 25. *Acetylation of alcohols/amines/thiols using silver triflate.*

Baldwin *et al* used iron (III) *p*-toluenesulfonate (tosylate) as an efficient catalyst [35] for acetylation of alcohols, phenols, and aldehydes. The acetylation of primary and secondary alcohols, diols, and phenols proceeded smoothly with 2.0 mol % of catalyst. However, the reaction worked well with only a few tertiary alcohols. Iron (III) tosylate is an inexpensive, and easy to handle, commercially available catalyst (Scheme 26).

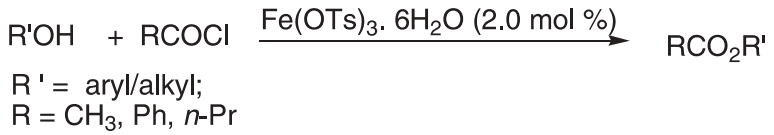

Scheme 26. *Acetylation of alcohols using iron(III) p-toluenesulfonate.*

E. Using Metal complexes

A number of metal complexes has been used as catalysts for acetylation of alcohols, phenols and amines. Chemo-selective acetylation of amines, phenols and alcohols with acetyl chloride in the presence of catalytic amount of metal acetylacetonates [36] covalently anchored onto amine functionalized silica under solvent-free conditions has been reported (Scheme 27).

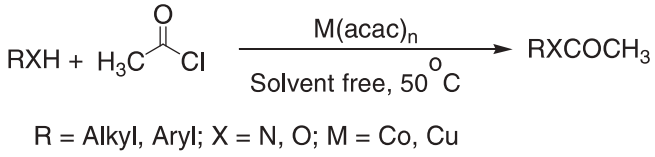

Scheme 27. *Acetylation of alcohols/phenols/amines using metal acetylacetonates.*

Moghadam *et al* [37] used tin (IV) tetraphenylporphyrinatotetrafluoroborate, SnIV(tpp)$(BF_4)_2$ as a catalyst for efficient acetylation of alcohols and phenols with acetic anhydride (Scheme 28). The method has been successfully employed for acetylation of not only primary alcohols and phenols but also sterically hindered secondary and tertiary alcohols with acetic anhydride. This catalyst selectively acetylated the alcohols and phenols in the presence of acetals and silyl ethers.

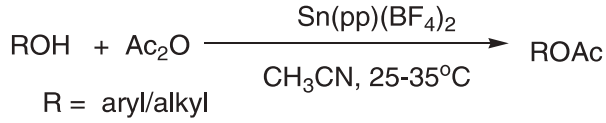

Scheme 28. *Acetylation of alcohols using tin(IV) tetraphenylporphyrinatotetrafluoroborate*

N-Acyl 1,5-diazabicyclo[4.3.0]non-5-ene tetraphenylborate salt [38] has been used as O-acylating agents for conversion of primary and secondary alcohols to corresponding esters. When both primary and secondary alcoholic groups are present in the same molecule, primary alcoholic group is acylated regioselectively (Scheme 29).

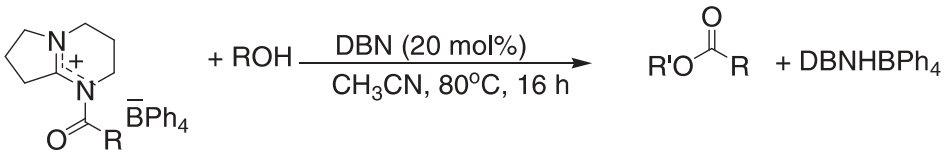

Scheme 29. *Acetylation of alcohols using N-Acyl 1,5-diazabicyclo[4.3.0]non-5-ene*

F. Using Metal

Acetylation of phenols, thiophenol, amines and alcohols with acyl chlorides in a solvent free system at 25°C have been reported using zinc dust as a catalyst [39]. The catalyst can be recovered and recycled making the procedure potentially useful for industrial applications (Scheme 30).

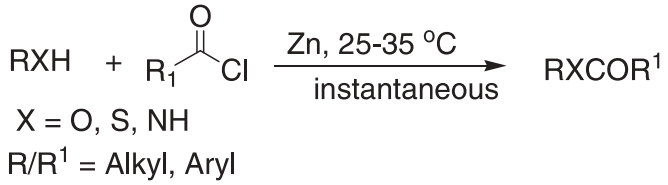

Scheme 30*. Acetylation of phenols, thiophenol, amines and alcohols with acyl chlorides and Zn dust.*

G. Using supported acids

Application of solid acids in organic transformations is important because solid acids have many advantages such as simplicity in handling, decreased reactor and plant corrosion problems, and more environmentally safe disposal. Akhlaghinia *et al* reported use of polyvinyl alcohol immobilized N-ethyl sulfamic acid (PVA-$NHSO_3H$) catalyst [40] for acetylation of a variety of phenols, alcohols, amines and thiols with acetic anhydrides at ambient temperature under solvent free conditions. The catalyst works well for a large variety of simple and functionalized phenols, alcohols, amines and thiols (Scheme 31).

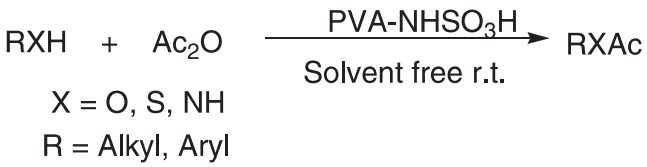

Scheme 31. *Acetylation of a variety of phenols, alcohols, amines and thiols with acetic anhydride using PVA-$NHSO_3H$.*

Solid supported silica sulfuric acid (SSA) [41] has been employed as a heterogeneous catalyst for the acetylation of a variety of phenols, amines, and thiols under solvent-free conditions at room temperature (Scheme 32). Deactivated substrates also acetylated rapidly, and the method showed the preferential selectivity for acetylation of amino group in the presence of hydroxyl group in which no C-acetylation was observed.

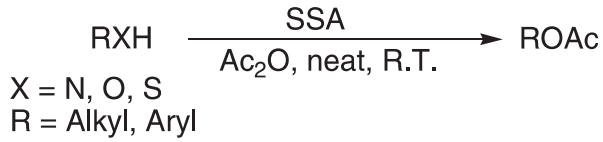

Scheme 32. *Acetylation of a variety of phenols, amines, and thiols using Silica sulfuric acid*

Zeolites (ZSM-5) catalyses acetylation of sulfonamides, amines, alcohols, and phenols with carboxylic acid anhydrides and chlorides using under mild and solvent-free conditions [42]. In this method, different types of amides and esters were obtained in moderate to high yields and purity after a simple workup, requiring no chromatographic separation (Scheme 33).

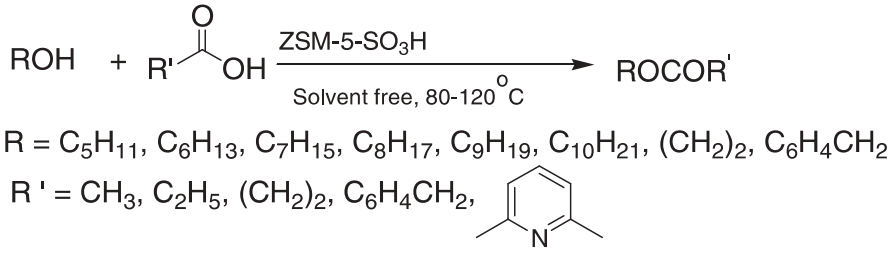

Scheme 33. *Acetylation of alcohols/phenols using ZSM-5-SO_3H.*

Melamine trisulfonic acid (MTSA) [43] is another efficient catalyst for acetylation of alcohols, phenols, and amines with Ac_2O under mild and completely heterogeneous reaction conditions (Scheme 34).

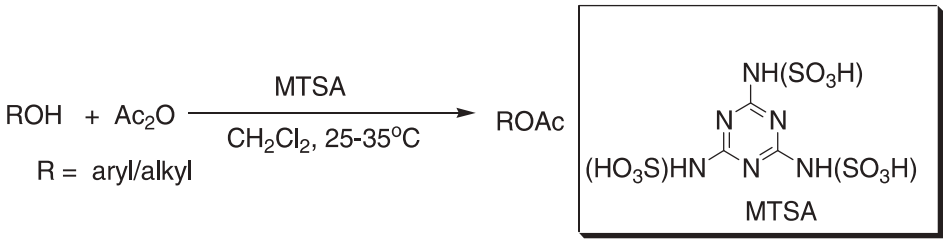

Scheme 34. *Acetylation of alcohols using Melamine trisulfonic acid.*

Chakraborti *et al* [44] reported fluoroboric acid supported on silica gel catalyzed acetylation of structurally diverse phenols, alcohols, thiols, and amines under solvent free conditions (Scheme 35). Acid-sensitive alcohols are smoothly acylated without competitive side reactions.

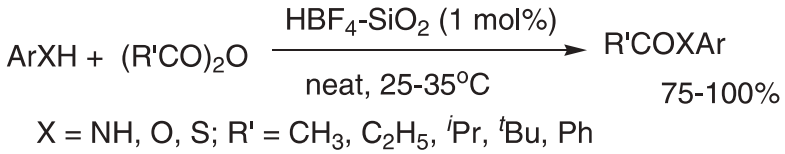

Scheme 35. *Acetylation of alcohols/phenols/amines/thiols using fluoroboric acid.*

3-Nitrobenzeneboronic acid has been employed as catalyst for acetylation of a wide range of alcohols as well as phenols with acetic anhydride in good to excellent yields at room temperature under solvent-free conditions [45]. The reactions are clean and the catalyst is mild such that highly sensitive functional groups including oximes are stable to the reaction conditions (Scheme 36).

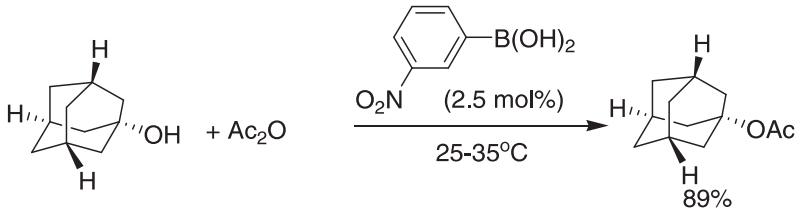

Scheme 36. *Acetylation of alcohols using 3-nitrobenzeneboronic acid.*

Methylenediphosphonic acid (MDP) [46] has also been employed as a heterogeneous catalyst for the acetylation of structurally diverse alcohols, phenols and amines with acetic anhydride under solvent-free conditions at room temperature (Scheme 37). This method shows preferential selectivity for the acetylation of the amino group in the presence of hydroxyl group.

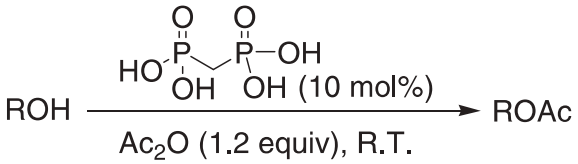

Scheme 37. *Acetylation of alcohols using methylenediphosphonic acid (MDP)*

The acetylation of alcohols, phenols, thiols, and amines with varied substitution using acid anhydrides has been reported to be catalyzed by Wells-Dawson heteropoly acid ($H_6P_2W_{18}O_{62}\cdot 24\ H_2O$) [47]. The reactions have been reported to proceed with very good to excellent yield in air at room temperature, using toluene as solvent (Scheme 38).

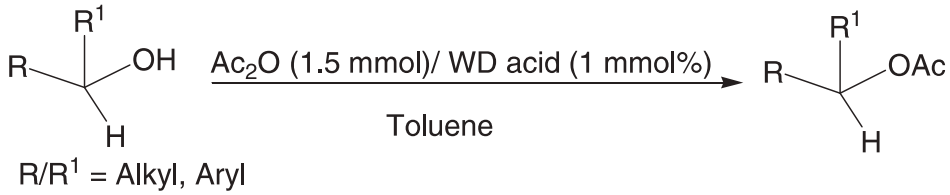

Scheme 38. *Acetylation of alcohols/phenols using Wells-Dawson heteropoly acid.*

H. Using Bases

Amongst different bases, pyridine is a popular catalyst for the acetylation of alcohols with acetic anhydride, but is toxic, has a bad smell, and its high boiling point makes its removal after the reaction difficult [48]. The use of acetyl chloride or acetic anhydride in presence of pyridine has been the most commonly used method for acetylation of alcohols, phenols, amines and thiols (Scheme 39).

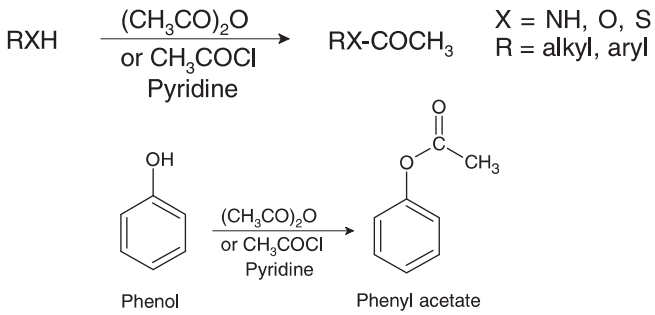

Scheme 39. *Acetylation of alcohols, phenols, anilines and thiols with acetyl chloride/acetic anhydride using pyridine.*

Another organic base, N,N′,N′-tetramethylethylenediamine (TMEDA) [49] has been used as a simple, mild and efficient catalyst for the

acetylation of alcohols, phenols and thiols at room temperature under solvent-free condition (Scheme 40). Acetylation reaction with acetic anhydride and benzoic anhydride proceeds with good to excellent yield in the presence of TMEDA as the catalyst.

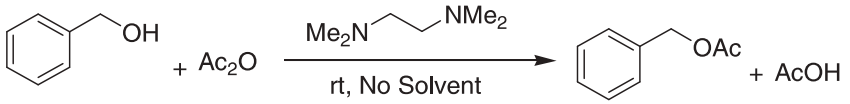

Scheme 40. *TMEDA catalyzed acetylation of benzyl alcohol*

Kazemi *et al* reported tetra-*n*-butyl ammonium hydroxide solution (TBAOH) [50] as an efficient catalyst for the acetylation of alcohols, phenols and thiols (Scheme 41).

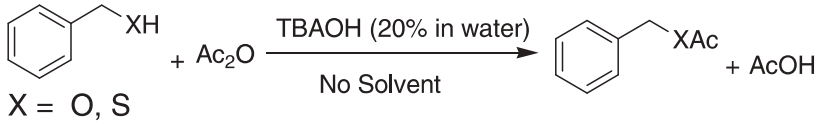

Scheme 41.*Acetylation of alcohols, phenols and thiols using tetra-n-butyl ammonium hydroxide solution*

I. Using molecular iodine

Acetylation of alcohols with vinyl acetate can be achieved by using molecular iodine [51] as catalyst (Scheme 43). Molecular iodine displays significant functional group tolerance, being compatible with methoxy, double bonds, spiroketals, ketals and phenolic hydroxyl functions (Scheme 42).

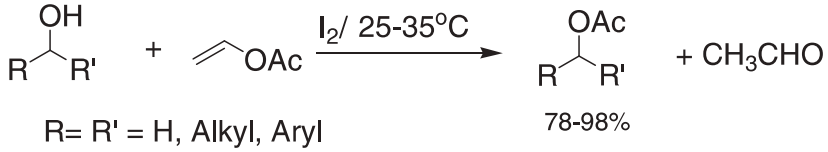

Scheme 42. *Acetylation of alcohols using molecular iodine.*

Ahmed *et al* [52] reported acetylation of a variety of alcohols, phenols and amines under solvent free conditions by using iodine in isopropenyl acetate (IPA) as a catalyst. Primary, secondary, tertiary alcohols, amines and mono to polyhydroxy phenols and anilines with electron donating or withdrawing substituents were converted *into* acetylated derivative in good to excellent yield at 85 to 90 °C (Scheme 43).

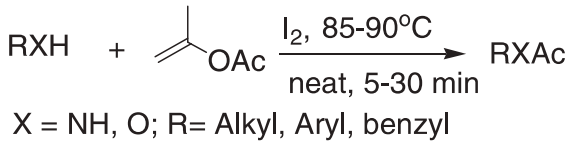

Scheme 43. *Acetylation of alcohols using iodine in isopropenyl acetate.*

III. Conclusion

Acetylation of alcohols, phenols and amines is usually carried out for the protection of OH and NH groups during the course of multistep organic synthesis, especially in the construction of polyfunctional molecules such as nucleosides, carbohydrates, steroids, and natural products. The reaction has been performed with a wide range of acid, base, metal salts, metal oxides and other catalysts under a variety of reaction conditions, thus offering a broad choice of catalysts and reaction conditions for specific targeting of OH and NH functionalities in the complex organic molecules. An interesting feature of catalyzed acetylation reaction is its chemoselectivity, *i.e.*, selective acetylation of primary alcoholic groups in the presence of secondary and tertiary or of alcoholic groups in the presence of phenolic as well as amino groups.

IV. References

[1] T. W. Greene and P. G. M. Wuts, in protective groups in organic synthesis", 4th Edition, Wiley, New York (2006) ISBN: 978-0-471-69754-1.

[2] P. J. Kocienski, "Protecting Groups"; Thieme: Stuttgart, 1994.

[3] W. Steglich, G. Hofle, "N,N-Dimethyl-pyridinamine, a very effective acylation catalyst" Angew. Chem., Int. Ed. Engl. 8 (1969) 981-989.

[4] E. Vedejs, T. S. Diver, "Tributylphosphine: A remarkable acylation catalyst" J. Am. Chem. Soc. 115 (1993) 3358-3359.

[5] E. F. V. Scriven, "4-Dialkylaminopyridines: super acylation and alkylation catalysts" Chem. Soc. Rev. 12 (1983) 129-161.

[6] S. Tomohumi, O. Kousaburo, O. Takashi, "Remarkably fast acylation of alcohols with benzoyl chloride promoted by TMEDA" Synthesis (1999) 1141-1144.

[7] B. Karimi, J. Maleki, "Lithium trifluorosulfonate as a recyclable catalyst for highly efficient acetylation of alcohols and diacetylation of aldehydes under mild and neutral reaction conditions" J. Org. Chem. 68 (2003) 4951-4956.

[8] R. Alleti, M. Perambuduru, S. Samanha, V. P. J. Reddy, Gadolinium triflate: an efficient and convenient catalyst for acetylation of alcohols and amine J. Mol. Catal. A: Chem. 226 (2005) 57-59.

[9] J. Iqbal, and R. R. Srivatava, "Cobalt (II) chloride catalyzed acetylation of alcohols with acetic anhydride: scope and mechanism"*J. Org. Chem*. *57* (1992) 2001-2007.

[10] S. Mulla, S. Inamdar, M. Pathan and S. Chavan, "Highly efficient cobalt (ii) catalyzed O-acetylation of alcohols and phenols under solvent-free conditions," Open Journal of Synthesis Theory and Applications, 1 (2012) 31-35.

[11] R. Fatemeh, "A heterogeneous cobalt (II) Salen complex as an efficient and reusable catalyst for acetylation of alcohols and phenols" Tetrahedron Lett. 50(2009) 395-397.

[12] E. Torregiani, S. Gianfranco, A. Minassi and G. Appendino, "Cerium (III) Chloride-promoted chemoselective esterification of phenolic alcohols," Tetrahedron Letters, 46 (2005) 2193-2196.

[13] G. A. Meshram and V. D. Patil, "Simple and efficient method for acetylation of alcohols, phenols, amines, and thiols using anhydrous $NiCl_2$ under solvent-free conditions" Synthetic Communications, 39 (2009) 4384-4395.

[14] S. Chandrashekhar, T. Ramchandar, and T. Mohamed, "Acetylation of alcohols with acetic anhydride catalyzed by $TaCI_5$" Tetrahedron Lett. 39 (1998) 3263-3266.

[15] A. K. Chakraborty and R. Gulhane, "Zirconium(IV) Chloride as a new, highly efficient, and reusable catalyst for acetylation of phenols, thiols, amines, and alcohols under solvent-free conditions," Synlett, 4 (2004) 627-630.

[16] V. R Choudhary, K. Y Patil and S. K Jana; "Acetylation of aromatic alcohols and phenols over $InCl_3$/montmorillonite K-10 catalysts" J. Chem. Sci., 116 (2004) 175177.

[17] J. S. Yadav, A. V. Narsaiah, B. V. S. Reddy, A. K. Basak, and K. Nagaiah,"Niobium (V) chloride: an efficient catalyst for selective acetylation of alcohols and phenols" J. Mol. Catal. A. 230 (2005) 107-111.

[18] S. T. Reddy, M. Narasimhulu, N. Suryakiran, C. K. Mahesh, K. Ashalatha, and Y. Venkateswarlu "A mild and efficient acetylation of alcohols, phenols and amines with acetic anhydride using $La(NO_3)_3 \cdot 6H_2O$ as a catalyst under solvent-free conditions" *Tetrahedron Lett*. *47* (2006) 6825-6829.

[19] P. Yadav, R. Lagarkha, and A. Zahoor, "Comparative study of acetylation of alcohols and phenols with different acetylating agents using zinc chloride as catalyst under solvent free conditions at room temperature" Asian. J. Chem. 22, (2010) 5155-5158

[20] F. N. Lugemwa , K. Shaikh and E. Hochstedt., "Facile and efficient acetylation of primary alcohols and phenols with acetic anhydride catalyzed by dried sodium bicarbonate" Catalysts 3 (2013) 954-965.

[21] S. Naik, G. Bhattacharjya, V. R. Kavala, and B. K. Patel; "Mild and eco-friendly chemoselective acetylation of amines in aqueous medium" ARKIVOC i (2004) 55-63.

[22] M. Kazemi,, H. Kohzadi, and Z. Noori, "Potassium carbonate: a highly efficient catalyst for the acetylation of alcohols, phenols and thiols under mild conditions" Iranian Chem. Commun. 2 (2014) 39-47.

[23] S. S. Praveen, K. Darsi, K. S. Nagamani, B. Rama Devi, A. Naidu and P. K. Dube, "Studies on N-acetylation of anilines with acetyl chloride using phase transfer catalysts in different solvents" Der Pharma Chemica, 3 (2011) 35-38.

[24] M. H. Sarvari, and H. Sharghi, "Zinc oxide (ZnO) as a new, highly efficient, and reusable catalyst for acetylation of alcohols, phenols and amines under solvent free conditions" Tetrahedron 61 (2005) 10903-10907.

[25] F. Tamaddon, M. A. Amrollahi, and L. Sharafat, "A green protocol for chemoselective O-acetylation in the presence of zinc oxide as a heterogeneous, reusable and eco-friendly catalyst" Tetrahedron Lett. 46(2005) 7841-7844

[26] F. Rajabi, and R. Laque; "Solventless acetylation of alcohols and phenols catalysed by supported iron oxide nanoparticles" Catalysis communication 45 (2014) 129-132.

[27] A. Zarei, A. R. Hajipour, and L. Khazdooz, "P_2O_5/Al_2O_3 as an efficient heterogeneous catalyst for the acetylation of alcohols, phenols, thiols, and amines under solvent-free conditions," *Synth. Commun. 41* (2011) 1772-1785.

[28] A. Orita, C. Tanahashi, A. Kakuda, and J. Otera, "Highly efficient and versatile acetylation of alcohols with $Bi(OTf)_3$ as catalyst" Angew. Chem., Int. Ed. 39 (2000) 2877-2879.

[29] M. Moghadam, S. Tangestaninejad, V. Mirkhani, I. Mohammadpoor-Baltork, M. Babaghanbari, M. Zarea, L. Shariati and S. A. Taghavi; "Zirconyltriflate: A new, highly efficient and reusable catalyst for acetylation and benzoylation of alcohols, phenols, amines and thiols with acetic and benzoic anhydrides" J. Iran. Chem. Soc. 6 (2009) 523-532.

[30] R. Dalpozzo, D. A. Nino, L. Maiuolo, A. Proeopio, M. Nardi, G. Bartoli, and R. Romeo, "Highly efficient and versatile acetylation of alcohols catalyzed by cerium (III) triflate," Tetrahedron Lett. 44 (2003) 5621-5624.

[31] K. Ahmed, K. A. Naseer, R. Srinivasan, V. Y. Srikanth, and T. Krishnaji, "$Al(OTf)_3$ as a highly efficient catalyst for the rapid acetylation of alcohols, phenols and thiophenols under solvent-free conditions," Tetrahedron Lett., 48 (2007) 3813-3818.

[32] H. -J. Yoon, S. -M. Lee, J. -H. Kim, H. -J. Cho, J. -W. Choi, S. -H. Lee and Y. -S. Lee, "Polymer-supported gadolinium triflate as a convenient and efficient Lewis acid catalyst for acetylation of alcohols and phenols" Tetrahedron Lett. 49 (2008) 3165-3171.

[33] A. S. Taghavi, M. Moghadam, S. Tangestaninejad, I. Mohammadpoor-B, S. Tangestaninejad, V. Mirkhani, and R. A. Khosropour, "Investigation of catalytic activity of high-valent vanadium(IV) tetraphenylporphyrin: A new, highly efficient and reusable catalyst for acetylation of alcohols and phenols with acetic anhydride" Inorg. Chimica. Acta. 377 (2011) 159-166.

[34] R. Das, and D. Chakraborty, "Silver triflate catalyzed acetylation of alcohols, thiols, phenols, and amines AgOTf-catalyzed Acetylation of Alcohols, Thiols, phenols, and Amines" Synthesis 10 (2011) 16211625.

[35] J.N. Baldwin, N. A. Nord, D. B. O'Donnell, and S. R. Mohan "Iron(III) tosylate catalyzed acetylation of alcohols, phenols, and aldehydes" Tetrahedron Lett. 53 (2012) 6946-6949

[36] R. K. Sodhi, V. Kumar, and S. Paul, "$M(acac)_n$ covalently anchored onto amine functionalized silica: highly efficient and recyclable heterogeneous catalysts for the acetylation of amines, phenols and alcohols under solvent-free conditions" *The Open Catalysis Journal*, *6* (2013) 1-7.

[37] M. Moghadam, S. Tangestaninejad, V. Mirkhani, I. Mohammadpoor-B, and A. S. Taghavi, "Highly efficient and selective acetylation of alcohols and phenols with acetic anhydride catalyzed by a high-valent tin(IV) porphyrin, $Sn(TPP)(BF_4)_2$" J. Mol. Cata. A: Chemical. 274 (2007) 217-223.

[38] E. J. Taylor, M. J. J. Williams, and D. S. Bull, "N-Acyl 1,5-diazabicyclo[4.3.0]non-5-ene (DBN) tetraphenylborate salts as O-acylating agents" Tetrahedron Lett. 53 (2012) 4074-4076.

[39] M. A. Pasha, M. B. M. Reddy and K. Manjula; "Zinc dust: An extremely active and reusable catalyst in acetylation of phenols, thiophenol, amines and alcohols in a solvent-free system" Eur. J. Chem. 1 (2010) 385-387.

[40] M. R. Fard, B. Akhlaghinia and S. Rezazade; "Polyvinyl alcohol immobilized N-ethyl sulfamic acid ($PVA\text{-}NHSO_3H$) as an efficient catalyst for rapid and selective acetylation of phenols, alcohols, amines and thiols under solvent free conditions" J. Indian Chem. Soc., 92 (2015) 1715-1728.

[41] D. Habibi, P. Rahmani, and Z. Akbaripanah; "Acetylation of phenols, anilines, and thiols using silica sulfuric acid under solvent-free conditions" Journal of Chemistry 2013 (2013) 1-9. Article ID 268654.

[42] A. R. Massah, R. J. Kalbasi, M. Khalifesoltani, and F. M. Kordesofla; "$ZSM\text{-}5\text{-}SO_3H$: An efficient catalyst for acetylation of sulfonamides, amines, alcohols, and phenols under solvent-free conditions" ISRN Organic Chemistry, 2013 (2013) 1-12. Article ID 951749.

[43] S. Farhad, A. Z. Mohammad, A. Ali-Reza, "Efficient acetylation of alcohols, phenols, and amines catalyzed by melamine trisulfonic acid" Synth. Commun. 40 (2010) 1022-28.

[44] A. K. Chakraborti, and R. Gulhane, "Fluoroboric acid adsorbed on silica gel as a new and efficient catalyst for acetylation of phenols, thiols, alcohols, and amines" , Tetrahedron let. 44 (2003) 3521.

[45] R. H. Tale, and R. N. Adude, "A novel 3-nitrobenzeneboronic acid as an extremely mild and environmentally benign catalyst for the acetylation of alcohols under solvent-free conditions" *Tetrahedron Lett. 47(*2006) 7263-7265.

[46] M. Xie, H. Wang, J. Wu, Y. He, Y. Liu, and P. Zou "Highly efficient and versatile acetylation of alcohols, phenols and amines catalyzed by methylenediphosphonic acid (mdp) under solvent-free conditions" J. Chil. Chem. Soc., 56 (2011) 884-886.

[47] G. P. Romanelli, D. O. Bennardi, J. C. Autino, G. T. Baronetti, and H. J. Thomas, "A simple and mild acetylation of alcohols, phenols, amines, and thiols with a reusable heteropoly acid catalyst ($H_6P_2W_{18}O_{62}\cdot 24\,H_2O$)" E-Journal of Chemistry, 5 (2008) 641-647.

[48] T. G. Bonner and P. McNamara,"The pyridine-catalysed acetylation of phenols and alcohols by acetic anhydride" J. Chem. Soc. B, (1968) 795-797.

[49] S. T. Kadam, H. Lee, and S. S. Kim; "TMEDA: Efficient and mild catalyst for the acetylation of alcohols, phenols and thiols under solvent-free condition" Bull. Korean Chem. Soc. 30 (2009) 1071-1076.

[50] M. Kazemi and M. S. Beigi, "Tetra-N-butyl ammonium hydroxide as highly efficient for the acetylation of alcohols, phenols and thiols" Organic Chem Curr Res 2 (2013) 2.

[51] J. W. Bosco, A. Aditya, and A. K. Saikia, "Molecular iodine catalyzed selective acetylation of alcohols with vinyl acetate" Tetrahedron Lett. 47 (2006) 4065-4068.

[52] N. Ahmed, and E. Van Lier, "Molecular iodine in isopropenyl acetate (IPA): a highly efficient catalyst for the acetylation of alcohols, amines and phenols under solvent free conditions" Tetrahedron Lett. 47 (2006) 5345-5349.

Curr. Rep. Sci. & Tech. 2 (1) (2016) 95-99

Dielectric Response of Silver Ion Induced PEN (Poly Ethylene Naphthalate)

Kusam Devgan
Department of Physics, S.R. Government College for Women, Amritsar, India
kusamdevgan93@yahoo.com

Abstract

Silver ion induced PEN (Poly ethylene naphthalate) films were examined to study variation of dielectric loss with respect to frequency. Silver ion beam (120 MeV) was used to analyze the modifications induced by swift heavy ions as a function of ion fluence, ranging from $3x10^{11}$ to $3x10^{12}$ ions/cm^2. Dielectric loss for irradiated samples increases with the increase in ion fluence.

Keywords

Irradiation effects, Dielectric properties, thin films, Polymer, Poly ethylene naphthalate.

I. Introduction

Polymeric materials due to a variety of properties such as low density, ability to form complex shapes and low fabricating cost have great prospective in many important applications. However, because of their surprising dielectric properties and inherent softness, the use of polymers is still limited [1]. The properties of polymers get altered due to radiation induced crosslinking and have successfully been used in industries widely. Polymers that are not highly cross-linked have properties that depend greatly on the forces that act between the chains. The most evident effect of cross linking is that it prevents the polymer from either melting or dissolving, because the solvent forms a swollen gel with the polymer rather than a solution, due to the cross links not being broken and this consequence is used in the formation of super absorbent polymers, On irradiating the polymers with ionizing radiations, ions and radicals are produced [2]. PEN is produced by the condensation polymerization of 2,6-naphtalenedicarboxylic acid and ethylene glycol [3-5]. In the last few years the dielectric constant spectroscopy has proven to be a very useful tool for

studying the structure and the dynamics of polymeric systems [6-9]. This knowledge is also important for t provable he development of new materials for industrial applications, with specific electrical properties. Particularly, the conducting polymers have been offered for use as conducting wires, electromagnetic shielding materials [10, 11], light emitting diodes [12], sensors [13], etc. The aim of the present investigation is to study the alterations in dielectric loss of PEN films caused by silver ion (120 MeV) irradiation with the help of Dielectric techniques.

II. Experimental Details

The specimens of Poly ethylene naphthalate (PEN) in the form of flat polished thin films (25m) were procured from Good Fellow Ltd. (England). The samples were mounted on the sliding ladder and irradiated with silver (120 MeV) ion beams using 15 UD pelletron facility for the general purpose scattering chamber (GPSC) under vacuum of ~10-6 Torr at Inter-University Accelerator Center, New Delhi. The electronic energy loss, nuclear energy loss and ion range of polymers of characterize silver (120 MeV) ions in PEN polymer is ~5.49, 965.5 and 2.353 E+01 eV/Å respectively [14]. The ion beam fluence was varied from 3 x 1011 to 3 x 1012 ions cm^{-2}. The beam current was kept low to suppress thermal decomposition and was monitored intermittently with a Faraday cup. The ion beam fluence was varied from 1 x 1011 to 1 x 1012 ions cm^{-2}. Doses (Table 1) for the given fluence were calculated using the formula [15] as given below:

$$\text{Dose} = 1.602 \times 10^{-10} \times \frac{1}{\rho} \times \frac{dE}{dx} \times \phi \quad (1)$$

ϕ : Ion fluence,

ρ: Density of polymer,

$\frac{dE}{dx}$: Stopping power of ion

Table 1: *Doses for given fluence of silver ion of studied polymer*

Polymer	Ion Fluence (ions/cm^2)	Silver (120 MeV) (kGy)
PEN	Pristine	0.00
	3×10^{11}	3411.78
	3×10^{12}	34117.87

The Precision impedance analyzer 6500B is used to measure dielectric loss of pristine and irradiated samples of PEN films at room temperature in the frequency range 20Hz-1MHz.

III. Results And Discussion

The dielectric loss of pristine and irradiated samples of Poly ethylene naphthalate (PEN) was calculated. The graphs for variation of dielectric loss with frequency for pristine and irradiated samples of Poly ethylene naphthalate (PEN), irradiated with silver ions are shown in Fig. 1. It is observed from the plots that dielectric loss lessens with increase in frequency. This may be due to the fact that the charge carriers migrate through the dielectric and get trapped against a defect site, hence opposite charge is induced, which slow down the motion of charge carriers. It is also observed from Fig. that the value of dielectric loss of irradiated samples of Poly ethylene naphthalate (PEN) is more than that of pristine sample. This is due an increase in number of free radicals occurred due to chain scission process [16]. The increase in dielectric loss with increase in ion fluence contributes to the increase in rigidity of polymer due to irradiation [17].

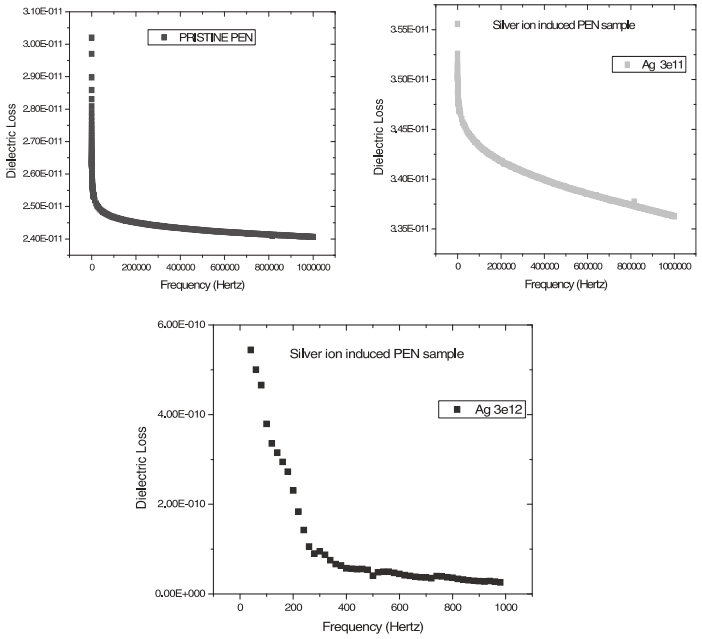

Fig.1. *Dielectric spectra of Poly ethylene naphthalate (PEN) samples irradiated with different fluences of silver ions.*

IV. Acknowledgments

The author wishes to thanks IUAC (Inter-University Accelerator Center), New Delhi, for providing the swift heavy ion facility. The Department of Electronics Technology, Guru Nanak Dev University, Amritsar is gratefully acknowledged for Dielectric studies.

V. References

[1] Y. Wu, T. Zhang, H. Zhang, X. Xhang, Z. Deng, and Gu Zhou, "Electrical Properties of Polymer Modified by Metal Ion Implantation," Nucl.Instr. and Meth. B 169 (2000) 89-93.

[2] A. Chapiro,"Chemical modifications in irradiated polymers," Nucl.Instr. and Meth. B 32 (1988) 111-114.

[3] V. Tsanaktsis, D.G. Papageorgiou, S. Exarhopoulos, D.N. Bikiaris, and G.Z. Papageorgiou, "Crystallization and Polymorphism of Poly (ethylene furanoate)," American Chem. Socie. 15 (2015) 55055512.

[4] K. Miyata, H. Ito, T. Kikutani, and N. Okui, "Structural Change of High-Speed Spun Poly (ethylene naphthalene dicarboxylate) Fibres with Annealing" The Society of Fiber Science and Technology 55 (2008) 542-551.

[5] I.O. Igwe, "Uptake of Aromatic Solvents by Polyethylene Films,"Appl. Polym. Sci. 104 (2007) 3849-3854.

[6] G. Williams, "Keynote lectures in selected topics of polymer science". Madrid: CSIC; 1997.

[7] J. Runt, and J. Fitzgerald, "Dielectric spectroscopy of polymeric materials," American Chemical Society Washington, 1997.

[8] A. Blythe, "Electrical properties of polymers," Cambridge, University Press Cambridge 1979.

[9] P. Hedvig, "Dielectric spectroscopy of polymers," Adam Hilger, Bristol, 1977.

[10] J. Joo, and J. Epstein, "Crossover in electrical frequency response through an insulator metal transition," Appl Phys Lett, 65 (1994) 22782280.

[11] A. Andre, PhD Thesis, Paris, 1996.

[12] J. Burroughes, D. Bradley, A. Brown, R. Marks, K. Mackay, and H. Friend, "Light-emitting diodes based on conjugated polymers," Nature .347 (1990) 539541.

[13] J. Yue, and A. Epstein, "Electronic control of PH at sulfonated polyaniline electrodes," J Chem Soc, Chem Commun 21 (1992) 15401542.

[14] J.F. Ziegler, M.D. Ziegler, and J.P. Biersack, "SRIM - the stopping and range of ions in matter," Nucl. Instr. and Meth. in Phys. Res. B 268 (2010) 1818-1823.

[15] O.B. Geiβ, M. Kramer, and G. Kraft, "Efficiency of thermo-luminescent detectors to heavy charged particles" Nucl. Instr. Meth. Phys. Res. B, 142 (1998) 592-598.

[16] T. Phunkan, D. Kanjilal, T.D. Goswami and H.L. Das, "Dielectric response of irradiated PADC polymer track detector," Nucl. Instr. and Meth. in Phys. Res. B 234 (2005) 520-524.

[17] T. Phunkan, D. Kanjilal, T.D. Goswami and H.L. Das, "Dielectric response of heavy ion irradiated PADC track detector," Nucl. Instr. and Meth. in Phys. Res. B 155 (1999) 116-119.

Curr. Rep. Sci. & Tech. 2 (1) (2016) 100-104

Investigation of the Optical Properties of ($70B_2O_3$-$29Bi_2O_3$-$1Dy_2O_3$) xBT Glasses under the Influence of Gamma Irradiation

Vanita Thakur[1], Anupinder Singh[1], Vibha Chopra[2], Sonika Thakur[3] and Lakhwant Singh[1]
[1]Department of Physics, Guru Nanak Dev University, Amritsar 143005
[2]Department of Physics, D.A.V. College, Amritsar 143001,
[3]Department of Physics, GNDU College Verka, Amritsar 143001
vanita.thakur88@gmail.com

Abstract

The glass samples with composition($70B_2O_3$-$29Bi_2O_3$-$1Dy_2O_3$) xBT; wherex = 0, 5, 10, 15, 20 and 25 weight percent, have been synthesised by melt quench method. The prepared glass samples were irradiated with different gamma doses using a ^{60}Co radioisotope. UV-Vis spectroscopic measurements have been performed on the irradiated samples to study theinfluence of gamma radiations on the optical properties of the samples. A decrease in the band gap energy (E_g) calculated from Tauc's plots has been observed after irradiation which may be attributed to the defects formation in the glass matrix.

Keywords

Glass, Barium titanate (BT), Gamma irradiation,Band gap energy.

I. Introduction

Now a days, there is an increasing use of gamma radiations in the field of medicine and industry, optical fibre waveguides,space craft and also in nuclear power plants [1, 2]. Therefore, the study of the irradiation effects on the glasses has drawn much attention of the researchers.The glasses have been found to be a good alternative of concrete which is usually used in shielding purposes [2, 3]. Bismuth based borate glasses are supposed to have good radiation shielding properties and find their use in the nuclear engineering applications [4, 5, 6]. Barium also play an important role in radiation glass shielding and is considered as a good replacement to lead (Pb) due to environmental toxicity of Pb. In the present work, the effect of

gamma irradiation on the optical properties of ($70B_2O_3$-$29Bi_2O_3$-$1Dy_2O_3$)-*x*BT glasses has been reported. Since, irradiation is supposed to bring some structural changes in the glass matrix which in turn affects the various structural, physical and optical properties of the glasses. These changes are found to depend on the type and dose of radiation and on the composition of glass [4].

II. Sample Preparation and Characterization

A series of glass samples with composition ($70B_2O_3$: $29Bi_2O_3$: $1Dy_2O_3$) *x*BT; *x*=0, 5, 10, 15, 20, 25 weight percent, was prepared by conventional melt quench technique, as discussed elsewhere [7].

A. Gamma Irradiation

The prepared glass samples studied in the present work were irradiated at room temperature by γ-rays using ^{60}Co γ-irradiator *(Gamma* Chamber-1200) with the dose rate of 7.5 kGy/h, at IUAC, New Delhi. The samples were exposed to different doses of 50 kGy, 100 kGy, 200 kGy.

B. Optical Absorption Measurements

In order to study the effect of gamma irradiation on the optical properties of the given glasses, the optical absorption measurements were carried out on well-polished glass samples using Shimadzu-1601 double beam UV-Vis Spectrophotometer in the wavelength range 200-900 nm.

III. Results and Discussion

The UV-Vis optical absorption spectra for the glass samples with composition ($70B_2O_3$-$29Bi_2O_3$-$1Dy_2O_3$)-*x*BT have been recorded at room temperature. The absorption coefficient α(ν) has been determined by the relation [8]:

$$\alpha(\nu) = \frac{A}{t} \quad (1)$$

where 'A' is the absorbance and 't' is the thickness of the sample.

Tauc's plots have been used for the estimation of the optical band gap energies of the samples using the relation [8, 9]:

$$\alpha h\nu = B\,(h\nu - E_g)^n \quad (2)$$

where B is the band tailing parameter, hν is the incident photon energy and n is a constant that determines the type of optical transitions. In the present

case, indirect optical band gap energies (E_g) have been calculated using n = 2. The plots between $(\alpha h\nu)^{1/2}$ and ($h\nu$), known as Tauc's plot have been used to calculate optical band gap energies of the prepared samples. Fig.1shows the Tauc's plots for the samples irradiated with 50 kGy and 100 kGy doses. In the similar way, we calculated the values for the sample irradiated with 200kGy. The values of band gap energy (E_g) obtained from the plots are listed in Table 1 and their behavior is depicted in Fig. 2. The values of E_g for the pristine sample have already been reported [7]

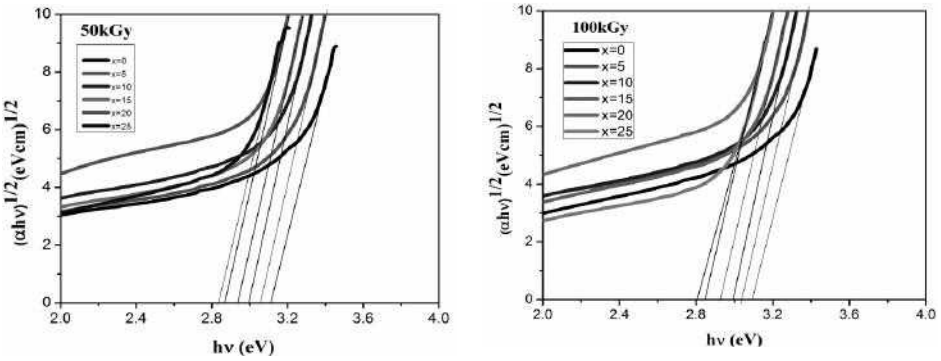

Fig1. *Tauc's plot for ($70B_2O_3$-$29Bi_2O_3$-$1Dy_2O_3$)-xBT glass samples after irradiation.*

Perusal of the data indicates that there is a decrease in the values of optical band gap energies after irradiation. This decrease in values of E_g can be related to the defects formation in the glass structure with irradiation. Since, irradiation of the glass samples causes displacements of ions and breaking of bonds, which results in the structural modifications in the glass matrix [10,11]. So, these changes in the structure can be responsible for the decrease in band gap energy. Also, from the table 1 it is clearly observed that with an increase in *x*, there is less decrease in value of E_g with irradiation, suggesting that with addition of BT, the glass system becomes radiation resistant.

Table 1. *Values ofIndirect optical band gap energy (E_g) for ($70B_2O_3$-$29Bi_2O_3$-$1Dy_2O_3$)-xBT glass system at different doses.*

Sample code	0kGy	50 kGy	100 kGy	200 kGy
x = 0	3.29	3.11	3.09	3.04
x = 5	3.23	3.06	3.04	2.94
x = 10	3.12	3.00	2.99	2.93
x = 15	3.02	2.94	2.92	2.91
x = 20	2.99	2.87	2.85	2.80
x = 25	2.91	2.84	2.81	2.76

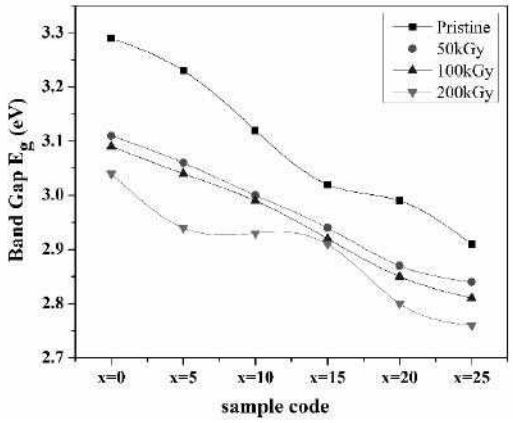

Fig 2. *Behaviour of optical band gap energy (E_g) for the irradiated glass samples at different doses.*

IV. Conclusions

A decrease in the band gap after gamma irradiation indicates the defects formation in the glass matrix. However, this decrease is found to be less in the glass samples with an increased amount of barium titanate. This leads to the conclusion that with an increase in the BT content in the glasses, they become more resistant to the gamma radiations. Hence such glasses can be considered as the potential candidates for radiation shielding purposes in the nuclear industry.

V. Acknowledgments

One of the authors, Vanita Thakur, wishes to thank University Grants Commission (UGC) for financial assistance through UGC-BSR fellowship. The authors also thank IUAC New Delhi, for providing Gamma irradiation facility.

VI. References

[1] S.Y. El-Kameesy, S. Abd El-Ghany, M. Abd El-Hakam Azooz, Y. Abd Allah El-Gammam, "Shielding Properties of Lead Zinc Borate Glasses". World Journal of Condensed Matter Physics, 3(2013) 198-202.

[2] R. Kaur, S. Singh, O.P. Pandey, "FTIR structural investigation of gamma irradiated $BaONa_2OB_2O_3SiO_2$ glasses". Physica B, 407 (2012) 4765-4769.

[3] H. Singh, K. Singh, L. Gerward, H.S. Sahota and R. Nathuram, "ZnO-PbO-B_2O_3 Glasses as Gamma-Ray Shielding Materials". Nuclear Instruments and Methods in Physics Research Section B: Beam Interactions with Materials and Atoms, 207 (2003) 257-262.

[4] M.A. Marzouk, F.H. El Batal, "UV-visible and infrared absorption spectra of Bi_2O_3 in lithium phosphate glasses and effect of gamma irradiation". Appl Phys A, 115(2014)903912.

[5] M.A. Marzouk, "Optical characterization of some rare earth ions doped bismuth borate glasses and effect of gamma irradiation". Journal of Molecular Structure, 1019 (2012) 8090.

[6] A.M. Abdelghany, H.A. El Batal and L.K. Marei, "UV-visible and infrared absorption spectra of Bi_2O_3 in lithium phosphate glasses and effect of gamma irradiation". Appl Phys. A, 115(2014) 903912.

[7] L. Singh, V. Thakur, R. Punia, R.S. Kundu, A. Singh, "Structural and optical properties of barium titanate modified bismuth borate glasses" Solid State Sci.37 (2014) 6471.

[8] R.S. Kundu, Sunil Dhankhar, R. Punia, Kirti Nanda, N. Kishore, "Bismuth modified physical, structural and optical properties of mid-IR transparent zinc boro-tellurite glasses". Journal of Alloys and Compounds 587(2014) 6673.

[9] R. Punia, R.S. Kundu, J. Hooda, S. Dhankhar, S. Dahiya, N. Kishore, "Effect of Bi_2O_3 on structural, optical and other physical properties of semiconducting zinc vanadate glasses". Journal of Applied Physics, 110 (2011) 033527.

[10] G. Sharma, K. S. Thind, Monika, H. Singh, Manupriya, and L. Gerward, "Optical properties of heavy metal oxide glasses before and after gamma-irradiation". Phys. stat. sol. 204 (2007) 591601.

[11] F. El-Diasty, F. A Abdel Wahab, "Optical Band Gap Studies on Lithum Aluminium Silicate glasses doped with Cr_{3+} ions". Journal of Applied Physics, 100(2006) 093511.

Curr. Rep. Sci. & Tech. 2 (1) (2016) 105-111

Estimation of indoor and outdoor gamma dose rate exposure levels in Jammu district, *Jammu & Kashmir*, India

Manpreet Kaur[1], Ajay Kumar[2] and Rohit Mehra[1]
[1]Department of Physics, Dr. B. R. Ambedkar National Institute of Technology, Jalandhar 144001, India
[2]Department of Physics, DAV College, Amritsar 143001, Punjab, India
ajay782@rediffmail.com

Abstract

A preliminaryoutdoor and indoor gamma ray dose rate has been measured in selected 40 villages of Jammu district of Jammu and Kashmir, India at one meter above the ground surface using Dosimeter-Radiometer MKS-03D (SARAD). Selected villages characterised into three different zones according to obtained outdoor gamma ray dose rate. This survey was designed in such a way so as to obtain a uniform and representative distribution of measurements locations. The mean gamma ray dose rate in outdoor amounts to 0.15±0.04 μSvh^{-1} and indoor amounts to 0.13±0.04 μSvh^{-1} in all three zones respectively. The overall average annual outdoor and indoor equivalent dose rate was 163.25± 46.58 μSvy^{-1} and 560.16±98.34 μSvy^{-1} respectively.Moreover, indoor equivalent dose rate was found higher than outdoor equivalent dose rate.The results revealed that the dose levels in all of the locations (indoor and outdoor) were below the 1000 μSvy^{-1} maximum permissible limit for the public set by International Commission on Radiological Protection (ICRP). Therefore, the present area is radiologically safe for health hazard point of view.

Keywords

Gamma ray dose rate, atmosphere, equivalent dose, exposure.

I. Introduction

The radiation is present in every environment of the earth's surface, beneath the earth and in the atmosphere. Man is by the very nature of his

environment exposed to varying amounts of ambient radiation with or without his consent.Gamma radiation from radionuclides which are characterized by half-lives comparable to the age of the earth, such as K40 and the radionuclides from the U^{238} and Th^{232} series,and their decay products, represents the main external source of irradiation to the human body [1].The terrestrial gamma rays originated from radioactive nuclides vary significantly, depending on the geological and geographical features of a region [2]. The world average value of the annual effective dose by natural radiation is about 2.4 mSv [1] out of which 52% is due to inhalation exposure and 92% of this fraction is contributed by the radioactive element radon and its progenies.Among all radionuclides, radon contributes high amount of potentially lethal due to lung cancer [3]. Exposure to ionizing radiation poses a high health risk and this risk may include cancer induction, radiation catractogenesis, and indirect chromosomal transformation because of the health risk [4]. The knowledge of the natural radioactivity inside the buildings is important for the determination of population exposure to radiations, as most of the residents spend about more than half of their time in indoor. Indoorand outdoor gamma dose rate measurements have been carried out in several countries [2-7], aimed at obtaining the distribution of gamma radiation exposure in representative dwellings and to evaluate the risk associated with this exposure.

The study of indoor and outdoor gamma radiation exposure has been carried out first time in Jammu district, Jammu and Kashmir, India. The objective of our study was to carry out an evaluation of the assessment of radiation gamma doserate and equivalent effective dose exposed by the inhabitants living outside and inside the houses.

II. Geology

The study area of the Jammu district, Jammu and Kashmir extends geographically from the latitudes 32°33'07" to 33°07'30" North and longitudes 73°51'19" to 75°08'52" East as shown in the Fig.1. District Jammu falls in Sub Mountains regions in the foot hills of the Himalayas. This district is bounded by rajouri district in the west, Udhampur in north and northwest and kathua in the south. Geologically, the area of the district is divisible in two distinct areas, the northern hilly area underlain by siwalik

rocks and the southern outer plain area underlain by the sediments. The siwalik group is delimited by the lesser Himalaya to the north andindo-gangetic plain to the south. The group is located between the main boundary thrust (MBT) in north and the himalayan frontal thrust (HFT) in south. In Jammu mainly alluvial soils are found, which are loamy with little clay content and contain small quantity of lime with high magnesium content. The soils are generally mixed with pebbles. These soils are generally acidic in nature, deficient in potash, phosphoric and lime.The rock formation of Jammu area belongs to upper siwalik group which comprises mainly the sandstones, clays and boulder conglomerates and intercalation of sandstone.

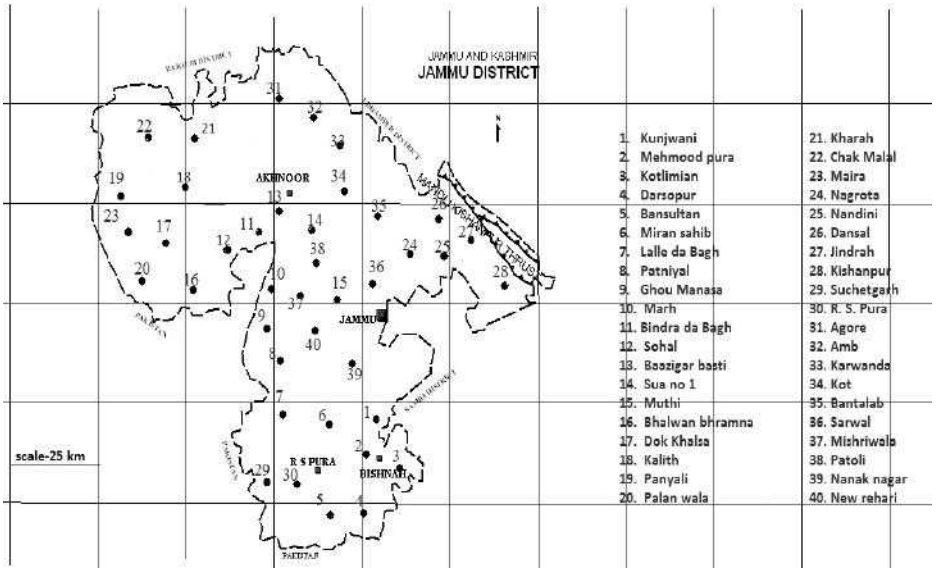

Fig 1. Geological map of surveyed area of Jammu district, Jammu and Kashmir, India.

III. Methodology

A preliminary survey has been carried out in Jammu district of Jammu and Kashmir, India to select the villages in such a way so that total area has been covered. Total of 40 villages have been selected. A measurement of ambient outdoor and indoor gamma dose rate has been done in such villages by using Dosimeter-Radiometer MKS-03D (SARAD) gamma detector meter at about 1 m above the ground surface. It is a G M tube based

survey meter with a digital display. Due to the random nature of the radioactive decay, the radiation exposure rate changes rapidly with time. In order to average out the exposure level of a given locations, 10 to 15 readings were taken for 10-15min. Results of the measurements of absorbed dose rate in environmental air are reported in units of micro Sievert per hour (μSvh^{-1}).The selected villages have been divided into three different zones depend upon obtained outdoor gamma dose rate. Eight (20%), twenty five (62.5%) and seven (17.5%) villages have been selected in first, second and third zones with outdoor gamma dose rate ranges of 0-0.10 μSvh^{-1}, 0-0.20 μSvh^{-1} and >0.20 μSvh^{-1}.The data obtained for the external and internal exposure rate in μSvh^{-1} was converted into absorbed dose rate $nGyh^{-1}$using conversion factor 870 $nGyh^{-1}$ [5].

A. Estimation of Annual Effective Dose Equivalent (AEDE)

The annual dose resulting from the absorbed dose attributed to gamma-ray emission from the radionuclides (Ra^{226}, Th^{232} and K^{40}) is obtained using following formula [4, 5]:

$$\text{AEDE (Indoor) } (\mu Svy^{-1}) = \text{Absorbed dose } (nGyh^{-1}) \times T_{exp} \times OF_{int} \times DCF \times 10^{-3} \quad (1)$$

$$\text{AEDE (Outdoor) } (\mu Svy^{-1}) = \text{Absorbed dose } (nGyh^{-1}) \times T_{exp} \times OF_{ext} \times DCF \times 10^{-3} \quad (2)$$

where T_{exp} is the exposure duration per year i.e. $8760hy^{-1}$,OF_{ext} and OF_{int} are occupancy factor for outdoor (0.2) and indoor (0.8) effective dose and DCF is effective dose to absorbed dose conversion factor of $0.7SvGy^{-1}$ for environmental exposures to gamma-ray.

B. Estimation of Excess Lifetime Cancer Risk (ELCR)

This deals with the probability of developing cancer over a lifetime at a given exposure level. An increase in the ELCR causes a proportionate increase in the rate at which an individual can get cancer of the breast, prostate or even blood. Excess Lifetime cancer risk (ELCR) can be calculated as [8]:

$$\mathbf{ELCR = AEDE \times DL \times RF} \quad (3)$$

where, AEDE is the Annual Effective Dose Equivalent (μSvy^{-1}), DL is the average duration of life (estimated to 70 years) and RF is the Risk Factor (Sv^{-1}), i.e. fatal cancer risk per Sievert. For stochastic effects, ICRP uses RF as 0.05 for public [8].

IV. Results and Discussion

The range of outdoor and indoor gamma ray dose rate has been varied from 0.09-0.14 μSvh^{-1} and 0.08-0.15 μSvh^{-1} with an average value of 0.09±0.005 μSvh^{-1} and 0.12±0.02 μSvh^{-1} in selected eight villages of first zone as shown in table 1.The absorbed dose rate calculated for outdoor andindoor in first zone ranged from 78.3-121.8 $nGyh^{-1}$with an average of 82.03±4.31 $nGyh^{-1}$ and 69.60-130.5 $nGyh^{-1}$ with an average of 100.67±20.72 $nGyh^{-1}$ respectively. Average annual effective dose equivalent for outdoor (100.60±5.28 μSvy^{-1}) and indoor (493.85±101.66 μSvy^{-1}) was lower than ICRP recommended limit 1000μSvy^{-1}[6]. However, the average value of excess lifetime cancer risk ($0.35\times10^{-3}\pm0.02\times10^{-3}$) was found comparable with 0.29×10^{-3} [8]

In second zone, the range of outdoor and indoor gamma ray dose rate has been ranged from 0.12-0.20 μSvh^{-1} with an average of 0.15±0.03 μSvh^{-1} and 0.10-0.17 μSvh^{-1} with an average of 0.14±0.02 μSvh^{-1} in twenty five villages as shown in table 1. The absorbed dose rate calculated in outdoor and indoor in second zone ranged from 104.4-174.0 $nGyh^{-1}$with an average of 131.54±23.64 $nGyh^{-1}$ and 87.0-147.9 $nGyh^{-1}$ with an average of 120.41±18.20 $nGyh^{-1}$. The average value of annual effective dose for outdoor and indoor was found lower than world averages figures [6]. But average excess lifetime cancer risk was found higher than world average figure [8].

In last zone, calculated outdoor and indoor gamma ray dose rate has been varied from 0.21-0.25μSvh^{-1} with an average of 0.22±0.02 μSvh^{-1} and 0.09-0.15 μSvh^{-1} with an average of 0.12±0.02 μSvh^{-1} in seven villages as shown in table 1. The absorbed dose rate calculated in outdoor and indoor in third zone ranged from 182.7-217.5 $nGyh^{-1}$with an average of 191.4±13.95 $nGyh^{-1}$ and 78.3-130.5 $nGyh^{-1}$ with an average of 103.16±14.28 $nGyh^{-1}$. Outdoor and indoor average annual effective dose equivalent was found lower than world averages figures[6].The average excess lifetime cancer risk was $0.82\times10^{-3}\pm0.06\times10^{-3}$and found comparatively higher than0.29×10^{-3} [8].

Moreover, indoor equivalent dose rate was found higher than outdoor

equivalent dose rate due to more accumulation of radionuclides inside the atmosphere as shown in where is Fig. 2. The outdoor radionuclides concentration is far below because the radiation exhaled from the ground is rapidly diffused over the vast atmosphere, but buildings and structures may prevent this dilution and results in accumulation of radionuclides inside the buildings even for areas with low exhalation rates from the ground [7].

Since the values of annual effective dose in all zones were found below the recommended limit, hence it can be concluded that the area is safe for health hazard point of view.

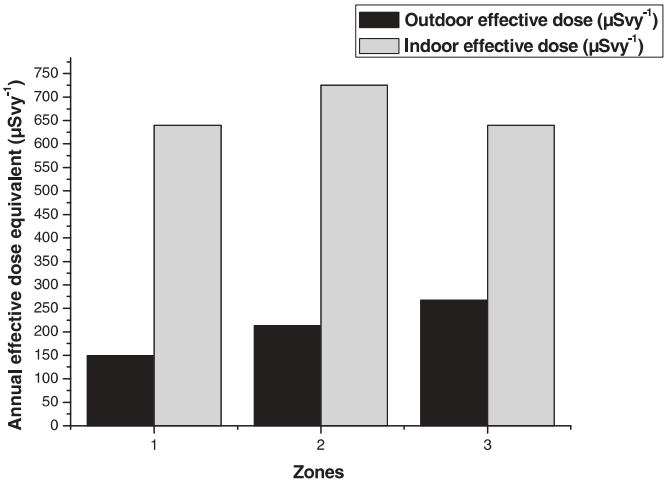

Fig 2. *Variation of outdoor and indoor annual effective dose(μSvy^{-1}) with different type of zones.*

Table 1.Absorbed dose rate and annual effective dose equivalent in indoor and outdoor environment of Jammu district, Jammu & Kashmir, India.

Zones	No. of Villages	Statistical factor	Gamma ray dose rate (μSvh^{-1})		Absorbed dose rate ($nGyh^{-1}$)		Annual effective dose equivalent (μSvy^{-1})		Excess lifetime cancer risk $\times 10^{-3}$
			Indoor	Outdoor	Indoor	outdoor	indoor	outdoor	
Zone 1	8	Min.	0.08	0.09	69.60	78.3	341.43	96.03	0.34
		Max.	0.15	0.14	130.50	121.80	640.18	149.37	0.52
		Mean	0.12	0.09	100.67	82.03	493.85	100.60	0.35
		S.D.	0.02	0.005	20.72	4.31	101.66	5.28	0.02
Zone 2	25	Min.	0.10	0.12	87.00	104.4	426.79	128.04	0.45
		Max.	0.17	0.20	147.9	174.0	725.54	213.39	0.75
		Mean	0.14	0.15	120.41	131.54	590.67	161.33	0.56
		S.D.	0.02	0.03	18.20	23.64	89.26	28.99	0.10
Zone 3	7	Min.	0.09	0.21	78.30	182.70	384.11	224.06	0.78
		Max.	0.15	0.25	130.50	217.50	640.18	266.74	0.93
		Mean	0.12	0.22	103.16	191.40	506.05	234.73	0.82
		S.D.	0.02	0.02	14.28	13.95	70.05	17.11	0.06

V. Acknowledgments

The authors highly acknowledge the financial assistance provided by Board of Research in Nuclear Sciences (BRNS), Mumbai (Project reference No. 2013/36/60-BRNS) for this work.

VI. Refernces

[1]. UNSCEAR 1988 Report to the General Assembly Sources and Effects of Ionizing Radiation (New York: United Nations).

[2]. M. Gholami, S. Mirzaei and A. Jomehzadeh,"Gamma background radiation measurement in Lorestan province, Iran" Iran. J. Radiat. Res.92(2) (2011) 89-93.

[3]. A.A. Sadiq and E.H. Agba, "Indoor and outdoor ambient radiation levels in Keffi, Nigeria"Working and Living Environ. Prot.9(1) (2012)19-26.

[4] N.N. Jibiri and S.T.U. Obarhuna, "Indoor and Outdoor gamma dose rate exposure levels in major commercial Building material distribution outlets and their radiological implications its occupants in Ibaden Nigeria"J. Natural Sci. Res.3(3) (2013)ISSN 2224-3186(paper) ISSN 2225-0921 (online).

[5] K. M. Nagaraju, M. S. Chandrashekar, K. S. Pruthvi Rani and L. Paramesh, "Measurement of gamma natural background radiation in Chamaraja Nagar district, Karnataka state, India" Radiat. Prot. Environ.35 (2013)73-76.

[6] I.U. James, I.F. Moses, J.N. Vandi and U.E. Ikoh, "Measurement of Indoor and Outdoor Background Ionising Radiation Levels of Kwali General Hospital, Abuja" J. Appl. Sci. Environ. Manage.19(1) (2015) 89-93.

[7] G.M. Shilpa, B. N. Anandaram, T.L. Mohankumari, "Study of Environmental gamma radiation level in and around Thirthahalli taluk Karnataka, India" AE Inter. J. Multidisciplinary Res. 2(5) (2014) ISSN - 2348 6724.

[8] H. Taskin, M. Karavus, P.Ay, A. Topuzoglu, S. Hidiroglu, and G. Karahan, "Radionuclide concentration in soil and lifetime cancer risk due to the gamma radioactivity in Kayseri, Turkey" J. Environ. Radioact.100 (2009) 49-53.

Curr. Rep. Sci. & Tech. 2 (1) (2016) 112-120

Thin Film Characterization Based ITO/Crystal Violet/Ag Device for Photovoltaic Applications

Gurpreet Singh[1], Aman Mahajan and R.K. Bedi[2]

[1]Department of Physics, Guru Nanak Dev University College, Narot Jaimal Singh, Pathankot-145026.

[2]Material Science Research Lab, Department of Physics, Guru Nanak Dev University, Amritsar-143005.

gsjosan.phy@gmail.com

Abstract

The present study comprises of structural and optical properties of spin coated crystal violet (CV) films prepared on glass substrates. Film composition was studied by FTIR spectroscopy. Surface morphology of films was studied using Atomic Force Microscopy. Significant results like high absorption coefficient and low band gap are obtained from UV-Visible absorption spectroscopy. Based on these preliminary investigations, an ITO/CV/Ag device was fabricated and studied for photovoltaic characteristics. Various photovoltaic and electrical parameters obtained are reported.

Keywords

Optical, Composition, Morphology, Band Gap, Photovoltaic.

I. Introduction

Thin organic films have revolutionized the research going on in the field of material science. The applications like electroluminescent, [1-2] gas sensors, [3-5] light-emitting diodes, [6-7] and solar cells [8-10] are among the most important aspects of organic thin films. The organic semiconductors used for such applications have a variety of derivatives and many more advantages in terms of a low-cost, a low-temperature process and mechanical flexibility. The performance of devices made from organic materials basically depends upon structural, optical and electrical properties of these materials in thin film form, e.g. development of low cost and efficient organic photovoltaic cells is clearly dependent upon optical

and electrical properties of the material.

Organic dyes form an important class of semiconducting materials with high absorption co-efficient. Metal phthalocyanines and their derivatives are well known in this field.[4] Crystal violet or Gentian violet ($C_{25}H_{30}ClN_3$), a dark violet-green powder is a similar organic material with high optical absorption in the visible region. It is chemically and thermally stable, thus suitable for preparation of thin films.

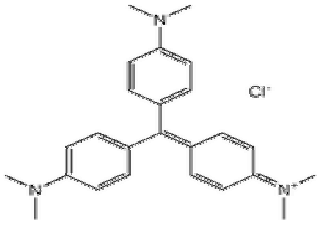

Fig 1. Chemical structure of crystal violet

The very large response towards absorption of light and low band gap (≈2.0 eV in powder form) of crystal violet among organic compounds are the factors which arise a possibility for its photovoltaic applications. Thus there is an extensive research into the applications of crystal violet in Material Science. Crystal violet is studied as a photoconductor in blend layer device[11] and in pallet form.[12] It acts as an n-type dopant for some organic materials such as fullerene (C60) to increase its conductivity.[13] Sensitization with crystal violet dye improves the performance of solar cells.[12]

To use crystal violet in double layer organic thin film solar cells, it is need to be studied in detail for its structural, electrical and optical properties. In our knowledge, no work has been published regarding structural, optical and electrical properties of crystal violet in thin film form grown by spin coating technique. With this communication, we report these properties of spin coated crystal violet films. An ITO/CV/Ag device is fabricated to study photovoltaic, capacitance-frequency and capacitance-voltage characteristics.

II. Experimental

The crystal violet used for this study was obtained from CDH Pvt.

LTD New Delhi. 0.05M solution of crystal violet was prepared in methanol. The spin coating unit of MILMAN series MODEL 2000S was used for uniform deposition of crystal violet films on chemically and ultrasonically cleaned glass substrates at a spinning speed of 2500 RPM. The films so prepared were annealed at 343K. Thickness of the films, as measured by DEKTEK Profilometer, was found to be 250 nm. FTIR (Shimadzu FTIR-8300) technique was used to verify composition of films and to ensure that no decomposition of material takes place while annealing processes. The surface morphological studies are carried out using Atomic Force Microscope (AFM) of "Nanosurf Easyscan2 Switzerland" at room temperature. To study the optical properties, the absorption spectra of the samples are obtained at room temperature in the wavelength range 200-900 nm, using UV-160A (Shimadzu) spectrophotometer.

Based upon the preliminary results obtained, an ITO/CV/Ag device was fabricated by depositing crystal violet on ITO coated glass substrate followed by deposition of silver by using "Hind Hivac 12A4H" vacuum coating unit. Thickness of the Ag layer was monitored by quartz crystal during the deposition and was kept at 75 nm. Thickness of CV layer, as measured by DEKTEK profilometer, was found to be 120 nm. I-V characteristics of this device were studied using Keithley 6517A electrometer under dark and illumination conditions. A 100 Watt halogen lamp was used for illumination of sample and intensity of light was measured using LUX meter. C-V and C-f characteristics are studied using "HIOKI 3522-50" LCR meter.

III. Results and discussion

Fourier transformed infrared (FTIR) spectroscopy is used to identify the crystal violet films. Comparison of FTIR spectra of crystal violet powder and that of thin film shows no practical change in vibrational frequencies (Fig. 2). Also the two spectra resemble very well in finger print region (1500 to 500 cm^{-1}). This indicates that crystal violet did not decompose while annealing up to 343K.

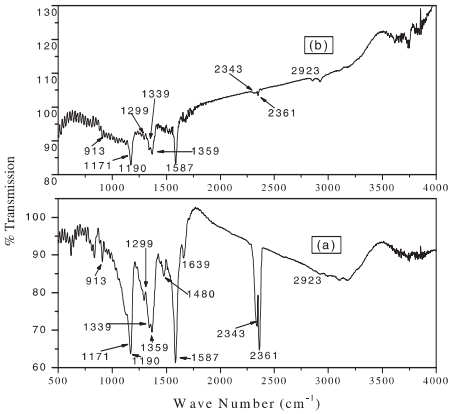

Fig 2. *FTIR transmission spectrum of (a) crystal violet powder and (b) spin coated crystal violet film annealed at 343K.*

It is seen that intensity of transmission peaks corresponding to wave number 2343 cm^{-1} and 2361 cm^{-1} is very low in case of film sample as compared to the corresponding peaks for the powder sample. This may be due to different packing arrangements of crystal violet in powder and thin film form. FTIR transmission peaks at wave number 1587, 1171, 2923 and 1190 cm^{-1}corresponds to C=C stretching of the benzene ring, C-N stretching vibrations, C-H asymmetric stretching and C-O stretching respectively. The transmission peak corresponding to wave number 758 cm^{-1} is attributed to symmetric out of plane bending of the Benzene ring. OH bending and C=C stretching bend are confirmed by the transmission peaks at 1480 cm^{-1} and 1639 cm^{-1}.[14]

The AFM image of crystal violet films indicates uniform growth over the glass substrates (Fig. 3). The surface coverage of film is found to be crack free. Systematically aligned grains of average size 1 μm are observed in the AFM image of film annealed at 343K

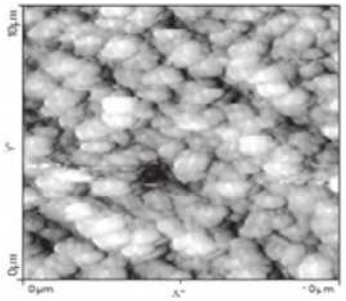

Fig3. *Two dimensional AFM image of spin coated crystal violet film annealed at 343K.*

One of the most important factors commonly used to describe the morphology of surface layer is the root mean square (RMS) roughness parameter. The aligned grains results into smooth thin film with surface roughness 66 nm.

Intense and broad absorption peak is observed in the UV-visible absorption spectroscopy of crystal violet film (Fig. 4a). Absorption in the wavelength range from 470 nm to 730 nm indicates a significant response of crystal violet thin film to light. Maximum absorption is observed at 590 nm.

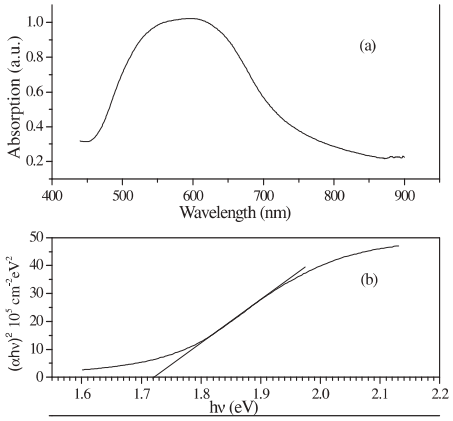

Fig 4. (a) Absorption spectra of spin coated crystal violet film and (b) Determination of band gap from variation of square of absorption co-efficient (α) versus photon energy.

These results indicate a low optical band gap of crystal violet in thin film configuration. To find the optical band gap the absorption edge of the crystal violet film has been examined in terms of a direct transition using Bardeen equation :[15]

$$\alpha h\nu = B(h\nu - E_g)^{1/2} \quad (1)$$

where B is a constant, E_g is the optical band gap and ν is the frequency of incident light.

Figure 4(b) shows the variation of square of the absorption co-efficient (α) versus photon energy (hν) in the energy region (1.5-2.2 eV) for thin films.Optical band gap of film is calculated by extrapolation of straight line to αhν = 0 which is found to be 1.72 eV. It confirms that in thin film configuration crystal violet is among the organic semiconductors having lowest band gap range.

From the above preliminary studies, it is seen that spin coated crystal violet film shows good morphology with least roughness followed by significant optical properties. These are the basic requirements for an organic material to be used as a photoconductor. Keeping this in consideration, a crystal violet based device is fabricated by sandwiching crystal violet layer between ITO coated glass substrate and silver (Ag) electrode to get an ITO/CV/Ag type structure. CV layer was vacuum annealed at 343K before deposition of silver. This device is studied for its J-V characteristics under dark and illumination. Further it is studied for Capacitance-Voltage and capacitance-frequency characteristics.

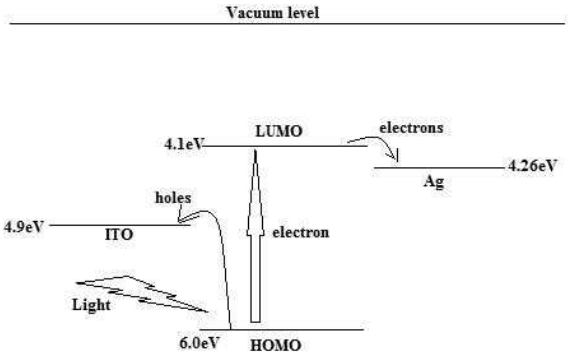

Fig 5. Energy band diagram of ITO/CV/Ag device

Fig. (5) shows the energy band diagram of ITO/CV/Ag device.[10,16] Schottky barrier is formed at ITO/CV interface due to major energy level difference between Fermi level of ITO and LUMO of crystal violet. Ohmic contact is formed at CV/Ag interface due to minor energy level difference between LUMO of crystal violet and Fermi level of Ag. The current density-voltage (J-V) characteristics of ITO/CV/Ag device under illumination and dark conditions are shown in Fig. (6). When negative voltage is applied to the ITO electrode, very small current flows through the device. This is due to the formation of Schottky barrier at the ITO/CV interface. In the low voltage range current carriers do not have sufficient energy to cross this barrier which leads to very small current density in the voltage range from 0.0-0.7 volts. By further increase in voltage current starts increasing as the current carriers now have sufficient energy to cross the schottky barrier. Current increases sharply on further increase in voltage above 0.8 volts. So ITO/CV/Ag device exhibits rectification

behavior with threshold at 0.8 Volts, when negative voltage is applied across the ITO electrode. But when Ag electrode is given the negative polarity, continues flow of charge carriers is observed without any barrier which leads to sharp variation of current with applied voltage. It confirms the formation of ohmic contact at CV/Ag interface.

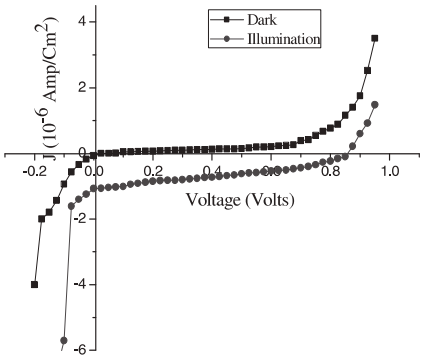

Fig 6.J-V plots of ITO/CV/Ag device under dark and illumination conditions

I-V characteristics of ITO/CV/Ag device are also studied under illumination through ITO electrode using a halogen lamp. Photovoltaic behavior is observed due to formation of a depletion layer of Schottky contact at the CV/ITO interface. Absorption of light photon by crystal violet leads to excitation of electron from HOMO to LUMO level which form an exciton (bounded electron-hole pair). Majority of these excitons recombine, which is a general feature of organic photoconductors. But, some of these excitons get separated by flow of electrons towards Ag electrodes and holes towards ITO. As a result photovoltaic behavior is seen in the J-V characteristic under illumination. The typical photovoltaic parameters are calculated from the analysis of J-V characteristics. Fill factor (FF) and short circuit current density (J_{sc}) for the above device are about 0.45 and 1.11×10^{-6} A/cm^2 respectively. Open circuit voltage (V_{oc}) of 850 mV is much improved than the earlier reported value for photovoltaic device based on crystal violet.[12]

IV. Conclusion

Based on significant results obtained from preliminary characterizations like FTIR spectroscopy, surface morphology and optical

absorption spectroscopy of spin coated crystal violet thin films an ITO/CV/Ag device is fabricated. Formation of Schottky contact at ITO/CV interface and ohmic contact at CV/Ag interface, as indicated by energy band diagram is confirmed by J-V characteristics of this device under dark. J-V characteristics of ITO/CV/Ag device under illumination confirm its photovoltaic behavior. Important photovoltaic parameters like fill factor (0.45), short circuit current density (1.11×10^{-6} A/cm2) and open circuit voltage (850 mV) are calculated. The open circuit voltage for this device is much improved than the previously reported crystal violet based device. So, with intense absorption in visible region and J-V characteristics under illumination we conclude that crystal violet is a very good photoconductor and can be used to improve the efficiency of thin film based organic photovoltaic devices.

V. References

[1] G.N.R. Tripathi, D.R. Dubey and Padmakar, "Electroluminescence in doped anthracene" J. Phys. C:Solid State Phys. 10 (1977) 2015-2017.

[2] G. Hughes and M.R. Bryce, "Electron-transporting materials for organic electroluminescent and electrophosphorescent devices" J. Mater. Chem. 15 (2005) 94-107.

[3] T. Kudo, M. Kimura, K. Hanabusa, H. Shirai and T. Sakaguchi, "Fabrication of Gas Sensors Based on Soluble Phthalocyanines" J. Porphyrins Phthalocyanines 3 (1999) 65-69.

[4] C.G. Claessens, U. Hahn, T. Torres, "Phthalocyanines: From Outstanding Electronic Properties to Emerging Applications" The Chemical Record 8 (2008) 75-97.

[5] R. Saini, A. Mahajan, R.K. Bedi, S. Kumar, "Synthesis and characterization of nanostructured 1,3-bis(1-anthracenylazomethine) benzene films for room temperature NH_3 gas-sensing applications" Sensors and Actuators B147 (2010) 122-127.

[6] S. Schols, S. Verlaak, C. Rolin, D. Cheyns, J. Genoe and P. Heremans, "An Organic Light-Emitting Diode with Field-Effect Electron Transport" Adv. Funct. Mater.18 (2008) 136-144.

[7] J.H. Lee, P.S. Wang, H.D. Park, C.I. Wu, J.J. Kim, "A high performance inverted organic light emitting diode using an electron

transporting material with low energy barrier for electron injection" Organic Electronics12 (2011) 1763-1767.

[8] S. Antohe, "Electrical and photoelectrical properties of the single-, and multi-layer organic photovoltaic cells" Journal of Optoelectronics and Advanced Materials 2 (2000) 498-514.

[9] M. Reinhard,J. Hanisch, Z. Zhang, E. Ahlswede, A. Colsmann and U. Lemmer, "Inverted organic solar cells comprising a solution-processed cesium fluoride interlayer" *Applied Physics Letters*98 (2011) 053303-1 to 053303-3.

[10] D.I. K. Petritsch, "Organic Solar Cell Architectures" PhD Thesis, University of Cambridge, United Kingdom and Technische Universit¨at Graz, Austria (2000).

[11] R. C. Nelson, "Organic Photoconductors. II. Crystal Violet"J. Chern. Phys.22 (1954) 890-892.

[12] G. D. Sharma, A. K. Tripathi, S. C. Mathur and D. C. Dube, "Photovoltaic effect in sensitized crystal violet dyes" J. Mater. Sci. letters 2 (1 9 8 3) 4 3 3 - 4 3 6.

[13] F. Li, A. Werner, M. Pfeiffer and K. Leo, "Leuco Crystal Violet as a Dopant for n-Doping of Organic Thin Films of Fullerene C_{60}"J. Phys. Chem. B108 (2004)17076-17082.

[14] L. Ayed, J. Cheriaa, N. Laadhari, A. Cheref, A. Bakhrouf, "Biodegradation of crystal violet by an isolated Bacillus sp." Annals of Microbiology, 59 (2009) 267-272.

[15] J. Bardeen, F. J. Blatt and L. H. Hall, in Photoconductivity Conference, Atlantic City, 1954, edited by R. G. Breckenridge, B. R. Russell, and E. E. Hahn (Wiley, New York, 1956).

[16] M.V.C. Amares, C. Chenal, R. L. Birke and J.R. Lombardi, "DFT, SERS, and Single-Molecule SERS of Crystal Violet" J. Phys. Chem. C 112 (2008) 20295-20300.

Curr. Rep. Sci. & Tech. 2 (1) (2016) 121-127

Stable Oxygen Isotopes As a Tool to Investigate theTemperature and Salinity Induced Water Mixing

Pooja Devi[1], A.K. Jain[2], M.S. Rao[3] and Rajan Saini[4]
[1]Department of Physics, Guru Nanak Dev University, Amritsar.
[2]Department of Physics, Indian Institute of Technology, Roorkee
[3]National Institute of Hydrology, Roorkee
[4]Post Graduate Department of Physics, Khalsa College, Amritsar
pujaiitr09@gmail.com

Abstract

The temperature and salinity induced mixing process of two water samples with different isotopic signatures was investigated through laboratory based experiment using stable oxygen isotopes of water. The results showed that rate of mixing of water samples having different initial isotopic compositions was slower when only temperature gradient was considered. The presence of salts in either of the water mass makes thermal mixing as well as isotopic mixing rapid. The results are useful in understanding natural hydrological process like mixing of fresh and cold Himalayan rivers with warm and saline sea water.

Keywords

River water, oxygen isotopes, salinity, temperature gradient.

I. Introduction

Mixing is defined as a process leading to the reduction of spatial gradients in water [1]. This can be achieved from motion at a microscopic scale governed by molecular diffusion, as well as advection and turbulence phenomena on macroscopic level. It may be noted that dissolved salt exists in water in its ionic form (NaCl). Therefore the movement of salt ion is associated with movement of water molecule. In this case, the higher temperature water is lighter (low density) compared to colder water and this relation is used to see the salinity and temperature mixing. The differences arising in water density due to

change in temperature and/or salt concentration are highly significant for the pattern of vertical mixing in lakes. Fresh water is light and floats on the surface, while salty water is heavy and sinks. The salinity and temperature together determine buoyancy of water. When surface salinity increases due to evaporation, the increased surface density contributes to a destabilization of upper-ocean stratification. Though the total buoyancy flux also depends on the sign and magnitude of the heat flux, surface "salinification" will generally contribute to deeper convective mixing of surface waters. Conversely, freshwater inputs due to rainfall or river runoff will decrease surface salinity, make a positive contribution to the stratification, and generally inhibit mixing. By observing states and changes of the concentrations of ocean salinity, it is possible to learn about ocean circulation, the water cycle, and climate change. For instance, the Arabian Sea has high salinity (usually in the range 35 to 37 psu) due to excess of evaporation over rainfall. In contrast, the Bay of Bengal has much lower salinity due to the large influx of fresh water from river discharge and high amount of rainfall. A constant addition of fresh water from the surrounding rivers essentially affects chemical and physical properties (temperature, isotopic composition) throughout the year.

Although, many natural examples of mixing of freshwater and saline sea water are well known globally [2-6] but micro details of the phenomenon of mixing is still not well understood due to various complex processes involved that affect the rate of mixing. To monitor the mixing of water masses using isotopes, it is also required to have isotopic inhomogeneity of the water masses. Combined study of stable ^{18}O isotopes and salinity can be ideal to monitor various processes happening in the oceans. In this paper, through laboratory based experiment, an attempt has been made to track the mixing process by monitoring temperature, salinity and ^{18}O content of mixing water samples with the assumptions that ^{18}O is controlled due to dispersion of isotopes along the gradient; salinity change additionally is governed by dispersion and diffusion process while thermal process, in addition to these is controlled by physical movement of molecules and energy transfer mechanism.

II. Materials and Methods

The two water samples taken from Roorkee town for the experiments were: Ganga Canal Water (CW) and Ground Water (GW) with isotopic compositions −8.70‰ and +13.04‰ respectively. The natural salinity of CW was 0.28mS/cm and that of the GW was reduced to 0mS/cm by distillation. The temperature gradient between the two water samples kept at the beginning of the experiment was 61ºC in both the experiments. This temperature gradient was achieved by heating the one water sample to ~64ºC while cooling the other water sample to ~3ºC by keeping it in the refrigerator. The mixing of warm and cold water was carried out in a translucent measuring cylinder of capacity 1.5L. To avoid surface cooling, evaporation induced isotopic changes and interaction between atmospheric vapour and experimental water, the measuring cylinder was covered from top with the help of a thick polythene sheet.

A. Temperature Induced Mixing

In a measuring cylinder 500ml of cold GW (~3ºC) was taken. There after an equal volume of warm CW (~64ºC) was added onto the cold water from the top very very slowly. Temperature measurements were done by using three pre-calibrated temperature probes at water depth of 100ml, 500ml (interface of two water masses) and 900ml (bottom layer) from the top surface of water in the measuring cylinder. At designed intervals, the 2.5ml aliquots of water samples were collected from three depths where temperature measurements were taken with the help of glass pipette in HDPE bottles of capacity 3 ml. Samples were taken very carefully so as to avoid any undesired turbulence in the water column till the temperature equilibrium between the two water samples was achieved.

B. SalinityInduced Mixing

The above experiment was repeated by raising the salinity of CW to 57 mS/cm (measured at room temperature) by dissolving 24gm of NaCl salt in 1L of hot CW. Electrical Conductivity (EC) measurements were also taken along the temperature monitoring and samples collection at designed intervals as discussed earlier. For measurements of electrical conductivity (EC) of saline water samples, 1ml of the sample water was diluted 100 times with distilled water (EC=0mS/cm) and the measurements were done with the help of hand held EC meter. The

purpose to prepare the saline water was to see the mixing of sea water with fresh water. Both the experiments were conducted at room temperature. The samples collected in both the experiments were stored in refrigerator till they are taken for isotopic analysis to investigate molecular level mixing.

C. Oxygen Isotope Analysis of Samples

The oxygen isotopic analysis of collected water samples were analyzed on Continuous flow- Isotope Ratio Mass Spectrometer (CF-IRMS) at Nuclear Hydrology laboratory of National Institute of Hydrology, Roorkee, India. The isotopic analysis was done by standard equilibration method in which water samples are equilibrated with CO_2 [7-8]. The results were expressed as:

$$\delta_{sample} = [(R_{sample}/R_{V\text{-}SMOW}) \ \ 1] \times 1000 \text{ ‰}$$

where $R = {}^{18}O/{}^{16}O$ in sample or in Vienna Standard Mean Ocean Water (V-SMOW). The reproducibility for ^{18}O is ±0.1‰.

III. Results and Discussion

A. Analysis of Thermally Induced Water Mixing

In 8 hours long experiment, the net fall in temperature of top layer was 39°C and rise in temperature of bottom layer was 22.2°C (Fig. 1a). The equilibrium temperature attained was 25°C which is same as the average room temperature 25.3°C in a duration of 280 min. The equilibrium isotopic composition $\delta^{18}O = 2.49$ ‰ was achieved in duration of 320 min which is in agreement with the $\delta^{18}O_{final\ average} = 2.56$ ‰ (Fig. 1b).

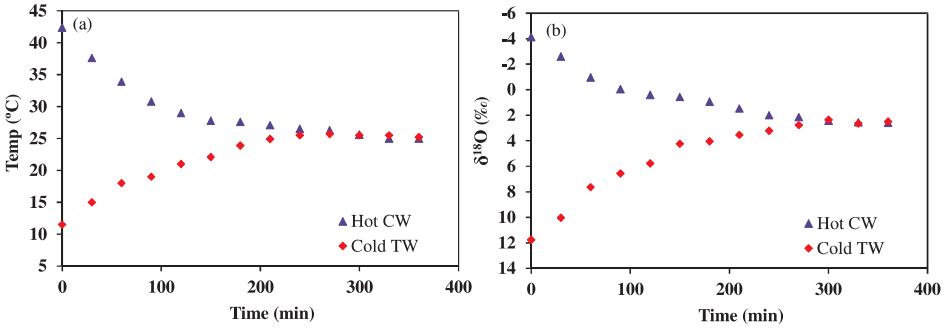

Fig1. *Time Variations of (a) temperature and (b) $\delta^{18}O$ in temperature induced mixing of two water samples.*

It is evident that the temperature mixing takes place faster than the complete isotopic mixing of two water masses of different isotopic signatures. This can be due to the reason that hot canal water is depleted and is on the top of the enriched ground cold water, so the GW will try to remain at the bottom and CW will tend to float at the top for longer time, which may slow down the process of isotope mixing than temperature mixing.

B. Analysis of Salinity Induced Water Mixing

It was observed that after mixing hot saline CW to the fresh cold GW, the equilibrium temperature and isotopic compositions of two water masses become homogeneous with values 27.4°C and + 2.51‰ respectively (Fig. 2). This clearly indicates that the solute accelerates the mixing process and the energy transfers through solute as well as solvent (water). The dual mode of energy transfer brings the concentration and temperature of the two solutions to equilibrium value immediately. Therefore the isotopic exchange of water molecules is also very rapid.

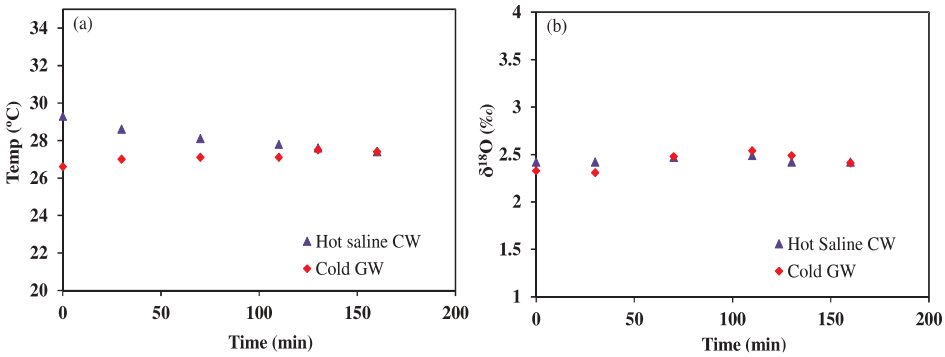

Fig2. *Variations of (a) temperature and (b) $\delta^{18}O$ in salinity induced water mixing of two layered system.*

C. Comparison of Mixing Pattern Among The Two Experimental Situations

The mixing least-square regression equations fitted to the measured temperature and ^{18}O data of both experiments are shown in Fig. 3 The fresh water and saline water show similar correlation (negative) for temperature mixing (R^2>0.86) indicating that the temperature of the bottom cold water changes slower than the temperature of surface warm water (Table 1). However, correlation coefficient found for the ^{18}O mixing in first case was excellent (R^2 = 0.981) when salt was not added to the any of the

water mass. This infers that the isotopic composition of the bottom enriched water changes faster than the surface depleted water. However, with the addition of salt to the hot depleted canal water, the value of correlation coefficient was reduced to 0.523. Overall, it can be inferred that mixing of enriched and depleted water in terms of both temperature and isotopic composition is affected by the salinity of the water.

Table 1. *The temperature and ^{18}O relation between GW and CW for Experiment 1 & 2.*

Parameter	Experiment 1	Experiment 2
Temperature	$T_{GW} = -0.849*T_{CW} + 46.843$; ($R^2 = 0.958$, N = 13)	$T_{GW} = -0.423*T_{SCW} + 39.019$; ($R^2 = 0.885$, N = 6)
$\delta^{18}O$	$\delta^{18}O_{GW} = -1.450*\delta^{18}O_{CW} + 5.986$ ($R^2 = 0.981$)	$\delta^{18}O_{GW} = 2.120*\delta^{18}O_{SCW} - 2.746$ ($R^2 = 0.523$)

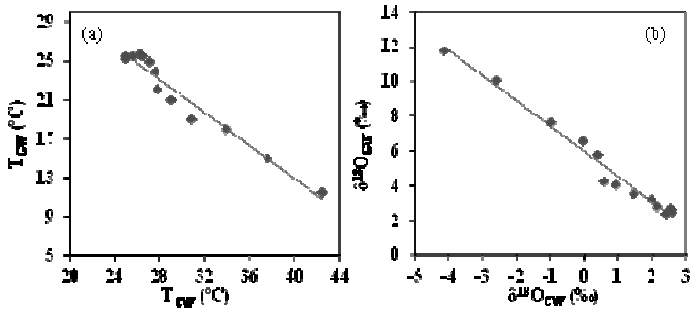

Fig 3.*(a) Top-bottom temperature and (b) $\delta^{18}O$ mixing relation for enriched ground water and depleted fresh canal water.*

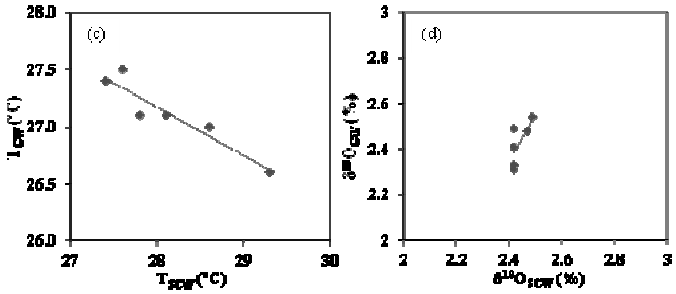

Fig 3.*(c) Top-bottom temperature and (d) $\delta^{18}O$ mixing relation for saline enriched ground water and depleted saline canal water.*

IV. Conclusion

When salinity difference was not considered, thermal mixing was faster than isotopic mixing. The presence of salts in either of the water mass

makes the rate of thermal mixing as well as isotopic mixing rapid. Higher the temperature or salinity gradient more is the rate of mixing. Combined study of stable hydrogen (δ^2H) and oxygen ($\delta^{18}O$) isotopes and salinity can be ideal to monitor various processes happening in the oceans. Therefore, such kind of studies can be extended to monitor the natural systems.

V. Acknowledgments

Pooja Devi acknowledges the support and facilities provided by Hydrological Investigation Division of National Institute of Hydrology, Roorkee, India for this work.

VI. References

[1] D. Imboden and A. Wuest, Mixing Mechanisms in Lakes, Springer (1995), 81-138.

[2] J.R. Dyer, "Groundwater-surface water interactions: effects of geothermal spring inputs to Jemez river water quality," 2007. Appl. Phys. Letters 85 (2004) 2503-2504.

[3] P. N. Vinayachandran and J. Kurian, "Modeling Indian ocean circulation: Bay of Bengal fresh water plume and the Arabian Sea mini warm pool. in: modeling, Proc. 12th Asian Cong. on fluid mechanics, Daejeon, Korea,"

[4] H. F. Haung and C. F. You, "Tracing freshwater plume migration in the estuary after a typhoon event using Sr isotopic ratios," Geophys. Res. Letters 34 (2007).

[5] F.L. Hellwger and L. G. Amold, "Tracing Amazon River water into the Caribbean Sea," J. of Marine Res.60 (2002) 537-549.

[6] J. Yuan, L. M. Richard, T.P. Rondey and J. D. Michael, "Storm induced injection of the Mississippi river plume into the open gulf of Mexico," Geophy. Res. Letters 31 (2004) L09312.

[7] S. Epstein and T. Mayeda, "Variations of the $18_O/16_O$ ratio in natural waters," Geochimicaet Cosmochimica Acta 4 (1953) 213-224.

[8] C.A.M. Brenninkmeijer and P.D. Morrison, "An automated system for isotopic equilibration of CO_2 and H_2O for ^{18}O analysis of water," Chem. Geol. 66 (1987) 21-26.

Curr. Rep. Sci. & Tech. 2 (1) (2016) 128-134

Preparation and Characterization of Self-Assembled Organic Nanofibers

Rajan Saini[1], Pooja Devi[2], Rummi Devi Saini[3] Iqbal Singh[1], Kamalpreet Khun Khun[1], Gursharan Kaur[1], Taminder Singh[1] and R.K. Bedi[2]
[1]Post Graduate Department of Physics, Khalsa College Amritsar-143005
[2]Department of Physics,
Guru Nanak Dev University, Amritsar-143005
[3]SMDRSD College, Pathankot. sainifizix@gmail.com

Abstract

Self-assembled nanofibers of $CuPcOC_8$ have been grown onto glass substrate using drop cast method under different experimental conditions and subsequently characterized for their structural, electrical and optical properties using X-ray diffraction, atomic force microscopy, UV-Visible spectroscopy and two probe technique. The results revealed that the density and dimensions of nanostructures was found to be strongly dependent on the concentration of solution. The possible formation mechanism of these structures was π-π interaction between phthalocyanine molecules.

Keywords

Phthalocyanine, Atomic force microscope, self-assembly, nanofibers.

I. Introduction

Cost effective preparation of nano/microstructures with controllable dimensions has attracted much attention in the field of molecular electronics as the small dimensions of these structures have significant effects on device performance due to high molecular ordering of nano/microstructures [1]. However, most 1D nano/micro structures reported in the literature belong to metals and inorganic materials [2]. Apart from these, organic materials are also popular among scientific and industrial world due to their wide use in thin film based devices such as field-effect transistors, light emitting diodes, and photovoltaic cells [3]. Organic semiconductors like phthalocyanines provide many advantages over the inorganic counterparts, such as unlimited choices of molecular

structures for property optimization, high flexibility and low cost of materials fabrication, ease for large area processing and compatibility with flexible and lightweight plastic substrates, and thus may open broader applications for the next generation of electronic devices [4]. In recent years, nano/micro structures have been grown by template method, vacuum evaporation, electrophoretic deposition etc. But solution based self-assembly is the simplest way to grow such structures [5]. In this method, we can synthesize self-assembled nano/micro structures by casting a solution onto the wide area substrates. However, poor solubility of unsubstituted phthalocyanine (Pc) complexes in common organic solvents highly restricts their applications in the solution process able organic semiconductors [6]. In order to induce solubility in a particular solvent, substitution of the phthalocyanine (Pc) microcycle is necessary. It is well known that incorporating substituents onto the phthalocyanine ring is able to tune the physical-chemical, electrochemical, and spectroscopic properties of phthalocyanine derivatives. In addition to the improved process ability, MPc complexes with high solubility can provide more efficient approaches to fabricate highly ordered structures and morphologies, which have gained considerable interest in recent years mainly due to their promising applications in optical and electronic organic devices [7].

In the present paper, we have selected Cu(II) 2,3,9,10,16,17,23,24-octakis (octyloxy)-29H, 31H-phthalocyanine i.e. ($CuPcOC_8$) molecule with eight short chain and flexible butoxy groups conferring good solubility of the molecule in various organic solvents and is also responsible for intramolecular π-π stacking to produce self-assembled nanostructures. The nanostructures are fabricated by drop casting $CuPcOC_8$/DMF solution onto the glass substrate. The self-assembled structures so obtained have been characterized for their structural, electrical and optical properties.

I. Experimental

$CuPcOC_8$ (figure 1) powder has been procured from Sigma Aldrich Pvt. Ltd. India Glass substrates were washed with lab detergent solution and deionized water in order to remove dust particles. After this, substrates

were ultrasonically and chemically cleaned with acetone, methanol and ultrapure water. The substrates were dried and kept in desiccator for further use. The concentration of $CuPcOC_8$/DMF solution was approximately 10^{-3} M. The samples were prepared by depositing a droplet of the solution on the substrates in a closed environment. After the solvent was evaporated, the atomic force microscope measurements were performed with a Nanosurf (model- Easy Scan 2), Switzerland AFM system with a Si tip having a force constant of 48 N/m. To check the lateral uniformity, different images were recorded at different positions of the sample. The images were analysed and processed using the standard software supplied with the control electronics. Film structure was examined using a Bruker X-ray diffractrometer using CuK_α radiation (λ=1.5418 Å) within a range of 3°-45° in 2θ scan mode. The X-ray tube was operated at current of 30 mA and 40 kV voltage. To study the optical properties, the absorbance spectra of the samples were obtained in the wavelength range of 300 to 900 nm by using UV-1601PC (Shimadzu, Japan) spectrophotometer. All structural and optical measurements were performed at room temperature (25 °C). To study the I-V characteristics, droplet of solution was poured on the substrate with pre-deposited gold electrodes and measured by using computer interfaced Keithley electrometer (6517A).

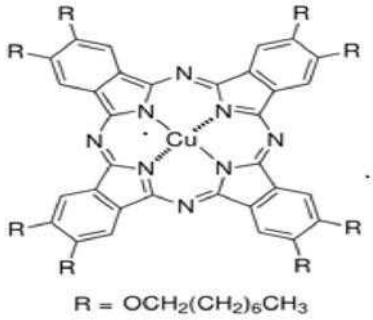

Fig. 1 Chemical structure of $CuPcOC_8$ molecule.

III. Results And Discussion

Figure 2 represents the two and three dimensional AFM images (scan size 5μm × 5μm) of self-assembled nanofibers grown parallel to the glass substrate. As seen in the figure, nanofibers were grown with smooth and dense morphology whose size distribution is uniform over the substrate

surface. The average diameter of nanofiber was found to be 83 nm. The rms roughness of nanofibers sample was found to be 4.8 nm. Fig. 3 represents the XRD diffractogram of nanofibers sample with a diffraction peak at 3.6° corresponding to an intermolecular separation of 2.52 nm between the adjacent phthalocyanine molecules. Besides this, a broad diffraction band between 10° to 20° has also been observed which may be due to the reflection from glass substrate.

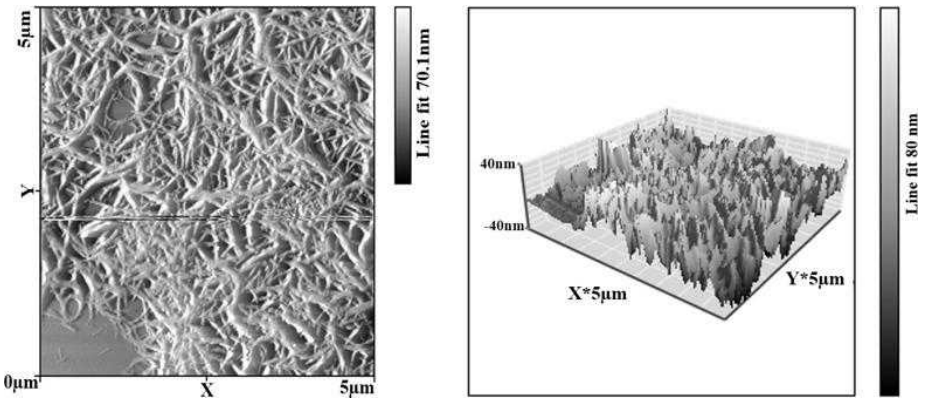

Fig. 2. *Two and Three dimensional AFM images of CuPcOC8 nanofibers grown over glass substrate*

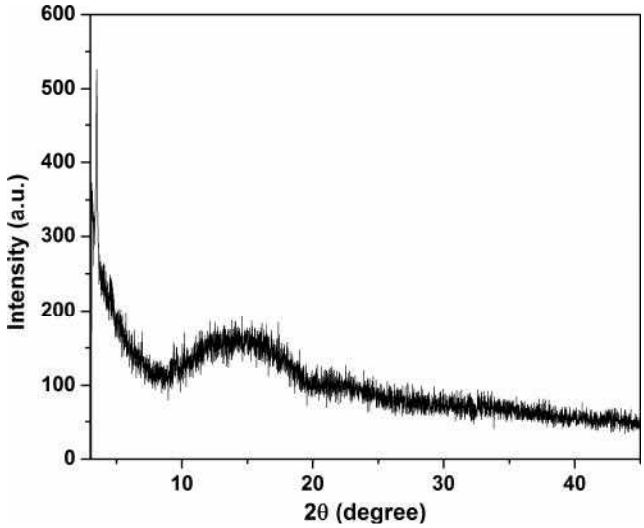

Fig. 2. *X-ray diffraction pattern of CuPcOC8 nanofibers grown over glass substrate.*

The optical properties of $CuPcOC_8$nanofibers have been studied by using UV-visible absorption spectroscopy technique in the wavelength range 300-900 nm. The UV-visible spectrum of phthalocyanines is due to π-π* transitions between molecular orbitals within the aromatic 18-π electron system and from overlapping orbitals on central metal ion [6]. The absorption bands observed in high energy (250-500 nm) and low energy region (550-800 nm) are called B band (Soret band) and Q-bands respectively. The higher energy "B-band" (250-500 nm) originates from highest occupied molecular orbital (HOMO) a_{2u} to lowest unoccupied molecular orbital (LUMO) e_g transition while the lower energy "Q-band" (550-800 nm) is ascribed to transition from HOMO a_{1u} to LUMO $e_g$level [6]. The UV-visible absorption spectrum of nanofibers sample is shown in figure 4. As shown in figure 4, UV-visible absorption spectrum of nanofibers sample depicts B band in UV region at 341 nm and Q band doublets in the visible region at 609 and 661nm respectively. The absorption bands of phthalocyanine films are generally found to be broadened as compared to the solution forms which may be attributed to formation of aggregates due to interaction between molecules in films [6]. The Q bands of nanofibers sample were found to be red shifted as compared to that of $CuPcOC_8$/DMF solution which reflects the edge-on type interactions between the phthalocyanine molecules in nanofibers sample [6].

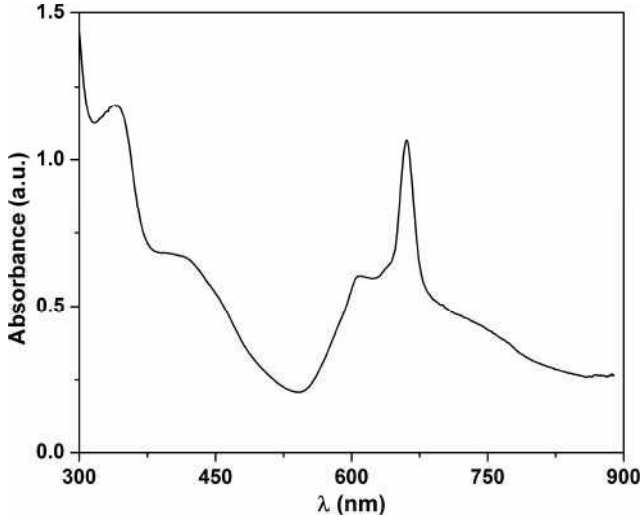

Fig. 4*. UV-Visible absorption spectrum of $CuPcOC_8$ nanofibers.*

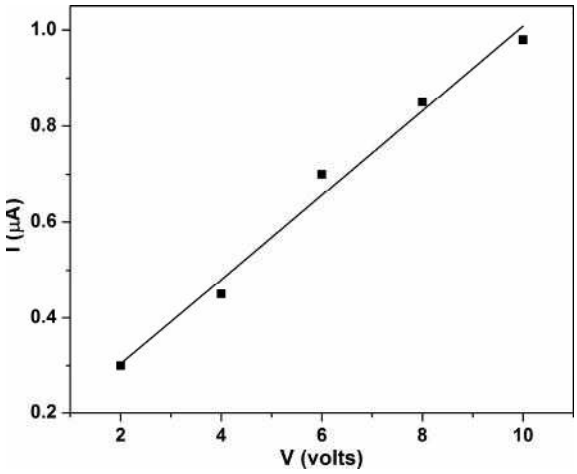

Fig. 5*. I-V characteristics of $CuPcOC_8$ nanofibers.*

To study the I-V characteristics of nanofibers, a droplet of $CuPcOC_8$ solution was drop casted between two pre-deposited Au electrodes. As shown in figure 5, the d.c. current was to found to increase monotonically with the increase in applied voltage. The d.c. current was found to be near 1μA at a bias voltage of 10V. This improved conduction might be due to the π-π stacking which favours the conductivity through co-facial intermolecular π-delocalization showing the potential of these nonofilters device applications.

IV. References

[1] F. S. Kim, G. Ren and S. A. Jenekhe, "One-dimensional nanostructures of conjugatedmolecular systems: assembly, properties, and applications from photovoltaics, sensors, nanophotonics to nanoelectronics" Chem. Mater.23 (2011) 682-732

[2] G.J. Cadena, J. Riu and F.X. Rius, "Gas sensors based on nanostructured materials" The Analyst132 (2007) 1083-1099.

[3] C. Zhang, Y. Yan, Y.S. Zhao and J. Yao, "Synthesis and applications of organic nanorods, nanowires and nanotubes"Annu. Rep. Prog. Chem., Sect C: Phys.Chem.109(2013) 211-239.

[4] L. Zang, Y. Che and J.S. Moore, "One-dimensional self-assembly of planar-conjugated molecules: adaptable building blocks for organic nanodevices"Acc.Chem. Res.41 (2008) 1596-1608.

[5] Rajan Saini, A. Mahajan, R.K. Bedi, D.K. Aswal and A.K. Debnath,

"Phthalocyanine based nanowires and nanoflowers as highly sensitive roomtemperature Cl_2 sensors" RSC Advances 4 (2014) 15945-15951.

[6] Rajan Saini, A. Mahajan, R.K. Bedi, D.K. Aswal and A.K. Debnath, "Solution processed films and nanobelts of substituted zinc phthalocyanine as room temperatureppb level Cl_2 sensors" Sensors and Actuators B198 (2014) 164-172.

[7] Gema de la Torre, C.G. Claessens and T. Torres, "Phthalocyanines: old dyes, new materials. Putting color in nanotechnology" Chem. Comm.(2007) 2000-2015.

Curr. Rep. Sci. & Tech. 2 (1) (2016) 135-144

Room Temperature Toluene Sensing Characteristics of Ultrasonically Deposited Zn-doped CuO Nanostructures

Gursharan Kaur, Taminder Singh, Iqbal Singh, Kamalpreet Khun Khun and Rajan Saini
PG Department of Physics, Khalsa College, Amritsar, India,
iqbalsgh@yahoo.com

Abstract

The large-scale Zn doped CuO nanostructures were deposited by ultrasonic spray pyrolysis route on the corning glass at different substrate temperature. The films with doping concentration of 5% and 10 % were deposited. The asdeposited films without any treatment were tested for toluene sensing at room temperature. The results indicate that the response of the CuO nanostructures towards toluene was affected significantly by substrate temperature and by Zn doping. It is found that the 10% Zn-doped CuO films deposited at substrate temperature of 300^0 C exhibits remarkably enhanced response of 85.03%.

Keywords

Toluene sensor, room temperature, CuO

I. Introduction

Toluene belongs to a family of an aromatic hydrocarbon compound and due to its intoxicating properties it leads to severe neurological problems on exposure to a very low concentration of Toluene [1-3]. Toluene has been extensively used in industrial reactions as feedstock and as solvent [4-6]. This family of volatile organic compounds (VOC) degrade the environment and thus its control is not only important from the point of public health care, but it is also very important for public security. It is therefore important to develop the instruments possessing ability to work in rough atmosphere and sensing such VOC at room temperature.

Sensors are the devices which efficiently work to monitor number of toxic volatile organic compounds and the use of semiconductor metal

oxide (transition) in the thick/thin film as toxic gas sensors has been reported in literature [7]. In recent years the synthesis of nanostructured metal oxide such as CuO, ZnO, SnO_2, WO_3 enhances the sensitivity to various gases including VOC because of the incorporation of increased specific surface area by synthesizing the material in various forms of nanostructures [8-11]. Metal oxide gas sensors change the electrical conductivity when VOC are adsorbed on metal oxide surface, so it is possible to detect the compounds by measuring the electrical resistance of the sensors. This technology presents the advantages of its low cost, small size and microelectronic compatibility. It has been found in number of reports that high operating temperature is mandatory for efficient sensor operation which increases the power consumption. It also decreases the suitability and reliability of the sensor performance. Thus, room temperature operated sensors are being preferred as their performance is repeatable and significant. However, most of metal oxide semiconductors gas sensors found in literature focus on detecting traces concentration of various oxidizing and reducing gases including H_2, CO, H_2S, C_3H_8, C_2H_5OH, CH_2O, and NO_x [12-18]. We have previously reported the detection of ammonia at room temperature using thick and thin film of CuO based sensors [19-21].

The number of materials pure as well as doped such as C-doped WO_3, Au-ZnO, ZnO-SnO_2, SnO_2, TiO_2-doped ZnO have been successfully utilized for the detection of toluene [22-26]. In literature very few reports on the sensors working at room temperature used for the detection of aromatic compounds have been found [26-27].

In the present investigation, Zn doped CuO films were deposited by ultrasonic spray pyrolysis (USP) technique and investigated its application in detecting toluene vapor. The as-deposited films without any further treatment as gas sensor exhibits desirable sensing characteristics including good sensitivity and reproducibility at room temperature.

II. Experimental Procedure

The films of CuO were deposited onto glass substrates by using 0.2M aqueous solution of trihydrated cupric nitrate ($Cu(NO_3)_2.3H_2O$). To introduce the doping ion in precursor, 0.2 M aqueous solution of $Zn(NO_3)_2$ was prepared and 5 and 10 ml of solution was added to aqueous cupric

nitrate solution to have required doping amount. The resulting solution has been stirred vigorously for 4 hours to form a homogeneous sol. The solution so prepared was used to generate an aerosol using an ultrasonic nebulizer (Omron Make NE-U17) which was subsequently transferred on the ultrasonically cleaned, preheated corning glass substrate using air as carrier gas. The preparative parameters of the USP set up such as nozzle to substrate distance, solution concentration, solution spray rate were taken from our previous reports on USP deposition [28, 29] to obtain pin hole free and adherent films. The substrate temperature was varied from 300^0 to 400˚C ± 5˚C using thermo controller (DTC Selec 303). After deposition the films were allowed to cool down naturally to room temperature. The film samples deposited at substrate temperature of 300˚ and 400˚C with doping concentration of 5% and10% are coded as 5ZC1, 10ZC1 and 5ZC2, 10ZC2 respectively.

The doped samples have been characterized for its phase analysis by X-ray diffraction analysis on PAN-analytical using Cu Kα wave. The surface morphological and composition analysis of the Zn doped CuO films were done using field emission scanning electron micrographs (FESEM), EDAX spectrum taken on a JEOL JSM-6700F with a beam voltage of 30 KV.

The response of Zn-CuO films for toluene was measured using two probe set up by measuring the change in the resistance of the films in toluene environment with respect to room temperature.The film resistance was measured with Keysight 34410A multimeter. Gas response is defined as the ratio of change in the resistance of the sample on exposure to gas with respect to the resistance in air.

$$S = \frac{|R_g - R_a|}{R_a} \quad (1)$$

Where R_g and R_a are the film resistance, measured in gas and air atmosphere respectively.

III. Results and discussion

Fig 1. shows XRD diffractogram of the Zn doped CuO films deposited onto the glass substrate kept at temperature of 300˚C with deposition time of 30 minutes. The obtained XRD diffractogram of the film shows sharp peaks indicating polycrystalline nature of samples and shows the characteristic peaks corresponding to CuO phase. It has been observed in

the diffractogram that no peak corresponding to the Zn or ZnO phase appeared on the XRD pattern. A matching of the observed and the standard (*hkl*) planes confirms that the deposited films are polycrystalline having monoclinic CuO. The diffractogram shows the prominent (002) and (111) monoclinic CuO peaks. The positions and the *d* values of the diffraction peaks for CuO are in good agreement with those reported earlier for the spray deposited CuO thin films [29, 30].

FESEM images displaying surface morphology of Zn doped CuO films have been shown in Fig. 2. The images clearly depict the change in surface morphology with change in doping concentration and substrate temperature. The micrographs of samples reveal uniform distribution of faceted like spherically shaped grains. The surface texture of deposited films is smooth and crack free composed of nano-sized particle agglomerates. The particle size in agglomerates is much smaller than the grain size and is difficult to resolve. The images of 5ZC1 and 5ZC2 found to possess bunches of particles having symmetrical shape but the grain size increases with the rise in substrate temperature. It has been observed from the morphological analysis of the doped samples that the size of grains has been significantly decreased with increasing dopant concentration. The sensing characteristics of USP deposited 5% and 10 % Zn doped CuO thin films are shown in Fig. 3 and Fig. 4 respectively. Observations show that resistance of films starts decreasing with the introduction of toluene in test chamber and attains saturated value after some time. The 10ZC1 films exhibits highest response of 6.683 and sensitivity of 85.03%, whereas 5ZC1 film show comparatively poor response of 1.091 and sensitivity of 8.36%. Thus, response and sensitivity of CuO films rises drastically with the increase in Zn concentration. The effect of dopant on gas sensing properties of films can be explained on the basis of modification induced by dopant in terms of increasing catalytic sites for gas adsorption [31]. Further 10ZC1 films were tested for their response characteristics to other VOC at room temperature. The response of various film samples toward toulene is shown in the Fig. 5.

A decrease in surface resistance of the film with the introduction of VOC may be assigned to their redox reaction with the adsorbed oxygen species O_2^- available at the active catalytic sites created by dopant and metal deficit

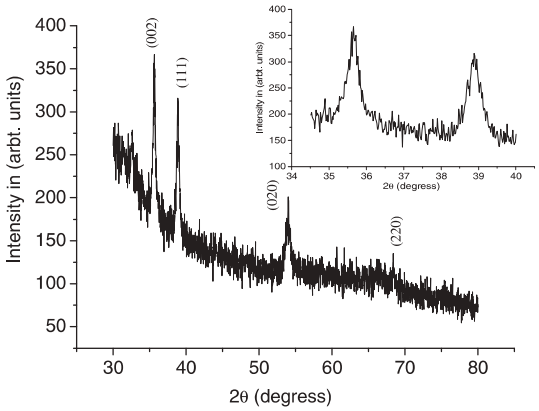

Fig.1 XRD diffractogram of the 10ZC2 sample

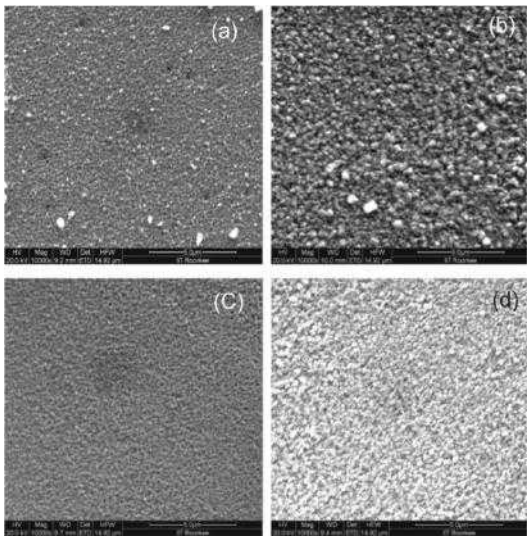

Fig. 2 *FESEM images of the (a) 5ZC1, (b) 5ZC2, (c) 10ZC1 and 10ZC2 samples*

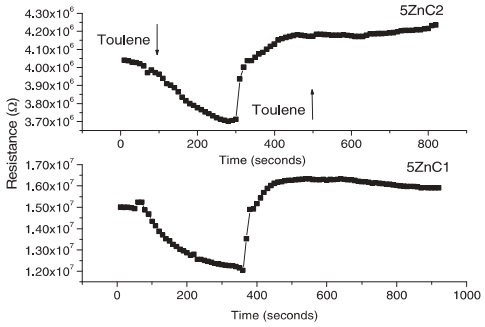

Fig. 3 *Variation in the resistance of the 5% Zn doped samples towards Toluene vapors at room temperature.*

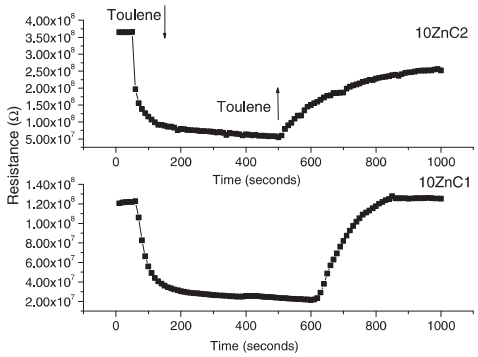

Fig. 4 *Variation in the resistance of the 10% Zn doped samples towards Toluene vapors at room temperature*

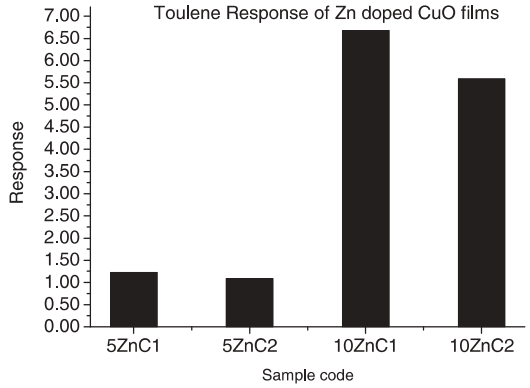

Fig. 5 *Response of various samples toward Toulene at room temperature*

locations. The response of the film decreases with increase in substrate temperature from 300 to 400˚C which might be due to the decrease in surface defects [29-33].

It can be seen from Fig. 3 and 4 that CuO film sensors have good sensing performance, with high sensitivity and a short response time. The highest response of 6.683 has been found for the films deposited at substrate temperature of 300˚C and with 10% doping concentration (10ZC1). The response characteristics show that sensor recovers its original resistance in minimum time when toluene has been ejected out.

IV. Conclusions

Sensitive film samples of cuo doped with zinc oxide have been

fabricated using the Spray pyrolysis method. The fabricated sensors 10ZC1 have a response as high as 6.683 and sensitivity of 85.03% ppm of 6oulene. Hence the films exhibited exceptional gas sensing characteristics at susbrate temperature of 300^0. Such a high selectivity and sensitivity of 10ZC1 film can be used in a practical gas sensing system to measure toluene for environmental monitoring, particularly at room temperature. The fast response and recovery time of films implies that toulene vapour molecules must interact weakly and reversibly with doped CuO films.

V. References

[1] R. van Doorn, C. Leijdekkers, R. Bos, R. Brouns, P. Henderson, Alcohol and sulphate intermediates in the metabolism of toluene and xylenes to mercapturic acids, J. Appl. Toxicol. 1 (1981) 236242.

[2] M. Matsuguchi, T. Uno, T. Aoki, M. Yoshida, Chemically modified copolymer coatings formass-sensitive toluene vapor sensors, Sens. Actuators B 131 (2008) 652659

[3] H. Z. Streicher, P. A. Gabow, A. H. Moss, D. Kono, and W. D. Kaehny, Syndromes of Toluene Sniffing in Adults. Annals of Internal Medicine, 94 (1981) 758-762.

[4] G. Devathasan, D. Low, P. C. Teoh, S. H. Wan, and P. K. Wong, Complications of Chronic Glue (Toluene) Abuse in Adolescents. Australian & New Zealand Journal of Medicine, 14, (1984) 39-43.

[5] L. Molhave, G. Clausen, B. Berglund, J. De Ceaurriz, A. Kettrup, T. Lindvall, M. Maroni, A.C. Pickering, U. Risse, H. Rothweiler, B. Seifert and M. Younes, Total Volatile Organic Compounds (TVOC) in Indoor Air QualityInvestigations. Indoor Air, 7 (1997) 225-240.

[6] A. J.Hempel, K. S. Kjaergaard, L. Molhave, and H. K. Hundnell, Sensory Eye Irritation in Humans Exposed toMixture of Volatile Organic Compounds. Archives of Environmental Health, 54 (1999) 416-424.

[7] H. Z. Streicher, P. A. Gabow, A. H. Moss, D. Kono and W. D. Kaehny Syndromes of Toluene Sniffing in Adults. Annals of Internal Medicine, 94 (1981) 758-762.

[8] Q. Geng, X. Lin, R. Si, X. Chen, W. Dai, X. Fu and X. Wang, The Correlation between the Ethylene Response and Its Oxidation over TiO2 under UV Irradiation. Sensors and Actuators B, 174 (2012) 449-457.

[9] M. Mohammed and H. Peter Benzene Sensing Using Thin Films of Titanium Dioxide Operating at Room Temperature *Sensors,* 2 (2002) 374-382.

[10] C. C. Li, L. M. Li, Z. F. Du, H. C. Yu, Y. Y. Xiang, Y. Li, Y. Cai, T. H. Wang, Rapid and ultrahigh ethanol sensing based on Au-coated ZnO nanorods, Nanotechnology 19 (2008) 035501.

[11] M. Rincón, J. M. Getino, J. I. Robla, J. García Hierro, J. Mochón, I. Bustinza Gas sensor array for VOC's monitoring in soils contamination Ingeniería,14 (1), (2010) 45-54

[12] L. Deng, X. Ding, D. Zeng, S. Zhang and C. Xie, High Sensitivity and Selectivity of C-Doped WO3 Gas Sensors toward Toluene and Xylene. IEEE Sensors Journal, 12, (2012) 2209-2214.

[13] X. Zhang, J. Zhang, Y. Jia, P. Xiao and J. Tang, TiO2 Nanotube Array Sensor for Detecting the SF6 Decomposition Product SO2. Sensors, 12 (2012) 3302-3313.

[14] S. Lin, D. Li, J. Wu, X. Li, and S. A. Akbar A Selective Room Temperature Formaldehyde Gas Sensor Using TiO2 Nanotube Arrays. Sensors and Actuators B, 156 (2011) 505-509.

[15] E. Şennik, Z. Colak, N. Kılınç and O. ZaferZiya Synthesis of Highly-Ordered TiO2 Nanotubes for a Hydrogen Sensor. International Journal of Hydrogen Energy, 35 (2010) 4420-4427.

[16] O. K. Varghese, G. K. Mor, C. A. Grimes, M. Paulose and N. Mukherjee A Titania Nanotube Array Room Temperature Sensor for Selective Detection for Hydrogen at Low Concentration. Journal of Nanoscience and Nanotechnology, 4 (2004)733-737.

[17] Y. Kwon, H. Kim, S. Lee, I. J. Chin, T. Y. Seong, W. I. Lee, and C. Lee Enhanced Ethanol Sensing Properties of TiO2 Nanotube Sensors. Sensors and Actuators B, 173 (2012) 441-446.

[18] H. Kim, M. H. Hong, H. W. Jang, S. J. Yoon and H. H. Park, CO Gas Sensing Properties of Direct-Patternable TiO2 Thin Films Containing Multi-Wall Carbon Nanotubes. Thin Solid Films, 529 (2013) 89-93.

[19] K. Wetchakun, T. Samerjai, N. Tamaekong, C. Liewhiran, C. Siriwong, V. Kruefu, A. Wisitsoraat, A. Tuantranont and S. Phanichphant Semiconducting Metal Oxides as Sensors for Environmentally Hazardous Gases. Sensors and Actuators B:

Chemical, 160 (2011) 580-591.

[20] R. K. Bedi and I. Singh, Room Temperature Ammonia Sensors Based on Cationic Surfactant Assisted Nanocrystalline CuO Applied Mater. Interfaces 2(5) (2010) 1361-1368.

[21] R. K Bedi and I. Singh, Low Temperature Route to Nanocrystalline CuO Powder Journal Current Nanoscience 5(3) (2009) 273-277.

[22] I. Singh, G. Kaur and T. Singh, Impact of surfactant and CoSurfactant on the Structural, Morphological and electrical properties of nanocrystalline copper oxide *Current Reports on Science and technology* 1(1)(2015)18-26.

[23] L. Wang, S. Wang, M. Xu, X. Hu, H. Zhang, Y. Wang and W. Huang A Au-Functionalized ZnO Nanowire Gas Sensor for Detection of Benzene and Toluene. Physical Chemistry Chemical Physics, 15 (2013) 17179-17186.

[24] X. Song, D. Zhang and M. Fan A Novel Toluene Sensor Based on ZnO-SnO2 Nanofiber Web. Applied Surface Science, 255 (2009) 7343-7347.

[25] Q. Qi, T. Zhang, L. Liu, and X. Zheng, Synthesis and Toluene Sensing Properties of SnO2 Nanofibers. Sensors and Actuators B: Chemical, 137 (2009) 471-475.

[26] Y. Zeng, T. Zhang, L. Wang, M. Kang, H. Fan, R. Wang and Y. He Enhanced Toluene Sensing Characteristics of TiO2-Doped Flowerlike ZnO Nanostructures. Sensors and Actuators B: Chemical, 140 (2009) 73-78.

[27] X. Ding, D. Zeng, S. Zhang and C. Xie, C-Doped WO3 Microtubes Assembled by Nanoparticles with Ultrahigh Sensitivity to Toluene at Low Operating Temperature. Sensors and Actuators B: Chemical, 155 (2011) 86-92.

[28] K. S. Kim, W. H. Baek, J. M. Kim, T. S. Yoon, H. H. Lee, C. J. Kang and Y. S. Kim, A Nanopore Structured High Performance Toluene Gas Sensor Made by Nanoimprinting Method. Sensors, 10 (2010) 765-774.

[29] I. Singh, G. Kaur and R. K. Bedi, CTAB assisted growth and characterization of nanocrystalline CuO films by ultrasonic spray pyrolysis technique. Applied Surface Science 257(2011) 9546 9554.

[30] I. Singh and R. K. Bedi, Studies and correlation among the structural, electrical and gas response properties of aerosol spray deposited self assembled nanocrystalline CuO. Applied Surface Science 257(2011) 7592-7599.

[31] I. Singh and R. K. Bedi, Influence of pH on the synthesis and characterization of CuO powder for thick film room-temperature NH_3 gas sensor, *Journal of Material Science* 46 (2011)5568-5580.

[32] I. Singh, T. Singh and G. Kaur, Correlation among the structural, morphological and gas sensing parameters of USP deposited Al-CuO films Current Reports in Science and Technology 1(2) (2016) 38-45.

[33] I. Singh and R. K. Bedi, Surfactant-assisted synthesis, characterizations, and room temperature ammonia sensing mechanism of nanocrystalline CuO. Solid State Sciences 13(2011) 2011-2018.

[34] R. K. Bedi and Iqbal Singh (2009). CuO thick film sensors to detect ethanol at room temperature, Proceedings of the 53rd DAE Solid State Physics Symposium 327-328.

Curr. Rep. Sci. & Tech. 2 (1) (2016) 145-159

Artificial neural networks in material science research

Mohan Singh[1] and Harminder Kaur[2]
[1]Department of Physics, Khalsa College Amritsar, Punjab, India
[2]Department of Computer Science, Majha College For Women, Tarn Taran, Punjab (India)
mohansinghphysics@gmail.com

Abstract

We know that predictions play an important role in modern science and technology and for this artificial neural network techniques have played a wonderful role. Artificial neural networks are biologically inspired computer programs planned to simulate the way in which the human natural brain processes information. Artificial neural networks provide a range of powerful new techniques for solving problems in materials science and engineering applications. The primary aim of this review is to provide background information, motivation for the applications and overview of various methodology employed in the development of artificial neural network techniques in materials science research. The importance of artificial neural networks particularly in material research has grown dramatically during last few decades. Many researchers have investigated the potential use of artificial neural network systems and related products. Many new ideas and advance technology are boosting the field of neural network simulations and playing a crucial role in many tentative and cutting edge applications in material science and technology. We know that there is a great advancement in scientific techniques and helped greatly in understanding the different phenomenon involved in material functioning, but there is still a lack of progress in predicting various unknown properties of materials. Artificial neural network technique can be useful to solve the complexity involved in material science research. Our review shows that all the works on the application of artificial neural networks to materials science research have reported excellent and encouraging results. In the present review work, basics of artificial neural network and survey of published work with

particularly focus on its applications in various disciplines of material science and engineering have been reviewed and presented. It is specified that this review should be accessible to readers to provide new insights for practical use of artificial neural network techniques in various fields of material science and engineering.

Keywords

Artificial neural network, materials research, modelling, predictions.

1. Introduction

Most of the modern materials do not occur naturally and there is a need of advanced materials that meet human daily needs by applying the knowledge generated in materials science research. There is a large amount of materials available in modern materials world [1] as well as there is a great advancement in scientific techniques to understand the material functioning and their applications, but there is still a lack of realizing various properties of materials. There are numbers of complexities and increasing demand for new advanced materials, which impose new challenges to materials science research [2]. Various theoretical ideas, modelling and simulations, analyses are working to understand and predict different unknowns in materials science and engineering. Among these techniques, soft computing is the emerging and important category of prediction analysis. Soft computing based techniques and methods are becoming more popular in various areas of science research. Among various soft computing techniques, the fuzzy logic, artificial neural networks and genetic algorithms are very popular. Artificial neural networks recommended computational tools with tremendous advantages over the others. The importance of artificial neural networks especially in material science has grown prominently during last few decades. Artificial neural network technique can be useful to solve the complexity involved in material science research and engineering. Many researchers are investigating the potential use of neural network systems and products and as result very efficient outputs have been published regarding the material science and technology. This is manifested by an increasing number of scientific instruments and advance devices. The idea of building a machine

whose architecture and ideas are inspired by that of the natural human brain is very interesting. Nowadays, computational technology permits simulations of hundreds or even thousands of neurons and many tentative applications have been proposed. Many new ideas and advance technology have played a tremendous role and boosting the field of neural network simulations and their applications in different areas of material science and technology. The published literature suggests that artificial neural networks have been shown to be valuable tools in reducing the workload in scientific laboratories and providing decision support. The permeative use of artificial neural network in various applications makes it an indispensable tool in the development of products for the human life [2-4].

This paper aims to provide a comprehensive review of various artificial neural network approaches used in the field of material science research. Scholarly papers from different journals are categorized into specific applications (nanotechnology, ceramics research, alloy and steel research, composites research, glass research, and plastic and polymer research etc. It is hoped that this review will serve as a comprehensive state-of-the-art reference for materials scientists and engineers and will highlights the potential applications of artificial neural network in material science related problems and therefore will enhance the future of artificial neural network approach in material science research. The purpose of this review is to highlights the role played by artificial neural networks in various areas of materials science and engineering. We begin with basics of neural network, followed by a review and literature survey regarding the use of artificial neural network in material science research.

II. Neural Networks

The original work on neural networks was published by McCulloch and Pitts [5, 6] and Hebb [7]. Now, there has been a dramatic growth in the research activity in artificial neural networks [8-10]. Artificial neural networks (ANNs) have been applied to various fields of science and technology especially in materials science research. Artificial neural network is also called connectionist model, neural net, or parallel distributed processor model [11-17]. The neural networks have the ability to learn by example, which makes them very flexible and powerful. ANN is

a processing device revolutionised by the design and functioning of natural brain and its components. ANNs have been propelled from the human brain which is a highly complex, non linear and parallel computer and has the capability to organize its structural constituents (neurons) to perform computations (e.g. pattern recognition, perception) many times faster than the fastest digital computer. The human brain constitutes of billions of neurons connect with several other neurons and the learning involves adjustments to the synaptic connections exist between the neurons. The modification of synaptic weights is used for the design of artificial neural network. It can perform several tasks such as pattern matching and classification, optimization function, approximation, vector quantization and data clustering. ANN possesses large number of interconnected processing elements (nodes or neurons) that operate parallel and a single neuron is connected to other neuron by a connection link. Each connection link is linked with weights which contain information about the inputs and this information is utilized by neuron net to solve a specific problem. Each neuron has its own internal state called activity level, which is the function of the inputs. A neuron can send only one signal at a time, which can be transmitted to other several neurons. Consider neurons X_1 and X_2 transmitting signals to another neuron Y. X_1 and X_2 are input neurons and Y is the output neuron. X_1 and X_2 are connected to the output neuron Y with interconnection links with weights W_1 and W_2 respectively. Several artificial neural network architectures and algorithms (e.g., multilayer perceptron, radial basis function network, recurrent neural network etc.) have been developed and authenticated in the literature [12-14, 17-25].

III. Advantages and Applications of Neural Network

Neural networks have the ability to extract meaningful outputs from complicated and complex data. The trained neural network is an expert for given information given to analyse and provides new projections, predictions and possibilities in any situation of interest. Neural networks have the large number of properties and capabilities like nonlinearity, input output mapping, adaptivity, evidential response, contextual information, fault tolerance via redundant information coding, very large scale

integrated (VSLI) implimentability, uniformity of analysis and design, neural biological analogy, self organization, real time operation etc. It provides important and cutting edge applications in multidisciplinary directions such as computer science, artificial intelligence, approximation theory, physics, chemistry, material science, neurobiology, dynamical systems, engineering, image/signal processing, robotics technology, cognitive, linguistic, philosophy, economics and finances, air traffic control, animal behaviour, appraisal and valuation, betting, criminal sentencing, complex physical and chemical processes, data mining, cleaning and validation, direct mail advertisers, echo patterns, econometric modelling, employee hiring, expert consultants, fraud detection, handwriting and typewriting, machinery control, medical diagnosis, medical research, music composition, photos and fingerprints, recipes and chemical formulations, voice recognition, weather prediction etc. A rapid increase in our understanding of artificial neural networks leading to the improved network paradigms and provide enormous application opportunities in materials science and engineering research.

IV. Neural Network in Material Science Research

The important materials used in the design and manufacture of useful products are alloys, plastics, wood, composites, ceramics, metals, fabrics etc. There is a dire need to understand the properties of materials both experimentally and theoretically to use their potential in various cutting edge applications. Among various scientific techniques, artificial neural network can enhance the output and performance of scientific research. The applications of artificial neural network models in materials science research are increasing in popularity. Most of the model consists of some important steps like generation of training data, selection of a network type, selection of the input and the output for the network, design of a suitable network configuration, selection of a suitable training strategy, training and validation of the resulting network [15, 26]. Artificial neural networks based tools have been applied in prediction, modelling, control, identification design and optimisation areas of materials science and engineering research. The important reason for the use of artificial neural networks in materials science research is its ability to recognise and learn

the underlying nonlinear relations between input and output without the need to construct an explicit mathematical model.

Some reviews, developments, discussions and criticisms are available regarding the achievements and importance of artificial neural networks in different field of science and technology e.g., instrumentation and measurement application, astronomy, chemistry, chemical engineering, material synthesis, high energy physics, materials science, materials design etc. [8, 27-67). Hoskins and Himmelblau [27] applied ANNs to error diagnosis for a chemical process. Nadi *et al* [28] depicted an adaptive learning architecture for modelling manufacturing processes involving various control variables. The model was produced by the integration of influence diagrams and neural networks. Using artificial neural networks, Larsen *et al* [29] illustrated the method using a nonlocal thermodynamic equilibrium theoretical atomic physics model for *k*-shell x-ray spectroscopy of a high density, high temperature aluminium plasma. In order to solve the problems inherent in the application of complex fittings to the response of detectors in gamma spectroscopy, Olmos *et al* [30] used neural network method based on the associative memory algorithm. Hudson [31] reported the basic artificial neural network theory to explore the applicability of neural network technologies for their specific applications. Miller [32] reviewed the applications of neural network in astronomy. Bishop [8] presented the basic neural network models in detail and explained the various techniques used to train them for different practical problems. Duch and Diercksen [33] reported different applications of the neural network methods to solve various problems in physics and chemistry. Ramchandran and Rhinehart [34] discussed several applications and advantages of artificial neural networks. Sumpter and Noid [35] discussed different application and developments of computational neural networks for the design, analysis and characterization of materials. Ai [36] discussed the applications of artificial neural network for metallurgical industry. Bensaoula *et al* [37] established the use of a multilayer neural network in semiconductor thin film deposition processes. Chen *et al* [38] proposed a model to relate the materials structure and properties to predict the properties of new materials using a self-architecting neural network. Bhadeshia [39] introduced the

neural networks and discussed their applications in materials science. Denby [40] presented the applications of neural network in high energy physics. Hussain [41] presented the applications of artificial neural networks in chemical process control, simulation, and online implementation. Kalogirou and Bojic [42] have highlighted the capability of artificial neural networks in energy-prediction and modelling. Goyache *et al* [43] illustrated the use of artificial neural networks in food industry. Hancheng *et al* [44] developed an adaptive fuzzy neural network for drawing out fuzzy rules directly from experimental data for material property modelling. Meireles *et al* [45] introduced a comprehensive review of the industrial applications of artificial neural networks. Venkatasubramanian *et al* [46] presented a review of process fault detection and diagnosis in process engineering using artificial neural networks. Zhang and Friedrich [47] discussed various potentials of the neural network for predicting properties of polymer composite materials. Fernandes and Lona [48] presented a brief tutorial for selecting and training neural networks for applications in polymerization engineering field. Zhang *et al* [49] develped a genetic neural network algorithm for materials design. Belic [50] described the use of neural networks as an approximation-modelling tool for practical applications in vacuum science problems. Du and Sun [51] discussed the capabilities of artificial neural networks for food quality evaluation. Sha and Edwards [52] discussed some important points regarding the use of neural networks in material research. Behler *et al* [53] discussed a combination of the metadynamics method for the investigation of pressure-induced phase transitions in solids with a neural network representation of high-dimensional density-functional theory (DFT) potential-energy surfaces. Hacib *et al* [54] proposed a method based on finite element method and radial basis function neural network for the robust identification of electromagnetic properties. Roupas [55] executed an overview of artificial neural networks for dairy product research. Vasseur *et al* [56] discussed the photon beam dose calculations using artificial neural networks. Ahmad and Zhang [57] discussed new techniques to improve neural network model robustness for nonlinear process modelling. Ludwig *et al* [58] demonstrated the applications of neural models in petroleum engineering. Marini [59]

discussed the neural network architectures for food analytical problems. Odetunji and Lasisi [60] provided a systematic review regarding the application of soft computing techniques in materials engineering. Costanza *et al* [61] used the application of artificial neural network for the characterization of mechanical properties of materials. Noor *et al* [62] reviewed the use of artificial neural networks in modelling and control of the polymerization processes. Curteanu and Cartwright [63] discussed some methods to develop neural networks for chemical engineering applications. Ma and Jiang [64] discussed fault detection and diagnosis methods and their applications in nuclear power plants. Alexandridis *et al* [65] presented a systematic approach for correlating the refractive index of material with experimentally measured inputs like wavelength, temperature, and concentration using neural network models. Pirdashti *et al* [66] published a comprehensive review of various ANN applications in the field of chemical engineering. Denizer *et al* [67] developed an optimization algorithm based on the neural network architecture to interpret the diffraction data. Artificial neural network technique have been widely used by many authors in different branches of advanced material science research such as *Materials classification*, Rutherford backscattering spectrometry and elastic recoil detection spectra, Elemental analysis, Material characterization by Indentation, Glass research, Glass transition temperature, Elastic constants, Sensors technology, Solar radiation/power prediction, Nanotechnology, Mossbauer spectra research, Super-capacitor research, Luminescence research, Microscopy, Liquid crystals research, Nuclear magnetic resonance spectra, Photovoltaic power generation, Fuel cell research, Material defects and fractures, Surface roughness prediction, Coating technology, Textile technology, Lithium ion batteries, Welding research, Thermal conductivity, Infrared spectra analysis, Pollution research, Superconducting materials, Milling process, Corrosion research, Ceramics, Film deposition and characterization, Electric/dielectic and magnetic characteristics, Crystal research, Alloy and Steel research, Plastic/polymer/ rubber technology, Composite material research.

V. Conclusion

In this review paper, we have presented an extensive and exhaustive

review of the literature regarding the applications of artificial neural network techniques in materials science and engineering research. The artificial neural network techniques are appropriate and very efficient at handling imprecise, uncertain, ambiguous, incomplete, and subjective data and information. The interface between materials science and engineering research and intelligent systems engineering techniques, such as the artificial neural network, is very emerging way in modern era of technology. Therefore, there is a dire need to boost the readers with the importance and capabilities of artificial neural network techniques used in material science and engineering research reduce the gaps of knowledge. It becomes desirable to have a computational framework within which various materials predictions could be explored. This can be achieved through the use of artificial neural network techniques in various material research and engineering areas due to their potential of making materials research more effective and efficient. This review suggests future works related to artificial neural network techniques in several areas of material science and technology. Finally, this review serves as a best reference of artificial neural network related approaches for material science research and highlights the potential applications of artificial neural network in material science research problems.

VI. References

[1] Ermolaeva, N. A., Kaveline, K. G. and Spoormaker, J. L., "Materials selection combine with optimal structure design: concept and some result" Mater. Des. 23 (2002) 459-470.

[2] Dobrzanski, L. A., "Significance of materials science for the future development of societies" J. Mater. Process. Technol. 175 (2006)133-148.

[3] Ashby, M. F., "Multi-objective optimization in material design and selection" Acta materialia 48 (2000) 359-369.

[4] Zhang, Y. M., Yang, S. and Evans, J. R. G., "Revisiting Hume-Rotherys rules with artificial neural networks" Acta Materialia 56 (2008) 1094-1105.

[5] McCulloch, W. S., and Pitts, W. A., "Logical calculus of the ideas imminent nervous activity" Bull Math Biophys. 5 1943 115-133.

[6] McCulloch, W. S. and Pitts, W. A., How we know universals: the perception of visual and auditory forms Bull Math Biophys. 9 1947 127-147.

[7] Hebb, D. O., "The organization of behavior: a neuropsychological" New York: Wiley (1949).

[8] Bishop, C. M., "Neural networks and their applications" Review of Scientific Instruments 65 (1994) 1803-1831.

[9] Yang, M. and Wei, H., "Application of a neural network for the prediction of crystallization kinetics" *Industrial and Engineering Chemistry Research* 45 (2006)70-75.

[10] Sivanandan, S. N. and Deepa, S. N., "Principle of Soft Computing", 2nd edition Wiley Inda, Pvt. Ltd. (2011).

[11] Lippmann, R. P., "Introduction to computing with neural nets" IEEE ASSP Magazine 4 (1987) 4-22.

[12] Lippmann, R. P., "Pattern classification using neural networks" IEEE Commun. Mag. 11 (1989) 47-64.

[13] Schalkoff, R. J., "Artificial neural networks" New York McGraw-Hill (1997).

[14] Wang, S., "Neural networks in generalizing expert knowledge" Comput. Ind. Eng. 32 (1997) 67-76.

[15] Basheer, I. A. and Hajmeer, M., "Artificial neural networks: fundamentals, computing, design, and application" J. Microbiol. Methods 43 (2000) 3-21.

[16] Waszczyszyn, Z. and Ziemianski, L., "Neural networks in mechanics of structures and materials- new results and prospects of applications" Comput. Struct. 79 (2001) 2261-2276.

[17] Mellit, A. and Kalogirou, S. A., "Artificial intelligence techniques for photovoltaic applications: A review" Prog. in Energy and Combustion Sci. 34 (2008) 74-632.

[18] Hornik, K., Stinchombe, M. and White, H., "Multilayer feedforward networks are universal approximators" *Neural Networks* 2 (1989) 359-366.

[19] Elman, J., "Finding structure in time" Cognitive Sci. 14 (1990) 179-211.

[20] Parlos, A., Chong, K. and Atiya, A., "Application of the recurrent

multilayer perceptron in modelling complex process dynamics" IEEE Transaction on Neural Networks (5) 2 (1994) 255-266.

[21] Giles, C. L., Horne, B. G. and Lin, T., "Learning a class of large finite state machines with a recurrent neural network" Neural Networks 8 (1995) 1359-1365.

[22] Draye, J., Pavisic, D. and Libert, G., "Dynamic recurrent neural networks: a dynamical analysis" IEEE Trans. Syst. Man. Cybern. (26) 5 1996 692-706.

[23] Haykin, S., "Neural networks: a comprehensive foundation" In (2nd Ed). New York MacMillan (1999).

[24] Cheroutre-Vialette, M. and Lebert, A., "Modelling the growth of listeria monocytogenes in dynamic conditions" Int. J. Food. Microbiol 55 (2000) 201-207.

[25] Seker S Ayaz, E. and Turkcan, E., "Elman's recurrent neural network applications to condition monitoring in nuclear power plant and rotating machinery" Eng. Appl. Artif. Intell. 16 (7-8) (2003) 647-656.

[26] Rao, H. S. and Mukherjee, A., "Artificial neural networks for predicting the macromechanical behaviour of ceramic-matrix composites" Comput. Mater. Sci. 5 (1996) 307-322.

[27] Hoskins, J. C. and Himmelblau, D. M., "Artificial neural network models of knowledge representation in chemical engineering" *Comput. Chem. Eng.* 12 (1988) 881-890.

[28] Nadi, F., Agogino, A. M. and Hodges, D. A., "Use of influence diagrams and neural networks in modeling semiconductor manufacturing processes" IEEE Transactions on Semiconductor Manufacturing 4 (1991) 52-58.

[29] Larsen, J. T., Morgan, W. L. and Goldstein, W. H., "Artificial neural networks for plasma x-ray spectroscopic analysis" Review of Scientific Instruments 63 (1992) 4775-4777.

[30] Olmos, P., Diaz, J. C., Perez, J. M., Garcia-Belmonte, G., Gomez, P. and Rodellar, V., "Application of neural network techniques in gamma spectroscopy" Nuclear Inst. and Methods in Physics Research A 312 (1992) 167-173.

[31] Hudson, W. B., "Introduction and overview of artificial neural networks in instrumentation and measurement application"

Conference Record-IEEE Instrumentation and Measurement Technology Conference (1993) 623-626.

[32] Miller, A. S., "A review of neural network applications in Astronomy" Vistas in Astronomy 36 (1993) 141-161.

[33] Duch, W. and Diercksen, G. H. F., "Neural networks as tools to solve problems in physics and chemistry" Computer Physics Communications 82 (1994) 91-103.

[34] Ramchandran, S. and Rhinehart, R., "Do neural networks offer something for you?" InTech 42 (1995) 59-64.

[35] Sumpter, B. G. and Noid, D. W., "On the design, analysis, and characterization of materials using computational neural networks" Annual Review of Materials Science 26 (1996) 223-277.

[36] Ai, L., "Application of artificial neural network in metallurgical industry" *Journal of Iron and Steel Research International* 9 (1997) 60-63.

[37] Bensaoula, A., Malki, H. A. and Kwari, A. M., "The use of multilayer neural networks in material synthesis" IEEE Transactions on Semiconductor Manufacturing 11 (1998) 421-431.

[38] Chen, C. L. P., Cao, Y. and LeClair, S. R., "Materials structure-property prediction using a self-architecting neural network" Journal of Alloys and Compounds 279 (1998) 30-38.

[39] Bhadeshia, H. K. D. H., "Neural networks in materials science" ISIJ International 39 (1999) 966-979.

[40] Denby, B., "Neural networks in high energy physics: A ten year perspective" Computer Physics Communications 119 (1999) 219-231.

[41] Hussain, M. A., "Review of the applications of neural networks in chemical process control-simulation and online implementation" Artif. Intell. Eng. 13 (1999) 55-68.

[42] Kalogirou, S. A. and Bojic, M., Artificial neural networks for the prediction of the energy consumption of a passive solar building Energy 25 (2000) 479-491.

[43] Goyache, F., Bahamonde, A., Alonso, J., Lopez, S., del Coz, J. J., Quevedo, J. R., Ranilla, J., Luaces, O., Alvarez, I., Royo, L. J. and Diez, J., "The usefulness of artificial intelligence techniques to assess

subjective quality of products in the food industry" Trends Food Sci. Technol. 12 (2001) 370 -381.

[44] Hancheng, Q., Bocai, X., Shangzheng, L. and Fagen, W., "Fuzzy neural network modeling of material properties" Journal of Materials Processing Technology 122 (2002) 196-200.

[45] Meireles, M. R. G., Almeida, P. E. M. and Simoes, M. G., "A comprehensive review for industrial applicability of artificial neural networks" *IEEE Transactions on Industrial Electronics* 50 (2003) 585-601.

[46] Venkatasubramanian, V., Rengaswamy, R., Yin, K., Kavuri, S. N., "A review of process fault detection and diagnosis. Part I: quantitative model-based methods" Comput. Chem. Eng. 27 (2003) 293-311.

[47] Zhang, Z. and Friedrich, K., "Artificial neural networks applied to polymer composites: a review" Compos Sci Technol 6 (2003) 2029-2044.

[48] Fernandes, F. A. N. and Lona, L. M. F., "Neural network applications in polymerization processes" Braz. J. Chem. Eng. 22 (2005) 323-330

[49] Zhang, Y., Li, X., Zeng, L. and Chang, C., "Application of materials design based on genetic neural network" Key Engineering Materials 280-283 (2005) 1837-1840.

[50] Belic, I., "Neural networks and modelling in vacuum science" Vacuum 80 (2006) 1107-1122.

[51] Du, C. J. and Sun, D. W., "Learning techniques used in computer vision for food quality evaluation: a review" J Food Eng 72 (2006) 39-55.

[52] Sha, W. and Edwards, K. L., "The use of artificial neural networks in materials science based research" Materials and Design 28 (2007) 1747-1752.

[53] Behler, J., Martonak, R., Donadio, D. and Parrinello, M., "Pressure-induced phase transitions in silicon studied by neural network-based metadynamics simulations" Physica Status Solidi (B) Basic Research 245 (2008) 2618-2629.

[54] Hacib, T., Mekideche, M. R., Moussouni, F., Ferkha, N. and Brisset, S., "Generalized RBF neural network and FEM fornmaterial characterization through inverse analysis" *Studies in computational intelligence* 119 (2008) 11-19.

[55] Roupas, P., "Predictive modelling of dairy manufacturing processes" Int. Dairy J. 18 (2008) 741- 753.

[56] Vasseur, A., Makovicka, L., Martin, E., Sauget, M., Contassot-Vivier, S. and Bahi, J., "Dose calculations using artificial neural networks: a feasibility study for photon beams" Nuclear Instruments and Methods in Physics Research Research B 266 (2008) 1085-1093.

[57] Ahmad, Z. and Zhang, J., "Selective combination of multiple neural networks for improving model prediction in nonlinear systems modeling through forward selection and backward elimination" Neurocomputing 72 (2009) 1198-1204.

[58] Ludwig, J. O., Nunes, U., Araujo, R., Schnitman, L., Lepikson, H. A., "Applications of information theory, genetic algorithms, and neural models to predict oil flow" Commun Nonlinear Sci 14 (2009) 2870-2885.

[59] Marini, F., "Artificial neural networks in foodstuff analyses: trends and perspectives. A review" Anal Chim Acta 635 (2009) 121-131.

[60] Odetunji, A. O. and Lasisi, E., U., "Applications of soft computing techniques in materials engineering: A review" African Journal of Mathematics and Computer Science Research 2(7) (2009) 104-131.

[61] Costanza, G., Tata, M. E. and Ucciardello, N., "Application of neural network to the materials characterization" International Journal of Computational Materials Science and Surface Engineering 3 (2010) 96-113.

[62] Noor, R. A. M., Ahmad, Z., Mat Don, M. and Uzir, M. H., "Modelling and control of different types of polymerization processes using neural networks technique: a review" Can. J. Chem. Eng. 88 (2010) 1065-1084.

[63] Curteanu, S., and Cartwright, H., "Neural networks applied in chemistry.I. Determination of the optimal topology of neural networks" *J Chemometr* 25 (2011) 527-549.

[64] Ma, J. and Jiang, J., "Applications of fault detection and diagnosis methods in nuclear power plants: a review" Prog. Nucl. Energ. 53 (2011) 255-266.

[65] Alexandridis, A., Chondrodima, E., Moutzouris, K. and Triantis, D., "A neural network approach for the prediction of the refractive index

based on experimental data" Journal of Materials Science 47 (2012) 883-891.

[66] Pirdashti, M., Curteanu, S., Kamangar, M. H., Hassim, M. H. and Khatami, M. A., "Artificial neural networks: applications in chemical engineering" Reviews in Chemical Engineering 29 (2013) 205-239.

[67] Denizer, B., Ustundag, E., Ceylan, H., Li, L. and Lee, S. Y., "Engineering neutron diffraction data analysis with inverse neural network modelling" Materials Science Forum 772 (2014) 39-44.

Curr. Rep. Sci. & Tech. 2 (1) (2016) 160-168

Role of Anionic Surfactant in the Growth of Nanostructured SnO_2 by Non Aqueous Sol Gel Method

Kamalpreet Khun Khun[1], Iqbal Singh[1], Rajan Saini[1], Gursharan Kaur[1], Taminder Singh[1] and R.K Bedi[2]
[1]Post Graduate Department of Physics, Khalsa College Amritsar-143005
[2]Materials Science Research Laboratory, Department of Physics, Guru Nanak Dev University, Amritsar-143005
kamal_minty@rediffmail.com

Abstract

Highly porous nanostructured Tin oxide (SnO_2) powder has been synthesized by a simple nonaqueous sol gel method using $SnCl_2 \cdot 2H_2O$ and C_2H_5OH as precursors. The precursor solution was modified by introduction of anionic surfactant namely SDS (sodium do-decyl sulphate) to carry out a comparative study of the properties of SnO_2 powder samples prepared from unmodified and surfactant modified solutions. The thermal decomposition behavior of the gel samples prepared by heating the precursor solution was studied by thermogravimetric and differential thermal analysis for selecting an optimal calcination temperature. The studies show the absence of any major weight loss regions beyond 500ºC for both the gel samples which confirms that a temperature of 500ºC and above was suitable for the removal of surfactants and other carbon impurities for producing nanostructured SnO_2 powder. Structural properties of SnO_2 powder samples prepared by calcining the gels at 550ºC for 3 hours were investigated by XRD and FESEM. The studies reveal that modification of precursor solution by SDS leads to reduction in crystallite size and significant changes in the morphology and porosity of SnO_2 powder samples. These changes were found to improve the sensing characteristics of thick films based on nanostructured SnO_2 powder and an extremely high response of 978% towards ammonia was obtained at an operating temperature of 200ºC.

Keywords

Tin oxide, Surfacatant, morphology, sensing

I. Introduction

Nanostructured materials have been of great interest in recent years because of their improved properties as compared to conventional microcrystalline materials [13] Out of the wide range of materials, nanostructured metal oxides form an important class that has been explored extensively due to their use in large number of applications such as solar cells, transparent conducting electrodes, transistors, lithium batteries and most importantly in gas sensing [4-6]. SnO_2 is one of the most important member of this family that has been widely investigated for its gas sensing applications. The large surface to volume ratio of nanostructured forms of SnO_2 enhances the gas response characteristics and hence makes it highly suitable for sensing applications. Studies on SnO_2 based gas sensors have shown that small particle size, a large surface to volume ratio, good crystallinity and high porosity are required to enhance its gas sensing ability [7,8] Therefore in recent years simple and efficient techniques for developing nanostructured SnO_2 have achieved great significance. Different solution phase techniques like homogeneous precipitation, hydrothermal route, sol gel method, sol gel combustion etc, [9-11]. have been widely used for preparation of nanostructured SnO_2 powders and films. In order to obtain nanostructured SnO_2 with good crystallinity and high porosity solution based routes by use of different templates has been widely reported in literature. These routes are found to be much simpler and cost effective in comparison to other techniques for synthesis of nanostructured materials. Use of surfactants in solution based synthesis is one such method that is particularly interesting as these organic compounds in conjunction with inorganic compounds in solutions acts as templates and permit a greater control on the particle size and porosity of the final synthesized material [12]. This technique has been mainly used in aqueous solutions as reported by different researchers. However only few reports are available on the usage of surfactants in non aqueous routes for synthesis of nanostructured metal oxides.

In this work an attempt has been made to synthesize nanostructured SnO_2 by an unmodified and surfactant modified nonaqueous sol gel method. The obtained samples were studied for their structural and gas sensing properties to explore the role of anionic surfactant SDS in modifying the properties of synthesized SnO_2

II. Experimental

Porous nanostructured SnO_2 powder samples have been synthesized by a nonaqueous sol gel method using stannous chloride and ethanol as precursors. SnO_2 sol was prepared by dissolving 0.025 moles of $SnCl_2 \cdot 2H_2O$ in 50ml ethanol . The mixture was then well stirred and heated at 50 °C in a closed vessel. For preparation of surfactant modified samples, 0.5M aqueous micellar solution of anionic surfactant SDS has been prepared by separately dissolving required amount of surfactant in 50 ml of water. The solution is then stirred magnetically for one hour to obtain clear micellar solutions. Small volume (5 ml) of surfactant solution was then added to the starting solutions for modifying the synthesis route. The solutions prepared from unmodified and surfactant modified precursors were finally heated in an oven at 120 °C until the solvent was completely evaporated to form a thick viscous gel. The gel samples prepared from the two solutions were then calcined at temperature of 550ºC for 3 hours to obtain SnO_2 powder samples.

For preparation of thick films a known quantity of the synthesized SnO_2 powder was thoroughly mixed with a few drops of diethanolamine and grinded in a mortar and pestle to obtain a fine paste. The paste was coated onto glass substrate and the film so obtained was annealed at a temperature of 400ºC for 1 hour to remove the organic binder.

The thermal decomposition behavior of the gel samples obtained from unmodified and surfactant modified precursors was studied in air atmosphere using Perkin Elmer Pyris diamond thermal analyzer in the temperature range from 25 to 700 °C. The crystal phases in the calcined powder were studied by X-ray diffractometer (X'Pert Panalytical) operated at 40 kV, 30 mA over 20°70° with a scan rate of 0.002°/s. The surface morphology and composition of the powder samples was investigated

using field emission scanning electron microscopy by FESEM JEOL JSM 6700 with a beam voltage 25 kV.

The sensor performance of thick SnO_2 films was tested in a home built test chamber in the operating temperature range (25-250ºC). A known volume of the gas to be tested was introduced in the chamber and the resistance of the sensor was measured by an electrometer as a function of time. The gas sensing response R (%) of the film is calculated by the relation as reported earlier [13]

III. Results and Discussion

A. Thermal Analysis

The TGA/DTA curves of the gel samples prepared from unmodified and SDS modified precursors are shown in Figure 1. TGA curves for both the samples show weight loss of 7.5-8.1, 14.3-17 and 11.1-14 % in temperature range of 25 -160C, 160-280C and 280- 500C respectively. The first weight loss in the samples is mainly attributed to release of residual solvent which results in emergence of an endothermic peak in the DTA curves. A pronounced endothermic peak corresponding to this region in case of SDS modified gel sample [fig 1(b)] can be attributed to ionic nature of surfactant which forms strong metal surfactant complexes that require larger heat energy for decomposition and removal of surfactants. The second weight loss is presumably due to decomposition of organic matter. The third weight loss is due to removal of residual surfactant and other carbon impurities. These observations are in close agreement with those reported earlier for surfactant assisted grown nanoporous SnO_2 [14,15]. Absence of any major weight loss and endo-exothermic reaction regions beyond 500C indicates that gel samples have been completely decomposed to SnO_2 powder at this temperature. Therefore a minimum temperature of 500C is required to remove the surfactants and left over carbon content for producing pure nanostructured SnO_2 powder.

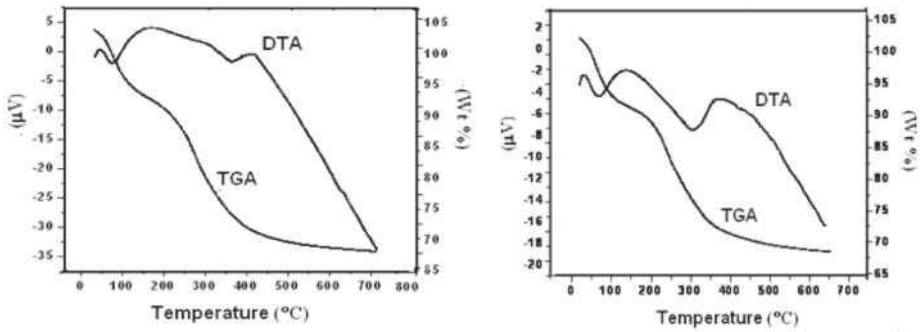

Fig 1. TGA/DTA curves of (a) unmodified and (b) surfactant modified SnO_2 gel samples

B. Structural properties

XRD patterns of SnO_2 powder samples prepared by calcining the SnO_2 gel samples at 550C for 3 hours are shown in Figure 2.The presence of sharp and well resolved peaks show polycrystalline nature of both the samples. Prominent diffraction peaks and their positions confirms the formation of tetragonal rutile structured SnO_2 (JCPDS 41-1445). Absence of any characteristic peaks of SDS in the XRD pattern in Fig. 2 (b) further confirms the formation of pure SnO_2. Markedly broadened peaks corresponding to reflections from (110), (101) and (211) planes in SnO_2 samples prepared from SDS modified precursors suggest that the sample is composed of comparatively smaller crystallites. The average crystallite size estimated from the Scherrer's formula [16] is found to be 18.9 and 9.2 nm for unmodified and surfactant modified SnO_2 respectively. It is thus clear that the addition of surfactant in the starting solution leads to reduction in crystallite size which can be attributed to the capping effect of anionic surfactant SDS that hinders the growth of SnO_2 nanoparticles [17]

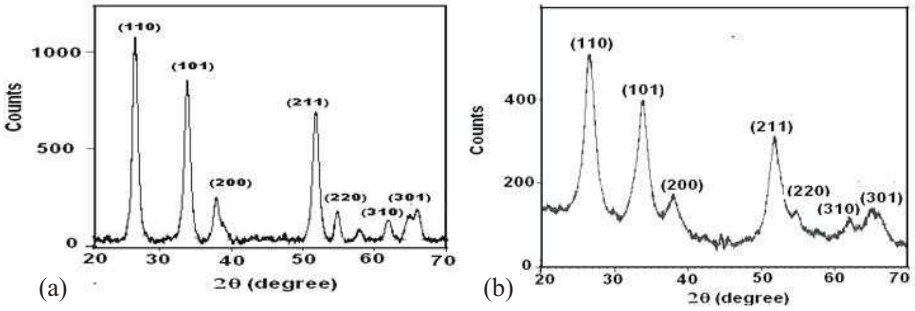

Fig 2. *XRD patterns of (a) unmodified and (b) surfactant modified SnO_2 powder samples*

The surface morphology of SnO_2 powder samples as examined by FESEM is shown in Figure 3. It is observed that the SnO_2 powder prepared from unmodified precursors is composed of hard agglomerates whereas loosely held spherical agglomerates formed from an interconnected network of finer primary particles is observed in case of the SnO_2 powder synthesized from SDS modified precursors. The decrease in agglomeration on introduction of SDS can be due to the formation of metal surfactant complexes that forms a network and stops the precursor molecules to come closer. Further heating of such a solution leads to decomposition of these complexes which leaves behind a large number of pores and results in increased porosity of the sample as observed in figure 3(b) [17]. The studies thus reveal that SDS plays an important role in changing the morphology, particle size and porosity of SnO_2 samples.

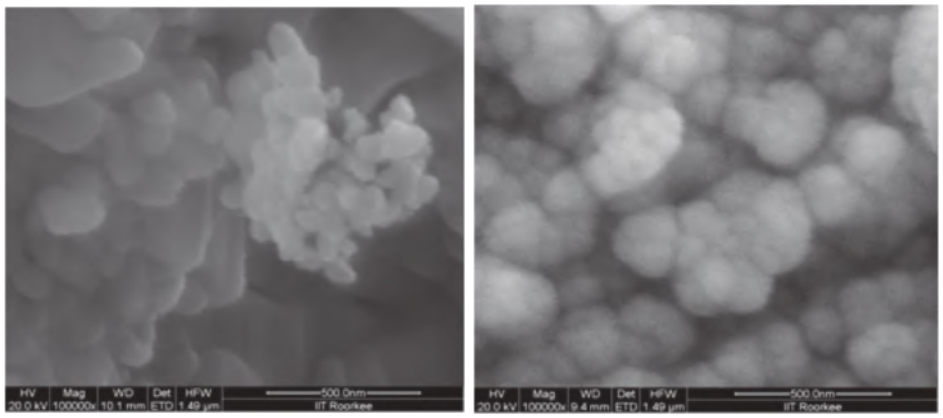

(a) (b)

Fig 3. *FESEM images of (a) unmodified and (b) surfactant modified SnO_2 powder samples*

C. Sensing Charactersistics

Thick films based on unmodified and surfactant modified SnO_2 samples were tested for sensing response towards gases and vapors like ammonia, chlorine, ethanol and acetone at different operating temperatures. The studies showed that the films were sensitive to ammonia and exhibited a good response at an operating temperature range of 150-200ºC. However the comparative studies of the films prepared from unmodified and surfactant modified samples reveals a much higher response in case of surfactant modified SnO_2 film.

The resistance time curves for the films exposed to 50 ppm of ammonia at an operating temperature of 200ºC are shown in Figure 4. Observations reveal that resistance of films increases on exposure to ammonia in all the samples which may be based on the reactions of ammonia with the adsorbed oxygen species [13]. The response %, response and recovery time estimated from the curves are given in table 1. The results suggest that in addition to good high response towards ammonia, the surfactant modified films also exhibits fast response and recovery time in comparison to unmodified SnO_2 film. The exceptionally high value of response towards ammonia by can be attributed to large effective surface area provided by nanosized particles in modified film which enhances gas adsorption whereas a comparatively faster response and recovery time can be due to high porosity that facilitates quick gas adsorption and desorption at the reactive sites.

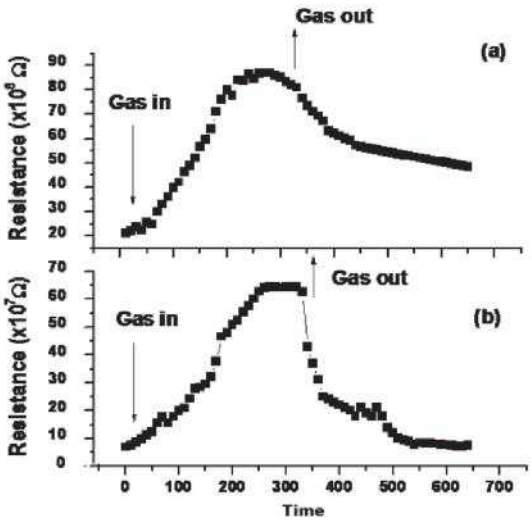

Fig 4. *Resistance Time curves of (a) unmodified and (b) surfactant modified SnO_2 powder samples*

Gas	Parameters	Unmodified SnO_2	Surfactant modified SnO_2
NH_3	Operating Temperature	[illegible]	200ºC
	[illegible]	$2.32x10^7$	$6.01x10^7$
	Rg(Ω)	$8.7x10^7$	$6.48x10^8$
	Response %	275	978
	Response time (sec)	245	180
	Recovery time(sec)	No recovery	190

IV. Conclusions

Porous nanostructured SnO_2 powder has been synthesized by a simple and inexpensive non aqueous sol gel method. Studies conclude that the

modification of the synthesis route by addition of small amounts of anionic surfactant SDS results in decrease in particle size and increase in porosity of SnO_2.This suggests that SDS effectively acts as a capping agent in the synthesis route and inhibits the growth of the particles. The agglomeration behavior of the particles is also observed to change in the presence of surfactant and loosely bound spherical agglomerates formed by a network of primary particles have been obtained whereas comparatively hard agglomerates without any specific shape were formed in case of unmodified SnO_2.These modified properties were found to enhance the sensing characteristics of the synthesized SnO_2

V. References

[1] K. Zhou, R. Wang, B. Xu, Y. Li, Synthesis, characterization and catalytic properties of CuO nanocrystals with various shapes, Nanotechnology 17 (2006) 39393943.

[2] C. Qian, F. Kim, L. Ma, F. Tsui, P. Yang, J. Liu, Solution-phase synthesis of Single crystalline iron phosphide nanorods/nanowires, J. Am. Chem. Soc. 126 (2004) 11951198.

[3] J.C. Lee, T.G. Kim, W. Lee, S.H. Han, Y.M. Sung, Growth of CdS nanorodcoated TiO2 nanowires on conductive glass for photovoltaic applications, Cryst. Growth Des. (2009) 45194523

[4] J. Sun, Q. Tang, A. Lu, X. Jiang, Q. Wan, Individual SnO2 nanowire transistors fabricated by the gold microwire mask method, Nanotechnology 20 (2009), 255202 (14).

[5] S Ferrere, A. Zaban, B.A. Gregg, Dye sensitization of nanocrystalline tin oxide by perylene derivatives, J. Phys. Chem. B 101 (1997) 44904493

[6] Y. Idota, T. Kubota, A. Matsufuji, Y. Maekawa, T. Miyasaka, Tin-based amorphous oxide: a high-capacity lithium-ion-storage material, Science 276 (1997)13951397.

[7] J. Zhao, L.H. Huo, S. Gao, H. Zhao, J.G. Zhao, Alcohols and acetone sensing properties of SnO_2 thin films deposited by dip-coating, Sens. Actuators B. 115 (2006)460464.

[8] Z. Ying, Q. Wan, Z.T. Song, S.L. Feng, SnO2 nanowhiskers and their

ethanol sensing characteristics, Nanotechnology 15 (2004) 16821684.

[9] F. Gu, S.F. Wang, M.K. Lu, G.J. Zhou, D. Xu, D.R. Yuan, Photoluminescence properties of SnO2 nanoparticles synthesized by sol−gel method, J. Phys. Chem. B 108 (2004) 8119- 8123.

[10] H. Yang, X. Song, X. Zhang, W. Ao, G. Qiu, Synthesis of vanadium-doped SnO_2 nanoparticles by chemical co-precipitation method, Mater. Lett. 57 (2003) 31243127.

[11] L. Fraigi, D.G. Lamas, N.E. Walsoe de Reca, Novel method to prepare nanocrystalline SnO_2 powders by a gel-combustion process, Nanostruct. Mater. 11(1999) 311318.

[12] G.Q. Liu, Z.G. Jin, X.X. Liu, T. Wang, Z.F. Liu, Anatase TiO2 porous thin films prepared by solgel method using CTAB surfactant, J. Sol Gel Sci. Technol.41(2007) 4955.

[13] Kamalpreet Khun Khun, Aman Mahajan, and R. K. Bedi, SnO2 thick films for room temperature gas sensing applications" Journal of Applied Physics 106, 124509 (2009)

[14] Vel´ asquez, C., Rojas, F., Ojeda, M.L., Ortiz, A. and Campero, A, Structure and texture of self-assembled nanoporous SnO2. Nanotechn. 16: (2005)12781284.

[15] Hongjun, J.I, Xiaoheng L., Xin, W., Xujie, Y., Lude, L.U., Xiutao, G.E. and Yonghong, L. (2011). Self-assembled SnO_2 Colloidal Particles and Their Gas Sensing Performance to H2, C2H5OH and LPG. J. Wuhan Univ. Techn. MaterSci. Ed. (2011) 26(4): 661-667.

[16] Klug, H. P. and Alexander, L. E. X-ray diffraction procedure for polycrystalline and amorphous materials. (1974). pp 687 2nd edition Wiley, New York.

[17] Kamalpreet Khun Khun, Aman Mahajan and R.K Bedi, Effect of cationic/anionic organic surfactants on evaporation induced self assembled tin oxide nanostructured films, Applied Surface Science 257 (2011) 29292934